UILU-ENG-76-2030

CIVIL ENGINEERING STUDIES

STRUCTURAL RESEARCH SERIES NO. 432

MEASURED HYSTERESIS RELATIONSHIPS FOR SMALL-SCALE BEAMS

By

D. P. ABRAMS

A Report on a
Research Project
Sponsored by
THE NATIONAL SCIENCE FOUNDATION
Research Grant ENV 7422962

UNIVERSITY OF ILLINOIS
at URBANA-CHAMPAIGN
URBANA, ILLINOIS
NOVEMBER 1976

BIBLIOGRAPHIC DATA SHEET	1. Report No. UILU-ENG-76-2030	2.	3. Recipient's Accession No.
4. Title and Subtitle Measured Hysteresis Relationships for Small Scale Beams			5. Report Date November 1976 6.
7. Author(s) D. P. Abrams			8. Performing Organization Rept. No. SRS No. 432
9. Performing Organization Name and Address University of Illinois at Urbana-Champaign Urbana, Illinois 61801			10. Project/Task/Work Unit No. 11. Contract/Grant No. NSF ENV-7422962
12. Sponsoring Organization Name and Address National Science Foundation Washington, D. C. 20013			13. Type of Report & Period Covered 14.

15. Supplementary Notes

16. Abstracts

Experimental results are presented of cyclic load tests performed on small scale beams. The specimens are replicas of coupling beams used in a ten story coupled wall model structure tested on the University of Illinois Earthquake Simulator. Test variables are the reinforcement and the loading pattern. Descriptions of the fabrication process, test setup, instrumentation and test procedures are presented. Measured moment-rotation relationships and patterns of crack development are used to describe the response and modes of failure of each specimen. The observed response is compared with that obtained from an analytical model representing deformations due to curvature, shear and slip of the reinforcement.

17. Key Words and Document Analysis. 17a. Descriptors

Anchorage, bond, cyclic loads, curvature, hysteresis, moment, reinforcement, rotation, shear deformation, stiffness, strength

17b. Identifiers/Open-Ended Terms

17c. COSATI Field/Group

18. Availability Statement	19. Security Class (This Report)	21. No. of Pages
Release Unlimited	UNCLASSIFIED	
	20. Security Class (This Page) UNCLASSIFIED	22. Price

UILU-ENG-76-2030

MEASURED HYSTERESIS RELATIONSHIPS FOR SMALL-SCALE BEAMS

BY

Daniel P. Abrams

University of Illinois
Urbana, Illinois

November, 1976

ACKNOWLEDGMENT

This investigation is part of a continuing study of reinforced concrete systems subjected to earthquake motions funded by the National Science Foundation under Grant ENV-7422962 and carried out in the Structural Research Laboratory of the Department of Civil Engineering at the University of Illinois, Urbana.

Acknowledgment is due to Mr. D. Aristizabal for his help with the planning of the experimental program. The tests and the studies were supervised by Professor M. A. Sozen.

The writer expresses his appreciation to Professor V. J. MacDonald, Mr. J. Sterner, and Mr. G. Lafenhagen for their advice and assistance with the instrumentation. Gratitude is also due to Mr. O. Ray and his staff for fabrication of the testing apparatus.

TABLE OF CONTENTS

TABLE OF CONTENTS (Continued)

LIST OF TABLES

LIST OF FIGURES

1.0 INTRODUCTION

1.1 Object and Scope

The object of this investigation was to study the hysteresis relationships for small-scale beams. The beam specimens were replicas of coupling beams used in a ten story coupled wall model structure tested by Aristizabal (1976) on the University of Illinois Earthquake Simulator. Moment-rotation relationships for the beams were measured to provide information for a nonlinear analytical study of the ten-story model structures performed by Takayanagi (1976). Six beam specimens were tested with the test variables being the amount of reinforcement and the loading pattern.

1.2 Influence of Coupling Beam on Structural Response

The hysteresis properties of beams used to couple structural walls can have a significant influence on overall building response. The stiffness of the coupling beams can dictate the extent to which each wall will act independently or as a coupled unit. If a reinforced concrete coupled wall structure is proportioned properly, energy from a strong earthquake will be dissipated locally at the beam ends when yielding occurs yet with the walls remaining linear. The permanent deformation of the structure will, therefore, be kept within allowable serviceability limitations. In addition, repair of damaged beams may be expedited with little loss of building function.

2.0 OUTLINE OF EXPERIMENTAL WORK

2.1 Test Variables

A total of six specimens were tested. Variables were the amount of longitudinal beam reinforcement and the loading program.

	Loading Pattern A	Loading Pattern B
Moderately Reinforced Beam	--	SD3, SD4
Heavily Reinforced Beam	SM1, SM4	SM2, SM3

Loading program A consisted of loading each beam to its maximum moment capacity for all cycles to study strength and stiffness variations with increasing damage. The beams of loading program B were loaded to the maximum moment for the first cycle only. Successive loading cycles were applied maintaining the maximum rotations of the first cycle.

2.2 Structural Idealization

The primary function of a beam coupling two structural walls is to ensure some level of beam action in the total structure, to provide a connection between the two walls so that the axial thrust in the walls can vary. For an ideally symmetrical pair of structural walls, the end moments applied to the ends of the beam are equal in magnitude causing tension on opposite extreme fibers for each end of the beam. A schematic description of this structural action is presented in Fig. 2.1. To simulate the end moments occurring in the ten-story prototype structure, replicas of representative beams were tested. A single concentrated load was applied to the pair of piers through pin connections, nine in. above the beam

centerline to develop the beam end moments. A second set of pin connections in the piers served as reactions for the load. Free body diagrams of the piers and beam are shown in Fig. 2.2. The applied load can be related to the average beam end moment by summing moments about each pin reaction. For the left pier

$$P_1 h = \frac{(M_1 + M_2)}{\ell} a + M_1 \qquad (1)$$

Similarly for the right pier

$$P_2 h = \frac{(M_1 + M_2)}{\ell} a + M_2 \qquad (2)$$

If the total applied load is denoted by "P" and the average end moment by "M"

$$P = P_1 + P_2$$

$$M = (M_1 + M_2)/2$$

Then adding equations (1) and (2), substituting for P and M, and solving for M

$$M = \frac{Ph}{2(\frac{2a}{\ell} + 1)}$$

which for the test specimens is numerically equal to

$$M = \frac{P(9.0")}{2(\frac{2(3.5)}{4.0} + 1)} = 1.64P$$

2.3 Specimen Description

A description of the specimens is presented in Fig. 2.3. Each specimen consisted of two 1 by 7 by 17-in. long piers cast monolithically with a 1-in. wide by 1.5-in. thick beam with a span of 4-in. Specimen type "SM" was heavily reinforced with 3.3% reinforcement per face. Specimen type "SD" was moderately reinforced with 1.6% reinforcement per face. Anchorage of the No. 8 gage longitudinal beam reinforcement was provided considering a lower bound on the bond stress of 450 psi. Ample shear reinforcement in the beams was provided so that the full moment capacity of each beam could be developed without a shear failure. Pier reinforcement was matched with that for typical story levels of the ten story model.

2.4 Fabrication

The test specimens were cast horizontally using the same procedures as Aristizabal (1976). A mechanical stud vibrator was placed against the steel plate formwork to consolidate the micro-concrete. The excess concrete was struck off and then troweled to a smooth finish. Steel bars forming the edges of the specimens were removed the next day to avoid shrinkage cracking of the specimen. After one week of curing under wet burlap and plastic sheets, the specimens were removed from the forms and stored in the laboratory. Measured specimen dimensions and ages are presented in Table 2.1.

All specimens were cast simultaneously from the same concrete mix. The mix proportions by dry weight were 1: 0.96 : 3.83 (cement: fine aggregate: coarse aggregate). High early strength (Type III) cement was used with the water-cement ratio being 0.80. The fine aggregate was fine lake sand. Coarse Wabash River sand served as the coarse aggregate. The concrete was mixed in a 400 pound batch in a one ton capacity Koehring Cyclo-Mixer.

Model reinforcement was annealed at 900° F for two hours and allowed to cool in the oven. Longitudinal beam reinforcement was then knurled to replicate the reinforcement in the ten story model test structure. The wire was cleaned with acetone and tied together using No. 19 gage wire. As can be seen in Fig. 2.3, the longitudinal beam reinforcement for type SM specimens was welded to the exterior pier reinforcement to improve embedment characteristics of the wire.

2.5 Material Properties

Ten 4-in. diameter cylinders by 8-in. long and five 2 x 2-in. prisms by 8-in. long were cast to establish material properties of the concrete. The cylinders were tested in a 300-kip Riehle universal testing machine. Six cylinders were tested in compression using a 0.0001-in. mechanical dial gage to measure strain. The measured concrete stress-strain curve is presented in Fig. 2.4. The descending portion of each curve could not be obtained due to limitations of the testing machine. Four cylinders were split by applying compression normal to the cylinder's longitudinal axis to obtain an estimate of the concrete's tensile strength. The prisms were loaded at midspan with a 120 kip capacity Riehle testing machine. Splitting strengths and moduli of rupture for the control samples are given in Table 2.2.

Representative stress-strain relationships for the model reinforcement are given in Fig. 2.5 through 2.8. An extensive study of the tensile properties of the No. 8 gage wire is presented by Staffier (1975). Bond characteristics of the wire was examined with pullout tests by Gavlin (1976).

2.6 Test Setup

A description of the test setup is presented in Fig. 2.9. Each specimen was mounted to the testing apparatus with 1 1/2-in. O.D. ball

bearings which were press fitted to the supporting 3-in. channels. The ball bearings were bolted firmly to each specimen with 5/8-in. diameter bolts as depeicted in Fig. 2.10 so that slippage of the connection would be minimal. Four 1 1/2-in. x 4-in. bars and a 1-in. base plate bolted to a fixed base served to anchor each specimen. The piers of specimen type SM were pre-stressed to a load of approximately 1000 pounds to simulate the axial load in the intermediate level piers of the ten story dynamically tested model. This was done using #18g wire cables wrapped around each pier and tensioned using a screw and bar arrangement.

The load was applied to another set of 3-in. channels which transferred the load to the specimen through similar ball bearing connections so that pier rotation would not be restrained. A 2.5 kip capacity ram operated in load control through a MTS closed loop servo-hydraulic system was used to load the specimens.

2.7 Instrumentation

Aluminum bars were epoxied to the outside edge of each pier to serve as beam end rotation indicators. Three linear voltage differential transformers (LVDT's) were used to measure the rotation of each aluminum bar as well as the vertical and horizontal rigid body translations so that the effect of connection slippages could be included in the measured rotations. A description of the relationship between the displacement readings and the beam end rotations is presented in Appendix A. The LVDT's were regulated using a 6 volt power supply. They were initially calibrated using dial gages. Digitized electrical signals from the LVDT's and the ram were punched on paper tape using a VIDAR data aquisition system and a teletype.

The paper tape was then read into a DEC-10 computer file where the signals were calibrated and punched on computer cards. The cards were read into an IBM-360 computer so that moments and rotations could be calculated, and plotted using Calcomp subroutines.

2.8 Test Procedures

Specific loading patterns for each specimen are presented in Fig. 2.11. The loading was monitored during each test using an X-Y plotter indicating ram load versus ram displacement. The ram load was held constant at load intervals of 100 pounds for a time span not exceeding ten seconds so that data could be taken to define each hysteresis curve.

Hydrocal was placed at the interfaces between components of the anchorage system to detect for slippages. Crack widths and propagations were recorded at ram load increments of approximately 500 pounds. Photographs of the damage in each beam were taken at peak loads for all cycles.

3. EXPERIMENTAL OBSERVATIONS

3.1 Introductory Remarks

Observed response of the test specimens is presented and discussed in this chapter. Measured moment-rotation relationships are used to describe the response of each specimen. Observed patterns of crack development are presented to discuss the behavior qualitatively. General features of observed behavior are reported as well as specific failure modes for each specimen.

3.2 Measured Moment-Rotation Relationships

Measured moment-rotation relationships for each specimen are presented in Fig. 3.1 through 3.6. The end moment, determined as described in Section 2.2, is plotted against the average end rotation for all cycles of loading. The end moment is also plotted against rotations measured at each end for individual cycles.

The hysteretic relationships illustrate general characteristics of the behavior of reinforced concrete members subjected to cyclic loading. Three distinctive trends were observed: (1) a variation in stiffness within each cycle of loading, including a severe reduction in stiffness in the low-moment regions; (2) a reduction in stiffness between successive cycles of loading for similar ranges of moment; and (3) a reduction in strength between successive cycles of loading for those specimens loaded to the apparent moment capacity in each cycle.

Representative ranges of observed response are depicted in Fig. 3.7. The first quarter cycle consisted of three nearly linear portions: AB,

BC and CD. Portion AB, representing the behavior of an uncracked beam remained linear to a moment of approximately 0.3 kip-in. Observed increase in rotation was essentially proportional to increase in moment from points B to C, with the increase in rotation exceeding that in moment as the yield moment was approached. At point C (approximately a moment of 1.7 kip-in. for type SD and 2.9 kip-in. for type SM) the stiffness reduced greatly indicating yield of the tensile reinforcement. The loading was stopped (at point D) when the slope of the moment-rotation curve was virtually zero.

The unloading portion DEF could be represented ideally by two linear segments, DE and EF. Segment DE was typically almost vertical. Segment EF had a steeper slope than that of segment BC.

In all cases, the transition segment FG was S-shaped. It was not symmetrical about the horizontal axis, the gradual change in slope in the unloading curve being initiated at a low positive load level on the order of 0.2 kip-in.

Loading to point H resulted in a similar type of behavior as observed for portion BC. The reversed loading stiffness (portion GH) was less than the loading stiffness (portion BC) for all specimens. Loading to the apparent maximum moment capacity at point I was accompanied by a gradual reduction in the slope of the moment-rotation curve. Maximum strengths observed for all specimens were less for the second half cycle than for the first.

Unloading from point I followed in a similar fashion as from point D. Initial unloading to point J resulted in a small change of rotation. Unloading to point K resulted in a greater slope for segment JK than for the reversed loading segment GH, but less than the first half cycle unloading segment EF.

The transition segment KL was S-shaped like segment FG but extended over a wider range of rotation. Point K was observed at approximately the same load level as point L.

Subsequent cycles of loading consistently resulted in similar types of behavior as observed for the initial cycle.

(1) Loading stiffnesses decreased progressively with each half cycle.

(2) Specimen strength deteriorated with each half cycle.

(3) Initial unloading for each half cycle resulted in a small change of observed rotation.

(4) The unloading stiffness for each half cycle was always greater than the loading stiffness.

(5) Unloading stiffnesses decreased progressively for each half cycle.

(6) The stiffness transition in the low-moment regions occurred progressively over a wider range of observed rotation for successive cycles.

3.3 Modes of Failure

The failure mechanism observed for the specimens consisted of spalling of the shell concrete, crushing of the extreme compressive fiber concrete, and slip of the main reinforcement.

All specimens, except SM3, developed the yield stress of the reinforcement in the first quarter cycle of loading without failure in shear, anchorage or by crushing of the concrete. Specimen SM3 did experience a sudden compressive failure of the extreme fiber concrete at the maximum

moment of the first quarter cycle. This resulted in a rapid loss of strength for which data could not be taken. The reason for only one specimen out of four heavily reinforced specimens failing in compression is attributed to scatter in the compressive properties of the concrete.

The yield stress of the reinforcement for subsequent half cycles was not developed. This is evidenced by the size of the observed maximum moment which is less than that required to produce yielding. The large increase in observed rotation for the small increase in applied moment indicates that the main reinforcement was slipping relative to the concrete before the yield stress could be developed. The maximum moment attained for successive cycles further decreased, indicating a deterioration of available bond strength with cyclic loading.

A diagonal tension failure was observed at the maximum rotation for the second half cycle for specimen SD3. A diagonal crack suddenly developed from the upper left to the lower right corners of the beam. Loading in the reverse direction (first half of second cycle) resulted in another diagonal crack from opposite corners which spalled a large portion of the shell concrete between the diagonal x-cracks. Because of the large reduction in specimen strength and stiffness, the test was completed at the end of the second cycle.

3.4 Observed Patterns of Crack Development

The primary pattern of observed crack development included flexural cracks at oppostie corners of each beam, diagonal shear cracks, and splitting cracks parallel to the longitudinal reinforcement. The general pattern of crack development is shown in Fig. 3.8. The first observed

cracks were short, vertical cracks at the end regions of each beam which were noticed at an applied moment of approximately 0.40 kip-in. As the load was increased, these cracks opened and propagated linearly. Diagonal cracks were first observed at a moment of approximately 2.5 kip-in. for type SM and 1.3 kip-in. for type SD. The diagonal cracks ranged in width from 0.002 to 0.004 in. As the load reached the maximum, faint splitting cracks were observed with minor crushing of the concrete at the compressive portions of the end regions.

The diagonal cracks closed during unloading, but the flexural cracks did not. Reversing the load resulted in closing of the flexural cracks at a moment of approximately 0.800 kip-in. for type SM and 0.500 kip-in. for type SD. Further loading in the reverse direction resulted in a similar network of cracks of the opposite sense.

Representative photographs of damage at peak loads of successive cycles are presented in Fig. 3.9. Flexural cracks at the beam ends became wider for successive cycles. Diagonal cracks also became wider and resulted in some spalling of the side cover for type SD specimens. Crushing of the concrete at the beam ends became more prevalent. Splitting cracks propagated further along the reinforcement resulting in spalling of the top and bottom concrete cover.

The width of the cracks occurring at the beam ends was measured during the first two cycles of loading and is presented in Table 3.1. Because of the inaccuracies of the crack width measurement, crack widths are presented only to support qualitatively the measured moment-rotation relationships. The influence of the crack width on the shape of the measured hysteresis relationships can be seen by translating the observed crack

widths to equivalent end rotations, and plotting versus moment. This relationship for the first loading cycle is shown in Fig. 3.10 for type SD specimens and in Fig. 3.11 for type SM specimens. A constant depth to the neutral axis based on the cracked section has been assumed to relate crack width to rotation.

Rotation calculated directly from crack widths were a significant portion of the total rotation. The average observed crack width was 0.007 in. at the maximum rotation of the first half cycle, indicating that the hinge rotation was due to more than strain in the reinforcement. Crack widths at maximum rotations of other cycles confirmed this observation.

The shape of each curve resembled the measured moment-rotation curve. The rotation calculated from observed crack widths followed a linear trend with applied moment for the major loading and unloading portions of each curve. As the load was reversed the effect of the cracks closing on the beam end rotation was quite significant. The large reduction in flexural stiffness observed from the measured moment-rotation curve is evidenced by the large change in crack width for a small change of reversed moment.

4. ANALYTICAL STUDIES

4.1 Introductory Remarks

A mathematical model to analyze the specimen response is presented in this chapter. Beam end rotation is assumed to consist of three components generated by deformation due to curvature of the beam, deformation due to shear, and slip of the reinforcement.

4.2 Moment-Curvature Study

Two moment-curvature studies were performed. A moment-curvature relationship for monotonically increasing load was developed to investigate limiting curvatures based on the ultimate strain of the concrete. A moment-curvature relationship for cyclic loading was developed to investigate the effect of loading reversals on section behavior.

Both relationships were developed considering (1) a linear strain distribution across the section, (2) an idealized stress-strain relationship for the reinforcement and concrete, and (3) nominal section dimensions as presented in Fig. 2.3.

An iterative procedure was used to calculate points on the moment-curvature curve corresponding to strains of the extreme compressive fiber. Strains and associated stresses were determined from an assumed curvature. Forces were calculated from the stresses. Equilibrium of the forces was used as the criterion for the validity of the assumed curvature. The procedure was reiterated varying the value of assumed curvature until force equilibrium was met. The internal resisting moment of the section was then

calculated by summing the products of the forces and respective distances from mid-depth of the section.

(a) Moment-Curvature Relationship for Monotonically Increasing Load

The assumed stress-strain relationship for the concrete is presented in Fig. 4.1. Tensile strength of the concrete was neglected. A parabola was assumed for the shape of the curve up to the maximum stress. A straight line was assumed for the descending portion to the maximum strain.

The assumed stress-strain relationship of the reinforcement is presented in Fig. 4.2. An idealized bilinear curve has been used to represent the observed behavior of the reinforcement from tension tests (Staffier, 1975).

Calculated moment-curvature relationships for a monotonically increasing load are presented in Fig. 4.3 and 4.4 for type SD and SM specimens respectively.

(b) Moment-Curvature Relationship for Cyclic Loading

A computer program developed by Karlsson was used to obtain moment-curvature relationships for the first one and a quarter cycles of loading. A description of Karlsson's model is provided by Wight (1973). Type SD and type SM sections were modeled with twelve strips of equal width as shown in Fig. 4.5. Unconfined concrete outside of the stirrups was assumed to spall at a strain of 0.004. Confined concrete within the stirrups was assumed to maintain the maximum compressive strength at large compressive strains.

The stress-strain relationship for the reinforcement was assumed to be bilinear for the first quarter cycle of loading. A Ramberg-Osgood function was used to idealize the behavior for subsequent loading.

The calculated moment-curvature relationship for cyclic loading is presented in Fig. 4.6 for type SD and in Fig. 4.7 for type SM.

4.3 Reinforcement Stress-Slip Relationship

To study the influence of slip of the main reinforcement on beam end rotation, a simple finite element model of the bar embedment was developed. A description of the model is presented in Fig. 4.8. The idealized anchored bar was divided into four elements of equal length. Bond resistance was modeled using translational springs of equivalent stiffness. Incremental nodal displacements, reinforcement stresses, and bond stresses were calculated for an incremental load applied to the end of the bar. The load was increased until a particular reinforcing element or spring stress exceeded a limiting stress. The stiffness was then recalculated using a revised modulus for that element.

The bar was unloaded when the yield stress at the face of the anchorage was attained, or when the bond resistance of all springs was zero.

The assumed bond stress-slip relationship is presented in Fig. 4.9. The equivalent stiffness of a spring was calculated by considering a uniform bond stress along the tributary length of embedded bar associated with the spring. The stiffness was computed as the product of the slope of the bond stress-slip curve, the perimeter of the bar and the tributary length. The bond stress-slip relationship was inferred from pullout tests (Gavlin) for a monotonically increasing load.

The assumed reinforcement stress-strain relationship is presented in Fig. 4.9. The first quarter cycle of loading is based on experimental data obtained by Staffier (1975). Subsequent half cycles of loading were

assumed to behave in the same manner. The axial stiffness of each reinforcing element was calculated by multiplying the area of the bar times the modulus of elasticity and dividing by the element length.

The incremental stiffness matrix was generated using the conventional approach of imposing a unit displacement at each node while fixing all others, determining the associated nodal forces, and writing the equilibrium equations.

$$\begin{bmatrix} KS1+KB1 & -KS1 & & & \\ -KS1 & KS1+KS2+KB2 & -KS2 & & \\ & -KS2 & KS2+KS3+KB3 & -KS3 & \\ & & -KS3 & KS3+KS4+KB4 & -KS4 \\ & & & -KS4 & KS4+KB5 \end{bmatrix} \times \begin{bmatrix} u_1 \\ u_2 \\ u_3 \\ u_4 \\ u_5 \end{bmatrix} = \begin{bmatrix} P \\ 0 \\ 0 \\ 0 \\ 0 \end{bmatrix}$$

Since the load was applied only to the node at the end of the bar, the stiffness matrix was partitioned and condensed to give the load-slip stiffness. The equations were solved to give an incremental slip at the face of the anchorage. Nodal displacements were calculated from this slip so that reinforcing element and bond spring stresses could be determined.

Reinforcing element stresses were calculated from the strains which were determined from the difference in adjacent nodal displacements. Bond spring stresses were determined from the nodal displacements and the spring stiffnesses.

The calculated reinforcing stress-slip relationship at the loaded end of the bar for the first one and a quarter cycles of loading is presented in Fig. 4.10.

4.4 Shear Deformations

The small span to depth ratio of the specimens produced high shear stresses at ultimate loads. Because of the uncertainty involved with the calculation of shear deformation after cracking and with cyclic loading, shear deformations were approximated using the principles of elasticity for a homogeneous plain concrete beam. The effect of cracking was considered by reducing the uncracked shear stiffness by an arbitrary factor of two.

The cracked shear stiffness was calculated using the relationship

$$K_v = \frac{V}{A_s} = 0.5 \left(\frac{AG}{\alpha L}\right)$$

where V = beam shear

A_s = shear deformation

G = shear modulus = $0.4\ E_c$

E_c = modulus of elasticity of concrete = 3000 ksi

A = area of section = 1.5 sq. in.

L = length of beam = 4.0 in.

α = shape factor for rectangular section = 1.2

The approximated beam shear stiffness for both type SD and SM specimens was 190 kip/in.

4.5 Moment-Rotation Relationship

For an incremental end moment, an incremental end rotation was calculated considering linear segments of the moment-curvature, reinforcing stress-slip, and shear deformation relationships as described earlier in this chapter. The end moment was increased until a particular linear range of any one of the above relationships was exceeded. A new linear range was defined, and the end moment was increased further. The end moment was descreased when the limiting rotation which was observed for the test specimens was attained.

End rotation due to curvature of the beam was calculated using the principle of moment-area as depicted in Fig. 4.11. The half span of the beam was divided into five elements of equal width. For an incremental end moment, the average moment across each element was calculated. An incremental curvature was assigned to each element by reading the calculated moment-curvature curve. The area under the curvature distribution was computed for each element, and multiplied by the distance from the element centroid to the midspan of the beam. The summation of these products was equal to the deflection at the end of a cantilever beam with a span equal to half the span of the specimen. Incremental rotations at the pin supports were determined from these deflections as described in Fig. 4.11.

The reinforcement stress-slip relationship was translated to an equivalent end moment-rotation relationship as described in Fig. 4.12. Moment was related to reinforcing stress by considering a constant lever arm. Hinge rotation at the end of the beam due to slip of the reinforcement was calculated as the ratio of the slip of the tensile reinforcement and the distance from the tensile reinforcement to the neutral axis. The location of the

neutral axis and the length of the lever arm were based on the transformed section for a fully cracked section. Both were assumed to be invariant with the moment applied to the section, which is reasonably valid before yield of the reinforcement occurs. After yield occurs, the additional slip is small since the additional tension on the reinforcement is small. Measured rotation at the pin supports was related to the hinge rotation as described in Fig. 4.12.

Shear deformation was related to end rotation in the same manner as described for deflection due to flexure (Fig. 4.11). End moment was related to shear force by simple equilibrium of forces as depicted in Fig. 2.2. Because of the uncertainty involved with the calculation of shear deformation, and the relative insignificance of shear deformation on total end rotation a linear relationship for all cycles was assumed between end moment and rotation due to shear deformation.

5. CALCULATED VS. OBSERVED RESPONSE

5.1 Introductory Remarks

The calculated specimen response using the mathematical model presented in the preceding chapter is compared with the observed response for the first cycle of loading. Variations between the observed and calculated responses are discussed considering limitations of the analytical model in representing the bond strength deterioration within the beam span.

The calculated moment-rotation response for the first cycle is presented with the observed response in Fig. 5.1 for type SD specimens and in Fig. 5.2 for type SM specimens.

5.2 First Half Cycle

For the first half cycle the calculated response agreed reasonably well with the observed response. The calculated stiffness for the first quarter cycle was consistently less than the observed stiffness. The maximum moment calculated for type SM specimens was in all cases smaller than the observed moment. The maximum moment calculated for both type SD specimens was greater than the observed moment. The calculated unloading portions of the curve agreed with the observed response for all specimens except SM3 which had a compression failure.

To show the relative importance of each component of calculated rotation, the contributions of curvature, reinforcement slip and shear deformation are plotted with the observed moment-rotation curves for the first quarter cycle in Fig. 5.3. Slip of the anchored longitudinal beam

reinforcement dominated the shape of the curve. Calculated rotation including slip of the reinforcement was nearly three times the rotation calculated from bending and shear strains. Calculated shear deformation was significant when compared with calculated bending deformation resulting from curvature because of the small span to depth ratio. Shear deformation was found to be far less significant on total rotation because of the strong influence of reinforcement slip on rotation.

Because of the high percentages of reinforcement, the effect of initial cracking of the extreme tension fiber was not critical for studying the nonlinear response. The calculated moment for a plain uncracked concrete section considering a modulus of rupture of 700 psi is 0.3 kip-in.

The gradual reduction in slope of the observed moment-rotation curve from cracking of the extreme tension fiber to the apparent yielding of the tensile reinforcement was also evident in the calculated curve. The reduction in slope of the calculated curve was primarily due to the change of bond stress distribution along the embedded bar. As the tension on the bar was increased, more of the embedded length was required for anchorage. This resulted in a longer length of strained bar and an increased rate of deformation with load.

The calculated stiffness in this range of loading was greater than the observed which may have been because of an inaccurate representation of the reinforcing stress-bar slip relationship assumed for each bond element of the analytical bar-embedment model. The assumed reinforcing stress-slip relationship was based on pullout tests (Gavlin) which has a large scatter of data.

The observed increase in rotation with little increase in moment as the specimen was loaded to the maximum load may not have been due to yielding of the tensile reinforcement. Pullout of the bar may have occurred at a load close to the yield load. The average bond stress along the length of the anchored bar required to develop the yield stress would have been 450 psi which was greater than that observed from pullout tests (Gavlin). This however seems unlikely because of the anchorage detail provided at the end of the beam reinforcement (Fig. 2.3) which was not provided in the pullout tests and should have prevented the bar from pulling out. Additionally, no direct evidence of an anchorage failure was observed when the specimen was dissected following the test.

The failure of the concrete in compression for specimen SM3 was not indicated by the analytical model. A compression failure of the beam should not have occurred regardless of the maximum concrete strain if the longitudinal reinforcement remained bonded along the entire length of bar. However, if the bond strength was insufficient to develop the change of force in the bar along the beam span, then the assumed compressive force on the bar at the beam end would have been reduced, or the bar may have possibly even been in tension. Equality of strains in the concrete at the level of the "compressive" reinforcement and the compressive reinforcement may not have been a valid assumption to make with the analytical model. The compressive force on the concrete would then be increased with a compressive failure of the concrete being a definite possibility for the heavily reinforced type SM specimens. Photographs of the type SM specimens taken at the maximum load of the first quarter cycle indicate that specimen SM3 had the largest cracks parallel with the compressive

reinforcement from the beam ends indicating a bond distress within the span. The fact that one out of four specimens failed in compression was credible because of the dependence of the mode of failure on the compressive strength of the concrete as well as the bond strength.

The deterioration of the bonded length of longitudinal reinforcement along the beam span may also have reduced the internal resisting moment of the beam section. As the effectiveness of the compressive reinforcement was reduced, the depth of the concrete compressive zone was increased, reducing the internal lever arm of the section. The relationship between the internal moment at yield of the tensile reinforcement and the average bond stress along the span (Fig. 5.4) has been derived by considering the stress distribution across the section as presented in Fig. 5.5. The longitudinal reinforcement in the compressive zone was considered to be unbonded with the concrete at the end of the beam. The force in the reinforcement was related to the force at the opposite end of the beam and the average bond stress along the beam span.

As can be seen in Fig. 5.4, the moment for type SM specimens was much more sensitive to a change in bond stress. The loss of compressive force resulting from bond distress was twice as much for the type SM specimens because of the number of wires per face. For the same reason, type SM specimens would have required a higher bond stress within the span to develop the calculated maximum moment based on a fully bonded beam. The heavily reinforced specimens would have required an average bond stress along the span of 1000 psi and the lightly reinforced specimens a stress of 500 psi. This may have been the reason the observed maximum moment for the first quarter cycle was consistently less for the type SM specimens than the calculated.

The bond stress required by this formulation for the type SM specimens to reach the observed yield moment was 780 psi which was greater than observed from the pullout tests. The pullout tests did not include a large shear force across the wire as was the case with the wires of the beam. Frictional forces parallel with the reinforcement from the beam shear ray have increased the apparent bond strength.

5.3 Second Half Cycle

The observed response diverged from the calculated curve for the second half cycle. The larger increase in observed rotation than calculated rotation when the load was reversed indicates that a loss of bond may have occurred when the specimen was loaded to the maximum moment of the first half cycle. Reversing the load would then result in a softer response than considered with the analytical model. As the tensile cracks of the first half cycle were closing, the slope of the moment-rotation curve should have been equal to or greater than that corresponding to a section consisting of the longitudinal reinforcement alone if the wire was bonded with the concrete. A simple calculation of the slope of the moment-rotation curve for a member consisting of only the reinforcement is presented in Fig. 5.6. This indicates that the reinforcement alone ought to be substantially stiffer than what was observed in this range of loading. If the reinforcement was unbonded at the beam ends, the full resistance of the reinforcement as previously calculated would not be observed as the cracks closed. This is further corraborated by the rapid change of observed crack width in this range of loading as mentioned in Section 3.4.

The comparison of observed with calculated response for the remainder of the hysteresis loop becomes confused because of the lack of conformance in the load reversal region. However, the difference between the calculated and observed strength for the second half cycle is quite evident. Further bond deterioration within the beam span (not considered with the analytical model) would reduce the maximum resisting moment in the same manner as described for the first half cycle (Fig. 5.3). Splitting cracks observed along the longitudinal reinforcement were a definite sign of bond deterioration within the span. Comparing the observed length of the splitting cracks from photographs with the calculated lengths of deterioration for the observed yield moments from Fig. 5.4 provides a suitable correlation for both type SD and SM specimens. The same comparison may also be made with good agreement in successive cycles for those specimens loaded to the maximum moment.

6. CONCLUSION

6.1 Scope

Six coupling beam specimens were subjected to a cyclic load to study moment-rotation relationships, and to provide information for the investigation of the behavior of a ten story coupled wall model structure subjected to simulated earthquake motions.

6.2 Conclusion

Slip of the main reinforcement was the major influence on the deformational characteristics of the specimens. Rotations including slip of the tensile reinforcement were approximately three times those rotations without considering slip. Shear deformations were not significant to beam end rotation even with the high shear stresses because of the large rotations due to slip of the reinforcement.

Specimens loaded to the same rotation limit as for previous cycles exhibited little deterioration of stiffness. Specimens loaded to the maximum moment for each half cycle exhibited a progressive deterioration of both stiffness and strength which was attributed to successive deterioration of the bonded length of the longitudinal reinforcement within the beam span.

Heavily reinforced specimens (type SM) performed more reliably in successive cycles than the lightly reinforced specimens because of the greater confinement offered by the stirrups. A severe reduction in strength and stiffness was observed for one of the lightly reinforced specimens once the side cover had spalled.

6.3 Further Research

This limited experimental study emphasized the need for further research in two areas related to the nonlinear response of reinforced concrete structures subjected to cyclic loads.

(1) The dominance of slip of the reinforcement and deterioration of the bond strength on the shape of the hysteresis loop in beams with high moment gradients provides cause for further investigation of the bond characteristics of reinforcement subjected to cyclic loading.

(2) The observed hysteretic response was influenced by phenomena not recognized by algorithms based on sectional characteristics and modified by elementary models of bond slip. A set of rules for hysteresis, such as the ones in reference 5, are not totally relevant to the hysteresis of beams with high moment gradients. Research is needed to develop either more comprehensive and correct or simpler and economical models for hysteresis.

LIST OF REFERENCES

1. Aristizabal-Ochoa, J. D. and M. A. Sozen, "Behavior of Ten-Story Reinforced Concrete Walls Subjected to Earthquake Motions," Civil Engineering Studies, Structural Research Series No. 431, University of Illinois, Urbana, October 1976.

2. Gavlin, N. L., "Bond Characteristics of Model Reinforcement," Civil Engineering Studies, Structural Research Series No. 427, University of Illinois, Urbana, April 1976.

3. Staffier, S. R. and M. A. Sozen, "Effect of Strain Rate on Yield Stress of Model Reinforcement," Civil Engineering Studies Structural Research Series No. 415, University of Illinois, Urbana, February 1975.

4. Takayanagi, T., and W. C. Schnobrich, "Computed Behavior of Reinforced Concrete Coupled Shear Walls," Civil Engineering Studies, Structural Research Series No. 434, University of Illinois, Urbana, December 1976.

5. Takeda, T., Sozen M. A., and Nielsen, N. M., "Reinforced Concrete Response to Simulated Earthquakes," Journal of the Structural Division, ASCE, Vol. 96, No. ST12, December 1970, pp. 2557-2573.

6. Wright, J. K. and M. A. Sozen "Shear Strength Decay in Reinforced Concrete Columns Subjected to Large Deflection Reversals," Civil Engineering Studies, Structural Research Series No. 403, University of Illinois, Urbana, August 1973.

Table 2.1

Ages and Measured Specimen Dimensions

Specimen	Age (Days)	Beam Dimensions (Inches) Width	Depth	Span
SD3	113	1.02	1.50	4.00
SD4	126	0.99	1.50	4.00
SM1	134	1.01	1.51	4.02
SM2	136	1.04	1.51	3.98
SM3	137	1.02	1.49	4.02
SM4	137	1.03	1.48	4.02

Table 2.2

Measured Splitting Strength and Modulus of Rupture

Cylinder/Prism	Splitting Strength (psi)	Modulus of Rupture (psi)
1	310	855
2	362	990
3	354	810
4	406	922
5	--	979

Table 3.1

Measured Crack Widths

(Inches)

End Moment (kip-in.)	Specimen SD3				Specimen SD4			
	A*	B	C	D	A	B	C	D
Cycle No. 1								
0.3	0.003	0.000	0.000	0.003	0.003	0.000	0.000	0.003
0.6	0.004	0.000	0.000	0.004	0.004	0.000	0.000	0.004
1.0	0.005	0.000	0.000	0.005	0.005	0.000	0.000	0.005
1.3	0.006	0.000	0.000	0.006	0.007	0.000	0.000	0.006
(+) Max.	0.007	0.000	0.000	0.007	0.009	0.000	0.000	0.007
1.1	0.005	0.000	0.000	0.004	0.008	0.000	0.000	0.006
0.5	0.004	0.000	0.000	0.003	0.006	0.000	0.000	0.004
0.00	0.003	0.000	0.000	0.003	0.003	0.000	0.000	0.003
-0.3	0.000	0.003	0.003	0.000	0.002	0.003	0.003	0.002
-0.6	0.000	0.003	0.005	0.000	0.000	0.004	0.005	0.000
-1.0	0.000	0.007	0.006	0.000	0.000	0.007	0.006	0.000
(-) Max.	0.000	0.011	0.008	0.000	0.000	0.011	0.007	0.000
-0.8	0.000	0.010	0.007	0.000	0.000	0.011	0.007	0.000
0.0	0.000	0.006	0.004	0.000	0.000	0.007	0.004	0.000

*For notation see Fig. 3.8

Table 3.1 (Continued)

Measured Crack Widths

(Inches)

End Moment (kip-in.)	Specimen SM1				Specimen SM2			
Cycle No. 1	A*	B	C	D	A	B	C	D
0.6	0.002	0.000	0.000	0.002	0.001	0.000	0.000	0.002
1.3	0.003	0.000	0.000	0.004	0.002	0.000	0.000	0.003
2.0	0.005	0.000	0.000	0.005	0.003	0.000	0.000	0.003
2.6	0.005	0.000	0.000	0.005	0.004	0.000	0.000	0.005
(+) Max.	0.005	0.000	0.000	0.006	0.005	0.000	0.000	0.006
1.5	0.004	0.000	0.000	0.005	0.004	0.000	0.000	0.004
0.5	0.003	0.000	0.000	0.004	0.003	0.000	0.000	0.003
0.0	0.002	0.000	0.000	0.002	0.002	0.000	0.000	0.002
-0.6	0.000	0.002	0.002	0.000	0.000	0.003	0.003	0.000
-1.3	0.000	0.003	0.003	0.000	0.000	0.003	0.003	0.000
-2.0	0.000	0.003	0.003	0.000	0.000	0.004	0.004	0.000
(-) Max.	0.000	0.006	0.004	0.000	0.000	0.005	0.005	0.000
-0.6	0.000	0.003	0.004	0.000	0.000	0.004	0.004	0.000
0.0	0.000	0.002	0.003	0.000	0.000	0.003	0.003	0.000

*For notation see Fig. 3.8

Table 3.1 (Continued)

Measured Crack Widths

(Inches)

End Moment (kip-in.)	Specimen SM3				Specimen SM4			
	A*	B	C	D	A	B	C	D
Cycle No. 1								
0.6	0.002	0.000	0.000	0.002	0.002	0.000	0.000	0.002
1.3	0.003	0.000	0.000	0.003	0.002	0.000	0.000	0.003
2.0	0.003	0.000	0.000	0.003	0.003	0.000	0.000	0.003
2.6	0.004	0.000	0.000	0.004	0.004	0.000	0.000	0.004
(+) Max.	0.004	0.000	0.000	0.004	0.005	0.000	0.000	0.004
1.5	0.004	0.000	0.000	0.004	0.004	0.000	0.000	0.003
0.5	0.003	0.000	0.000	0.003	0.003	0.000	0.000	0.003
0.0	0.003	0.000	0.000	0.003	0.002	0.000	0.000	0.002
-0.6	0.000	0.005	0.006	0.000	0.000	0.002	0.002	0.000
-1.3	0.000	0.005	0.007	0.000	0.000	0.004	0.003	0.000
-2.0	0.000	0.006	0.007	0.000	0.000	0.006	0.005	0.000
(-) Max.	0.000	0.007	0.008	0.000	0.000	0.007	0.007	0.000
-0.6	0.000	0.005	0.006	0.000	0.000	0.005	0.005	0.000
0.0	0.000	0.004	0.005	0.000	0.000	0.004	0.004	0.000

*For notation see Fig. 3.8

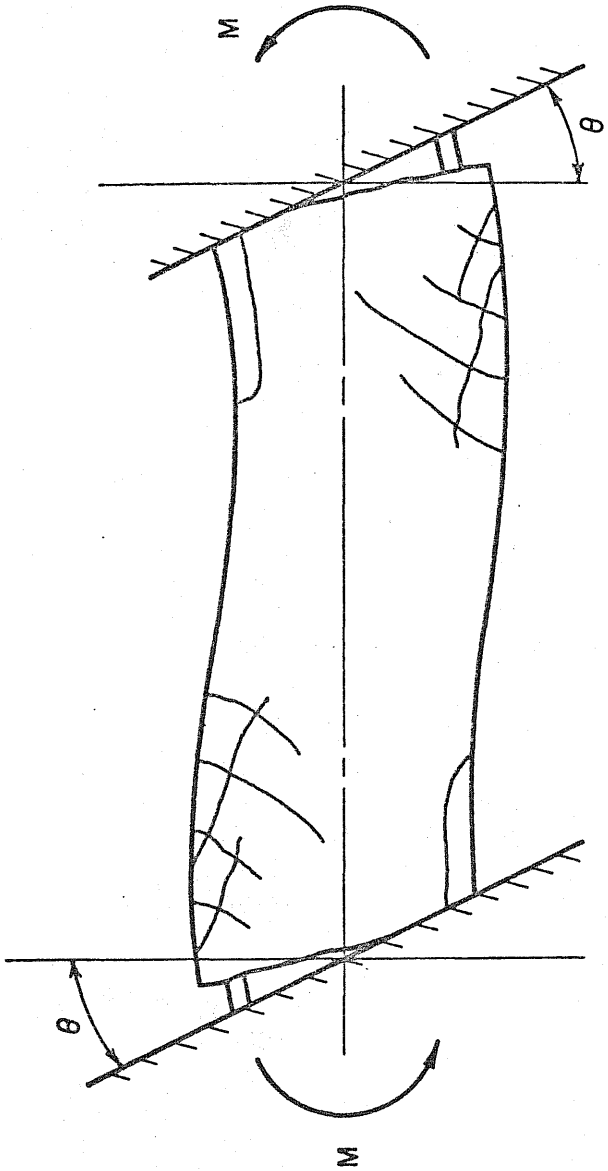

Fig. 2.1 Structural Idealization of Specimens

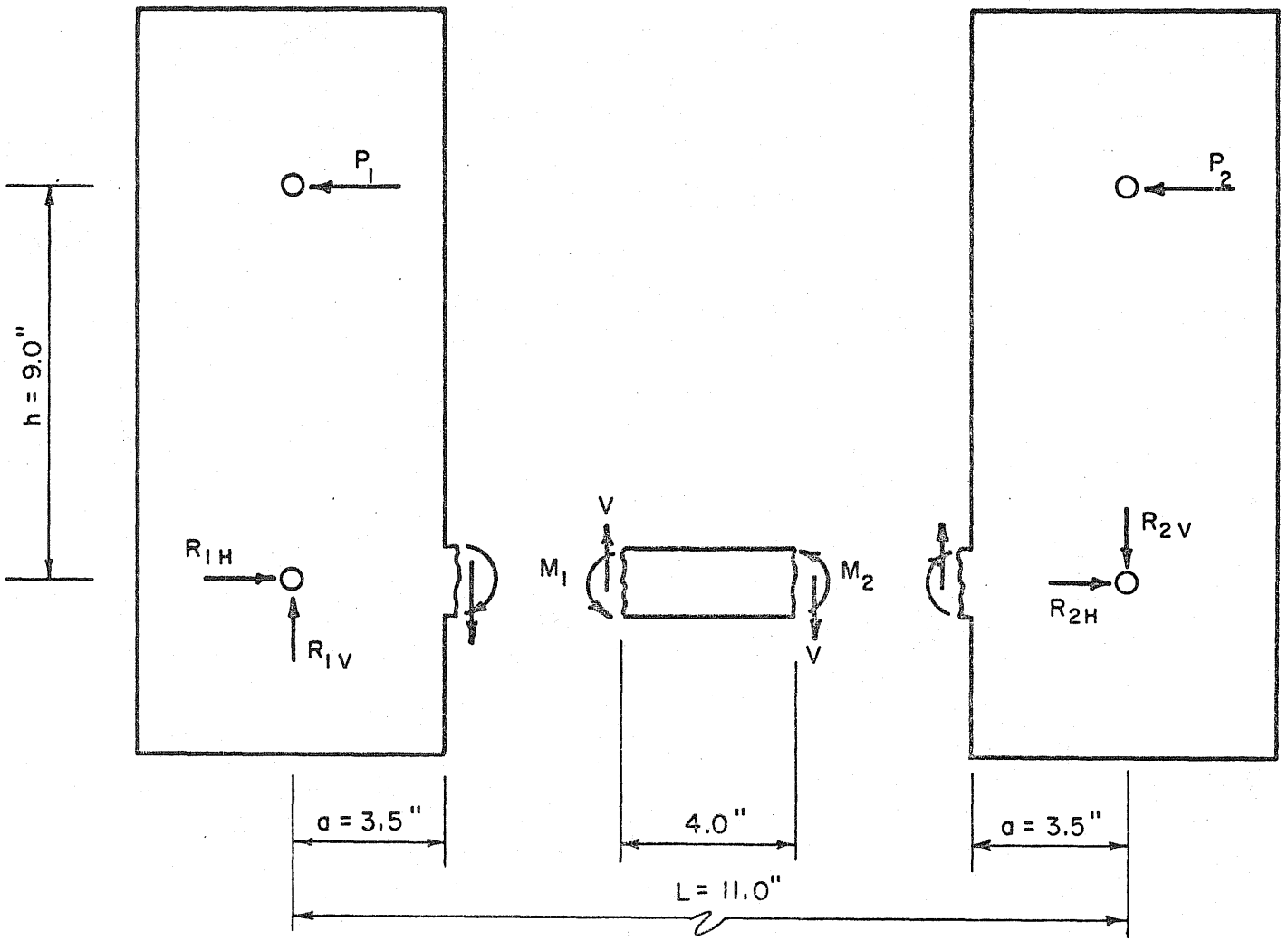

Fig. 2.2 Free Body Diagrams of Piers and Beam

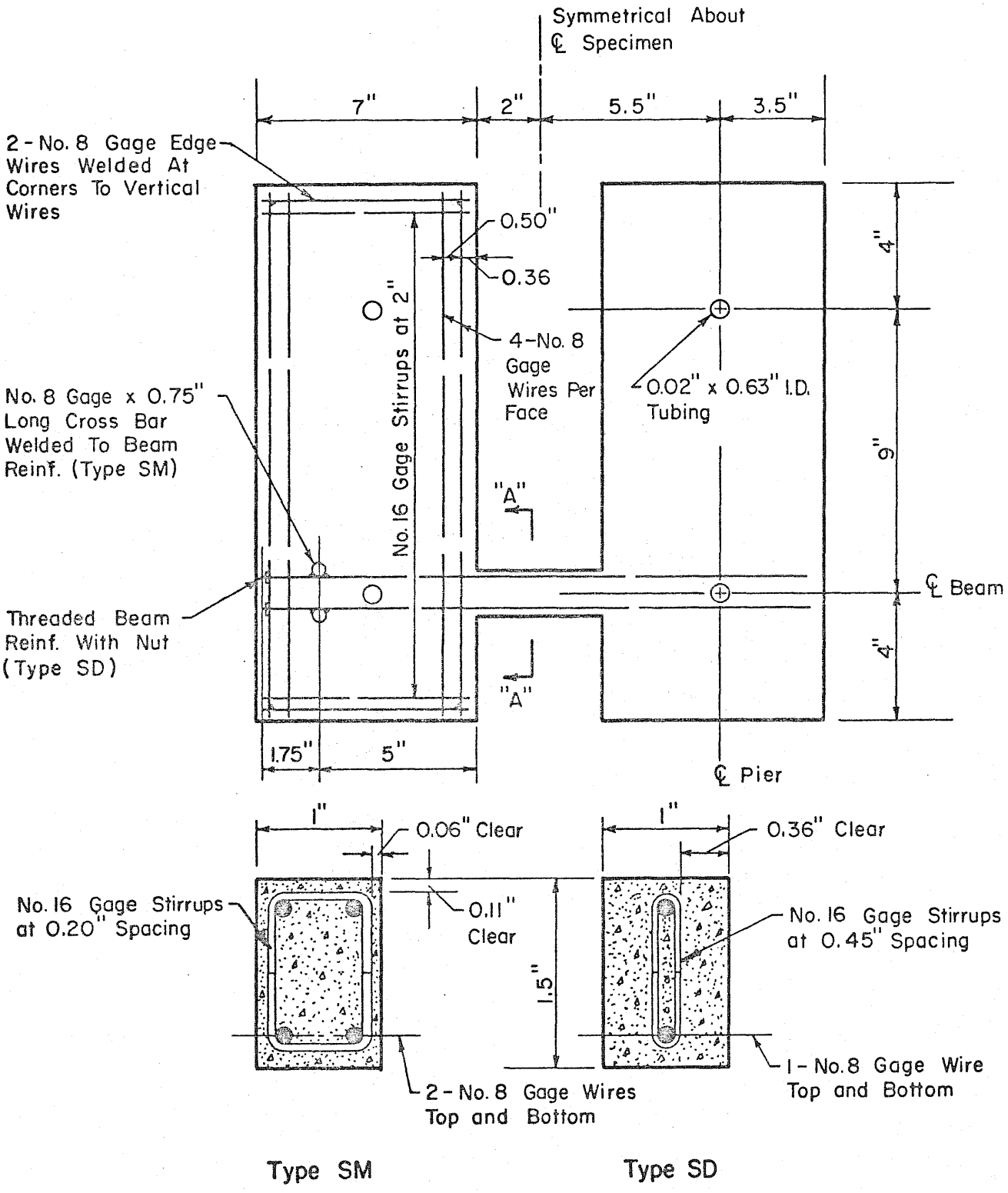

Fig. 2.3 Specimen Description

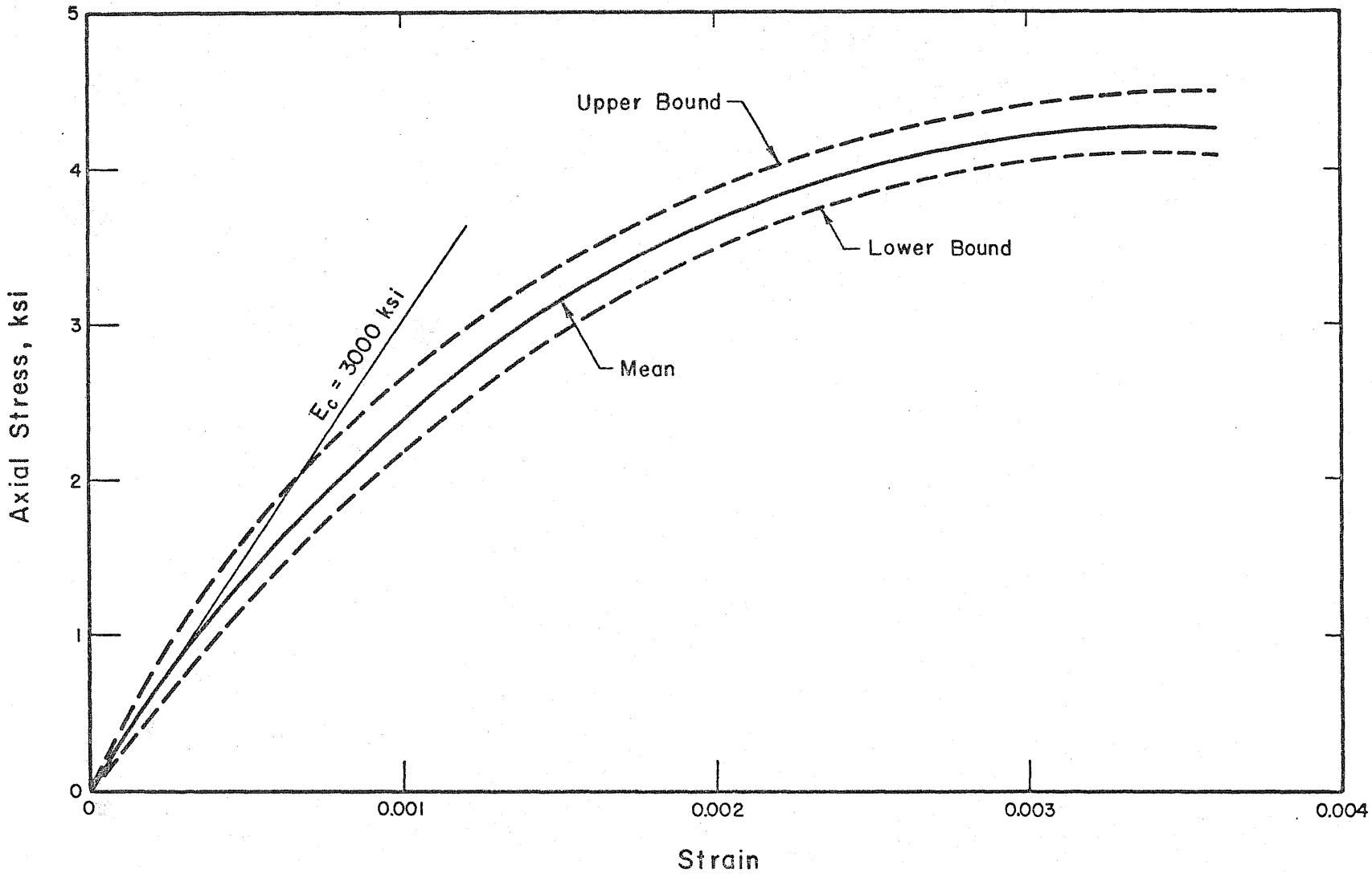

Fig. 2.4 Measured Concrete Stress-Strain Relationship

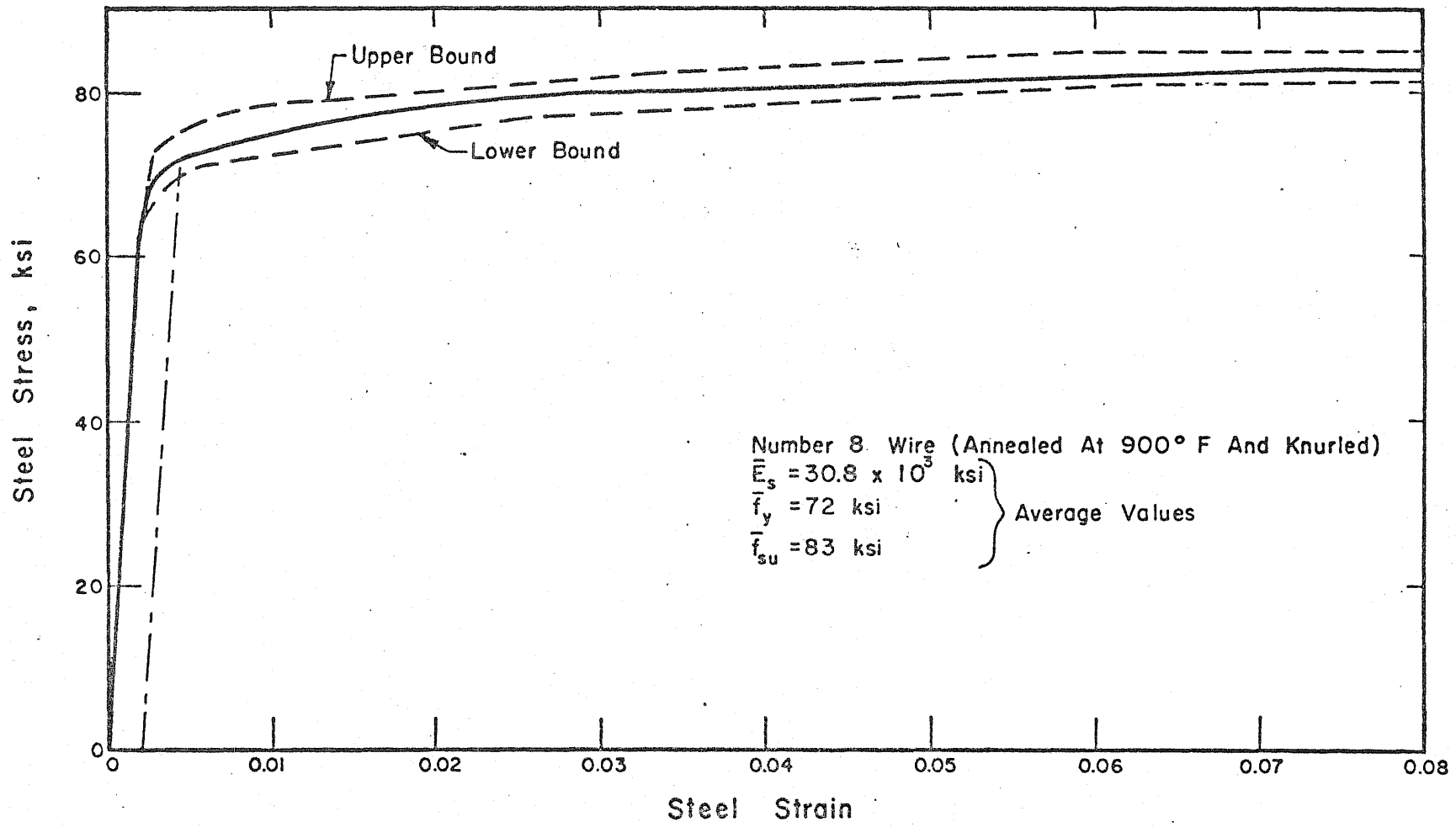

Fig. 2.5 Measured Stress-Strain Relationship for No. 8 Gage Wire

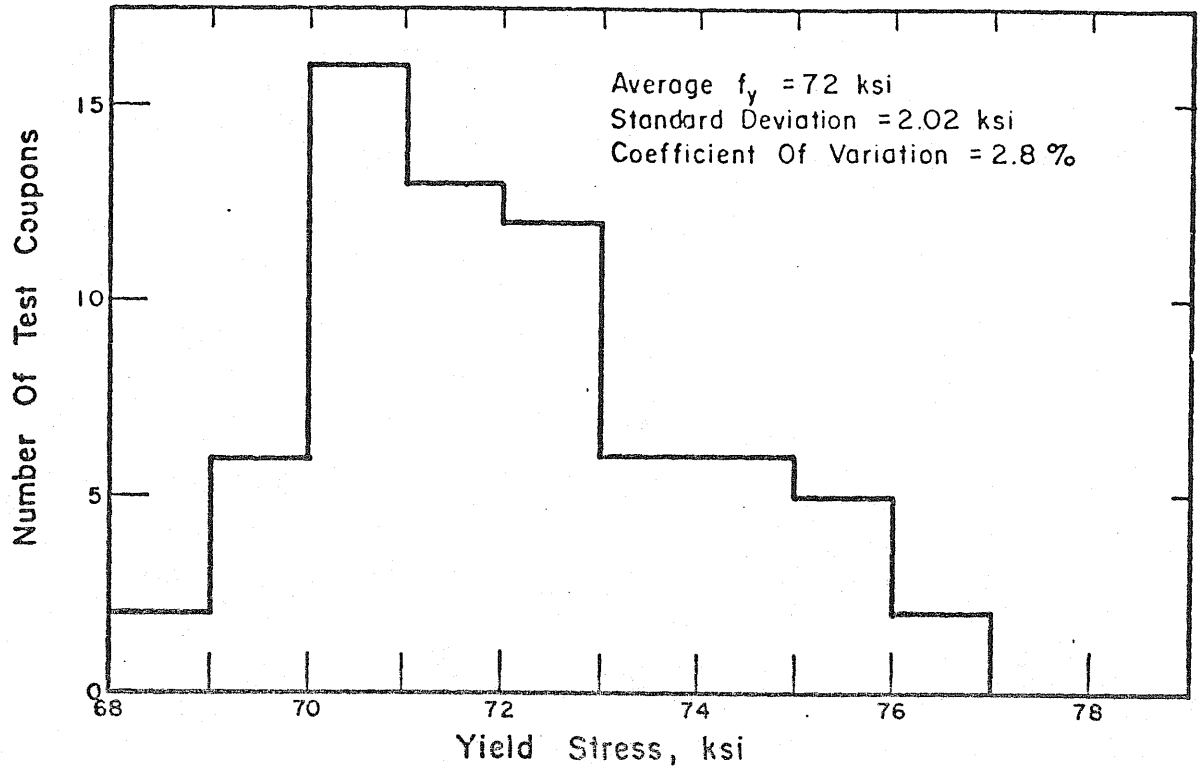

Fig. 2.6 Distribtuion of Measured Yield Stress of No. 8 Gage Wire

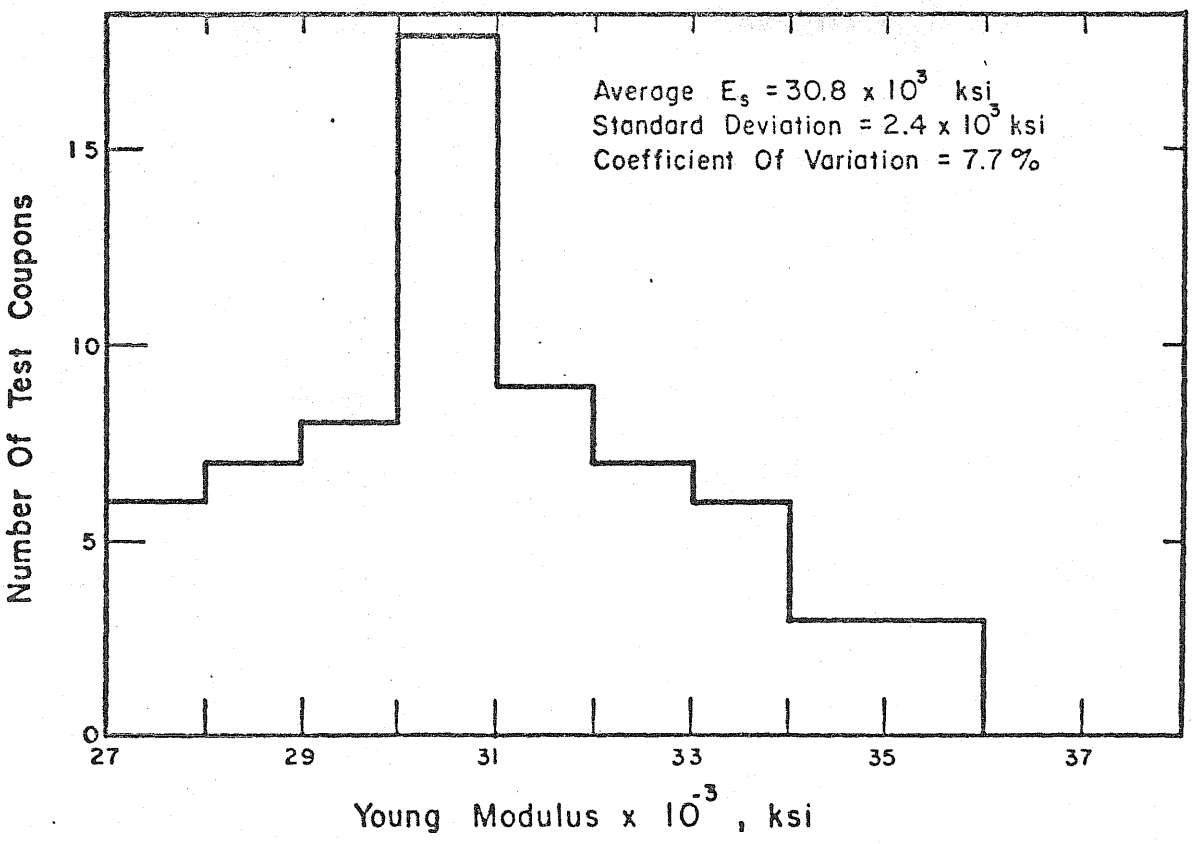

Fig. 2.7 Distribution of Measured Young's Modulus of No. 8 Gage Wire

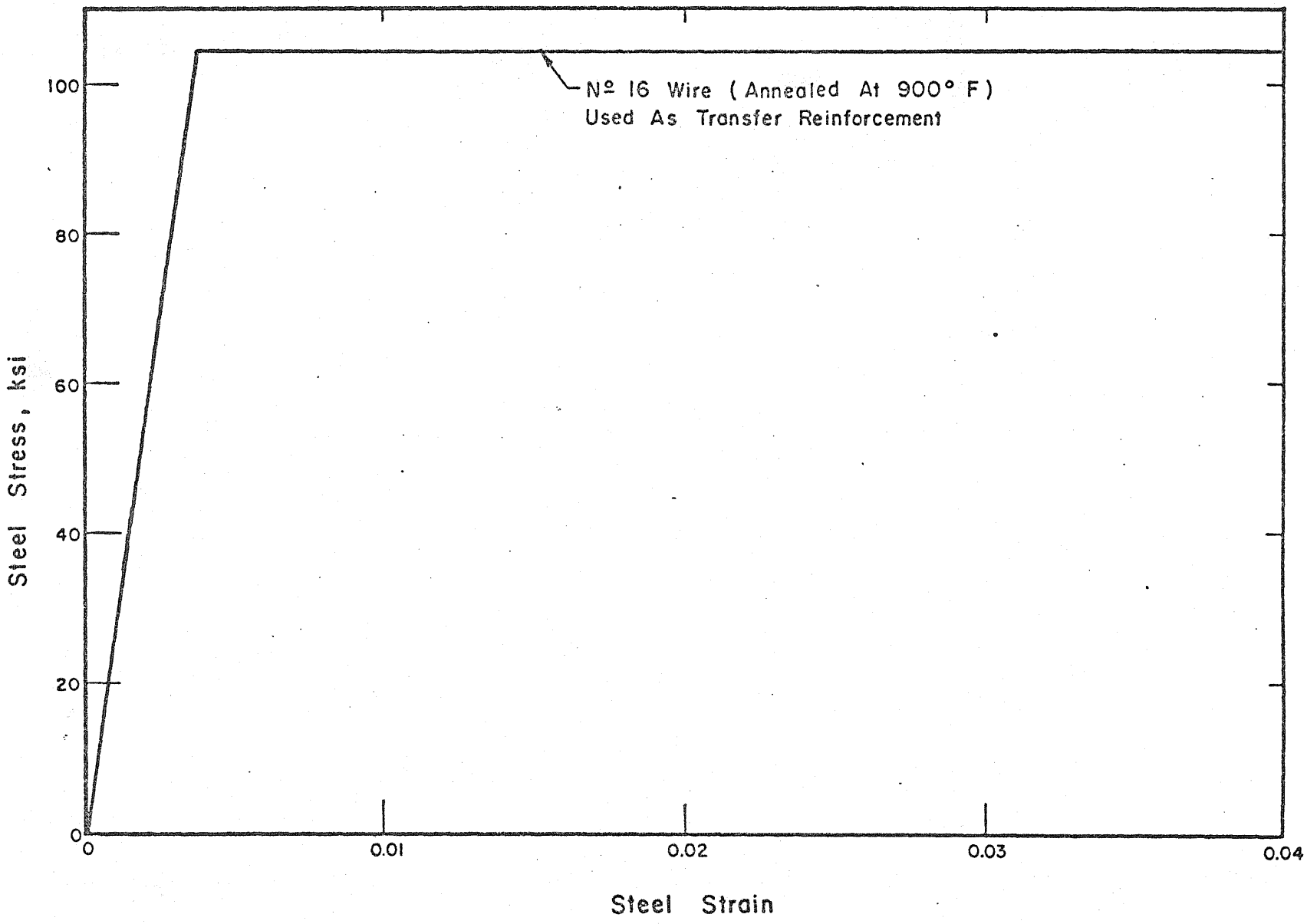

Fig. 2.8 Measured Stress-Strain Relationships for No. 16 Gage Wire

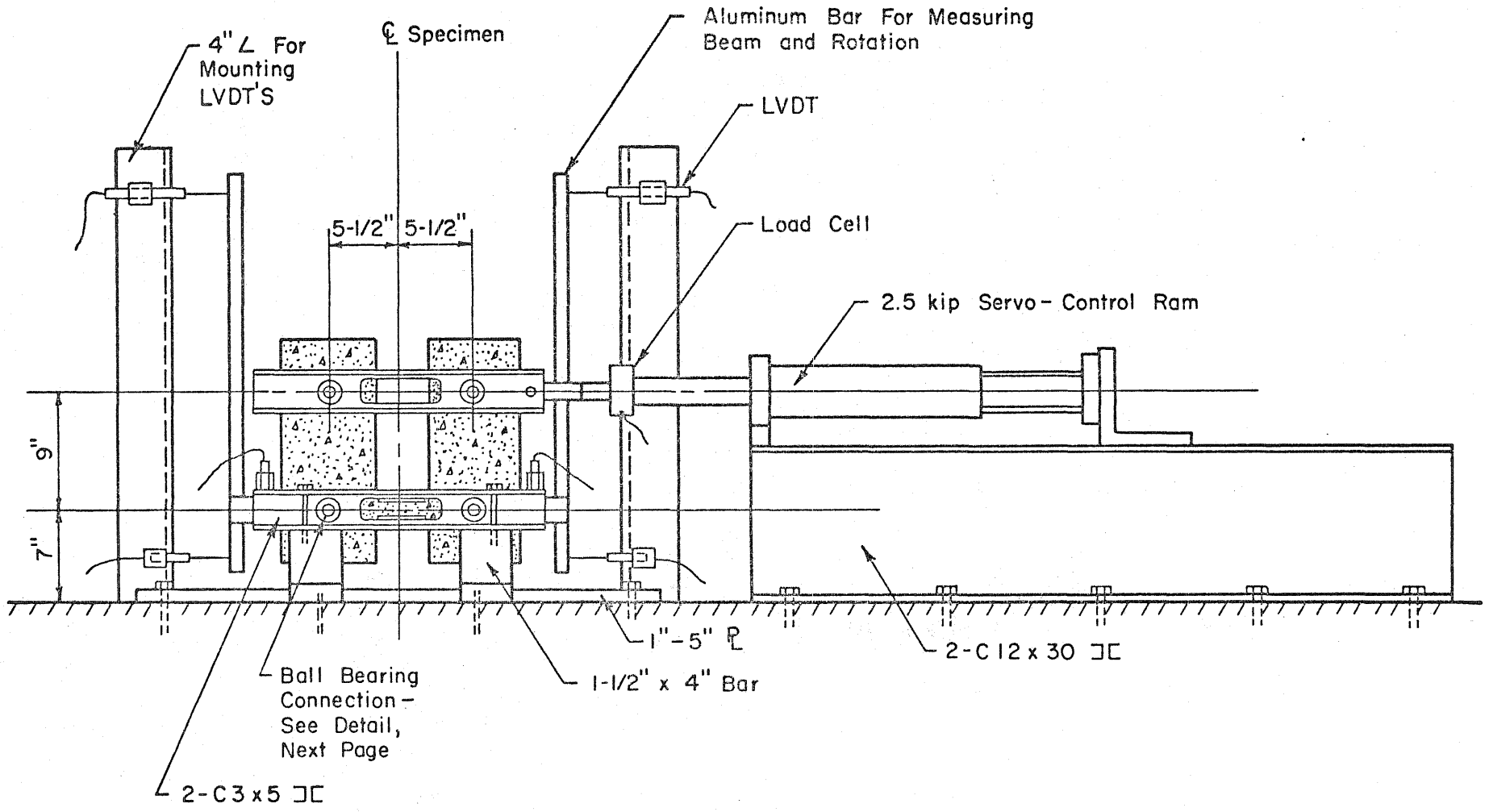

Fig. 2.9 Description of Test Setup

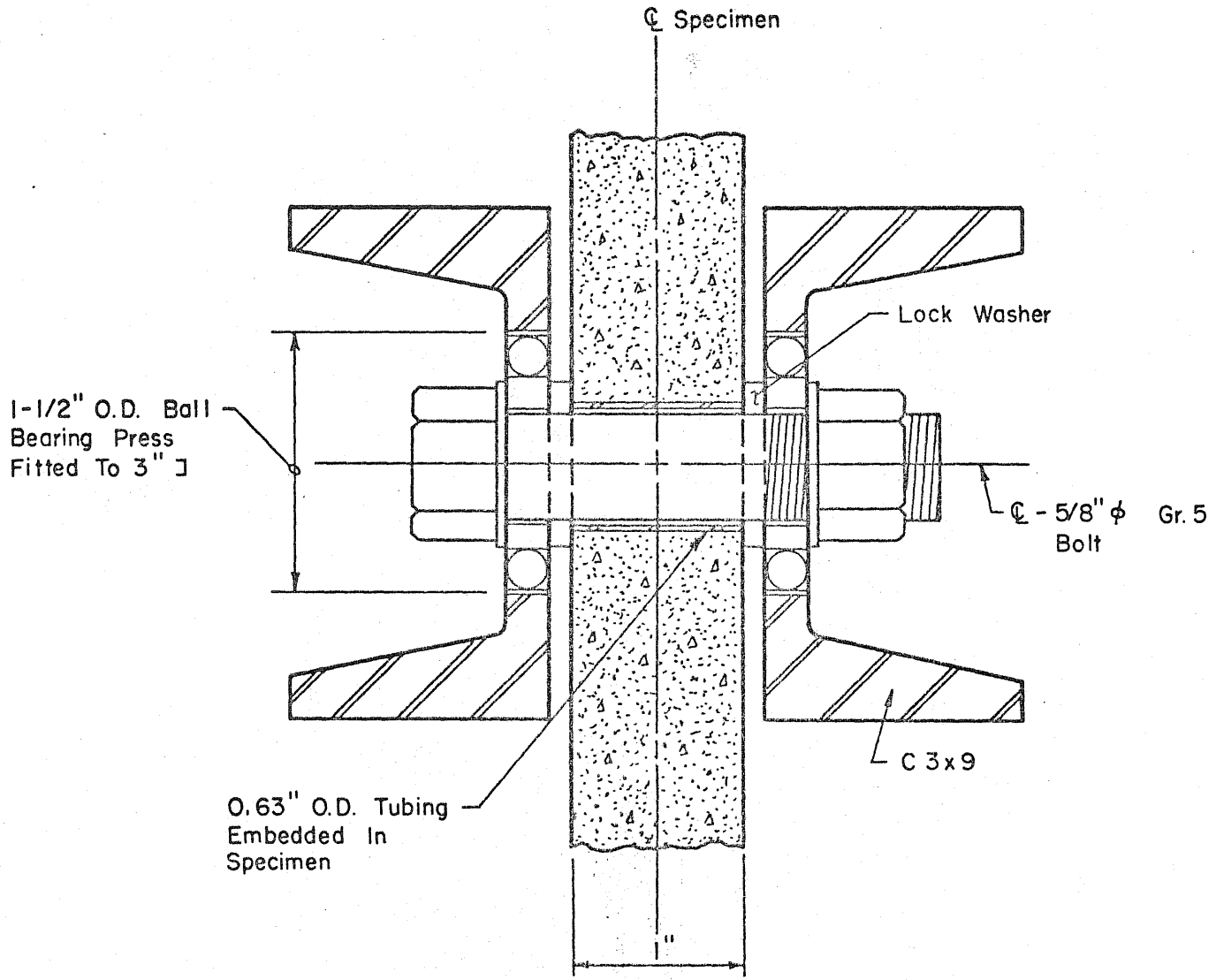

Fig. 2.10 Detail of Pin Connection

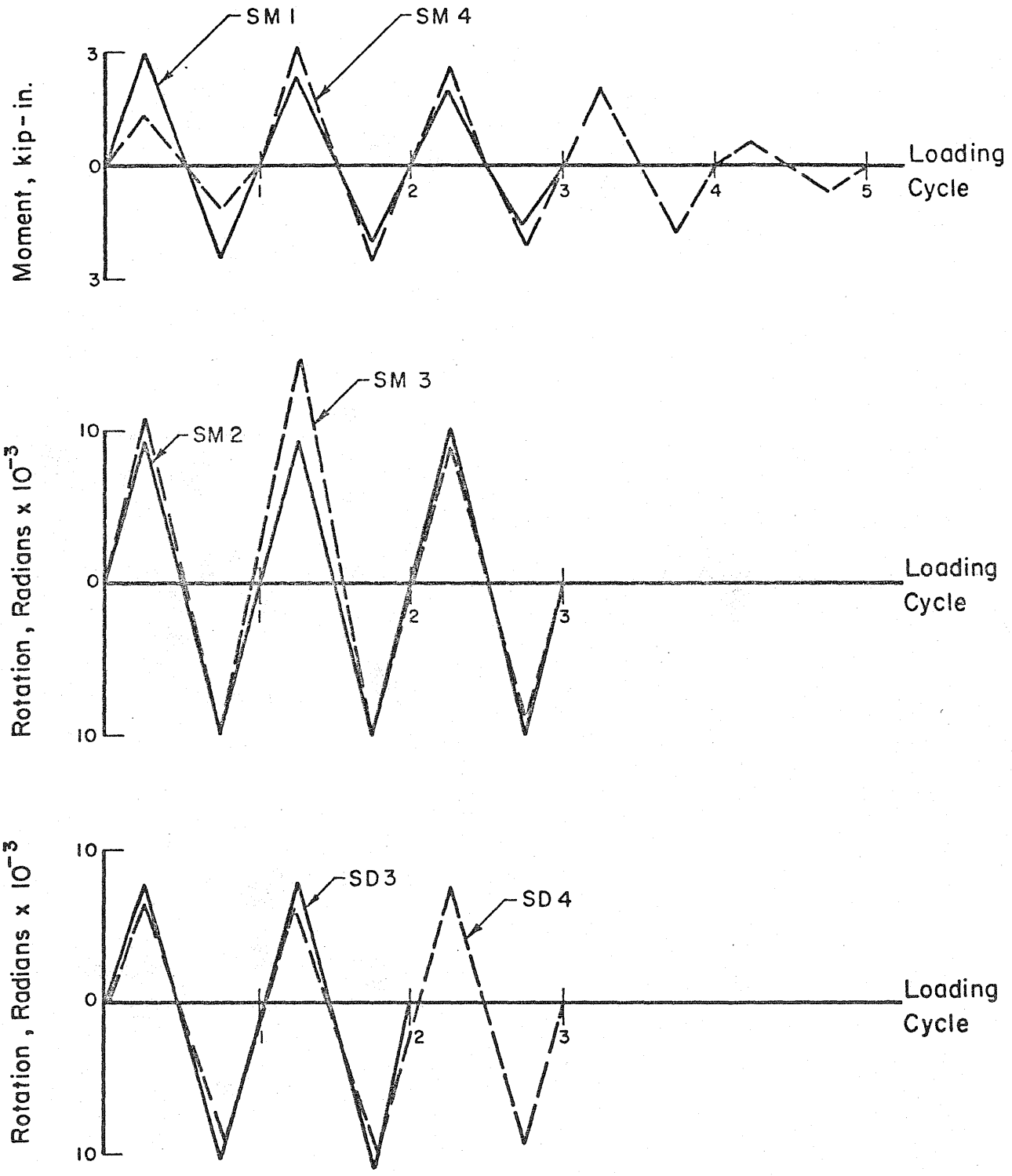

Fig. 2.11 Loading Patterns

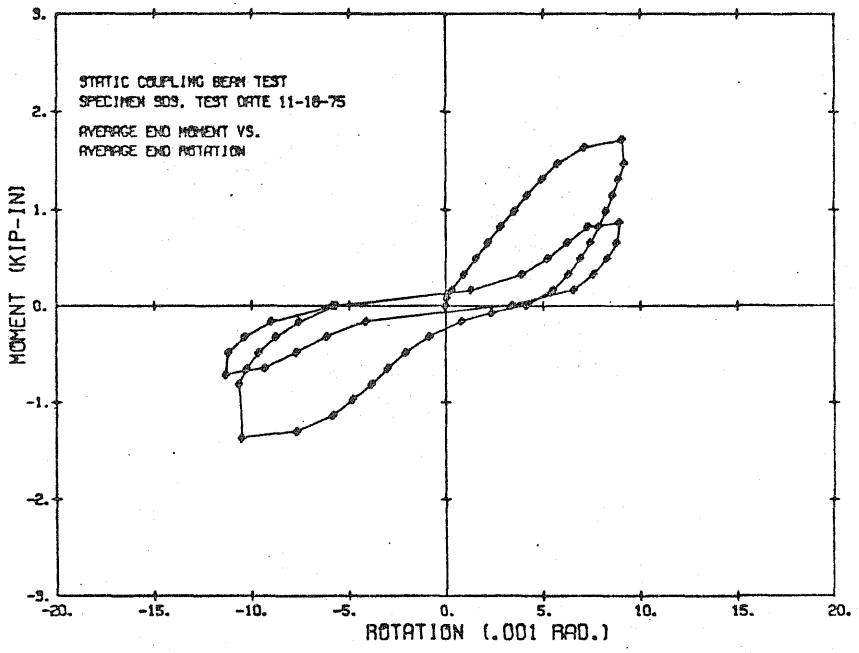

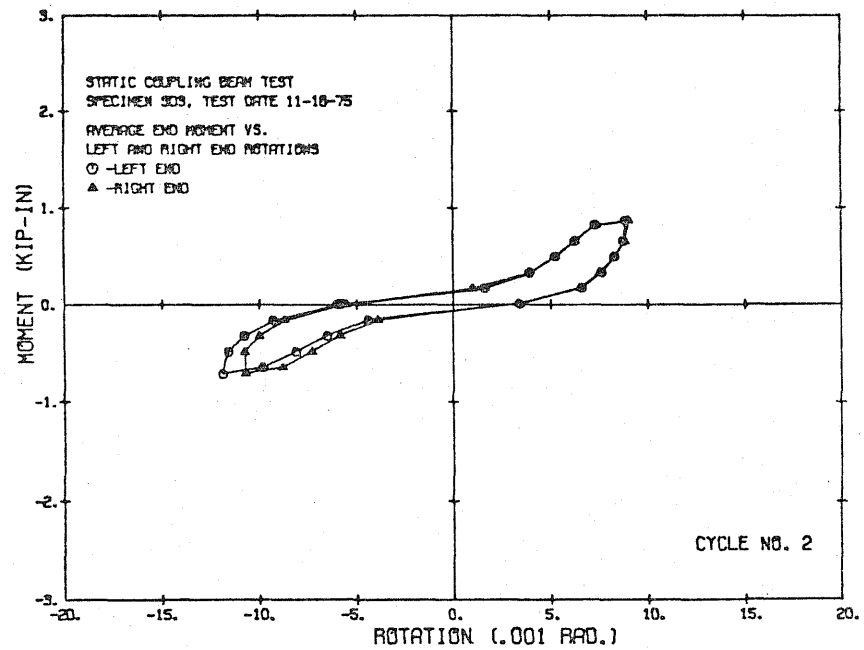

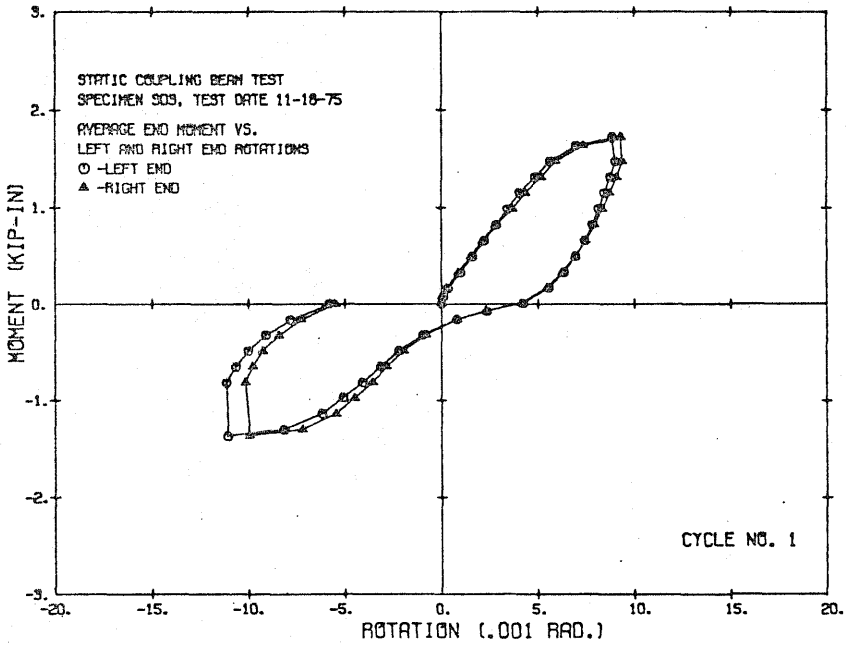

Fig. 3.1 Measured Moment-Rotation Relationship for Specimen SD3

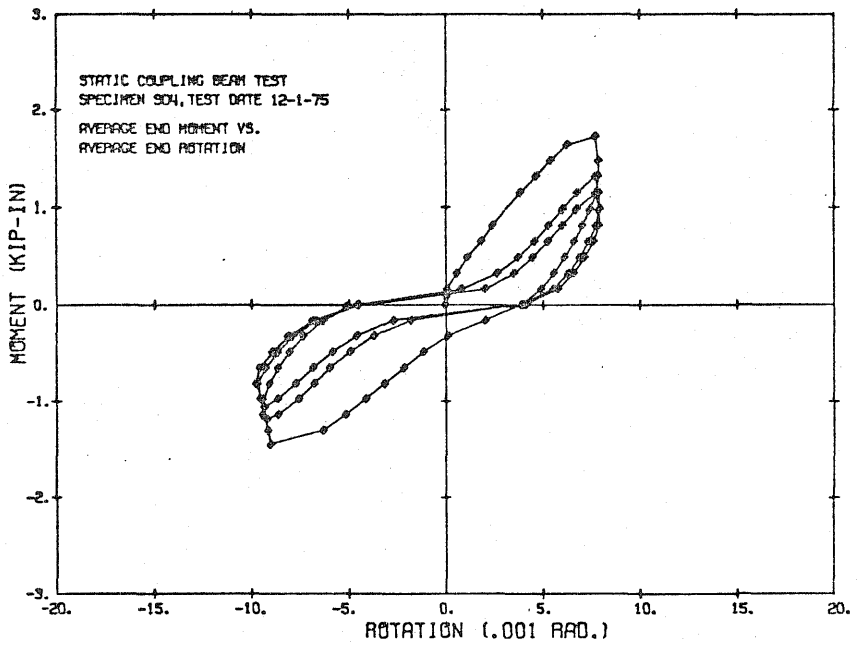

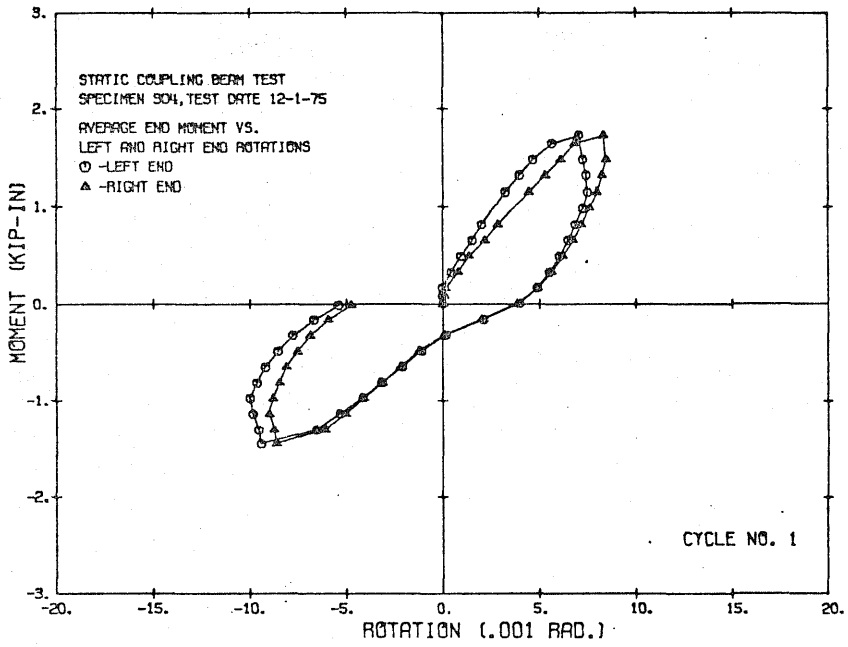

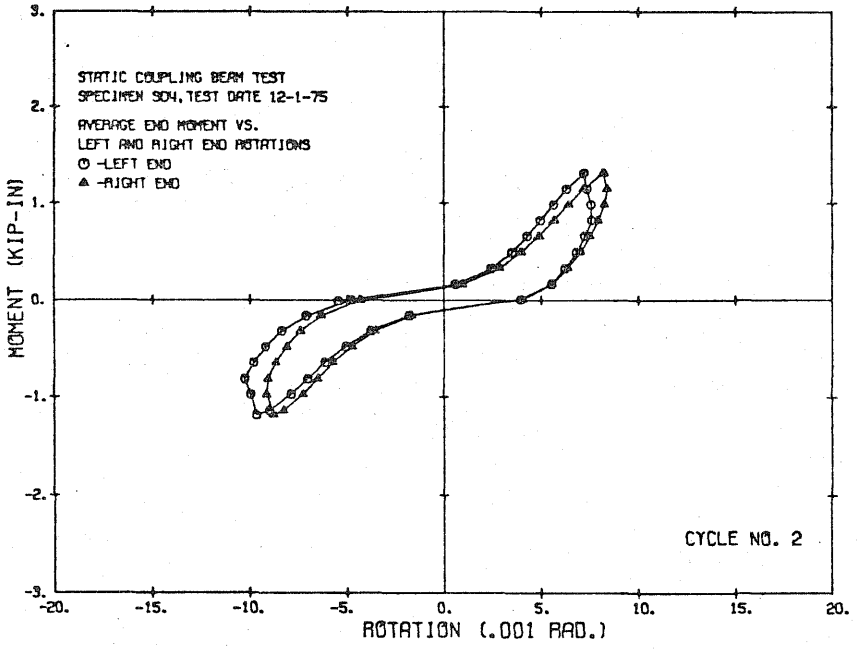

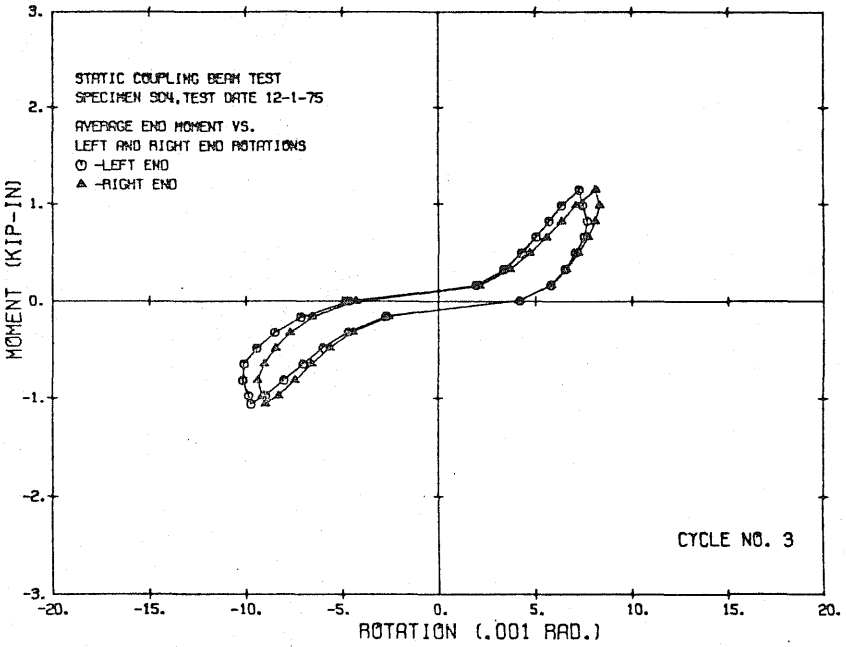

Fig. 3.2 Measured Moment-Rotation Relationship for Specimen SD4

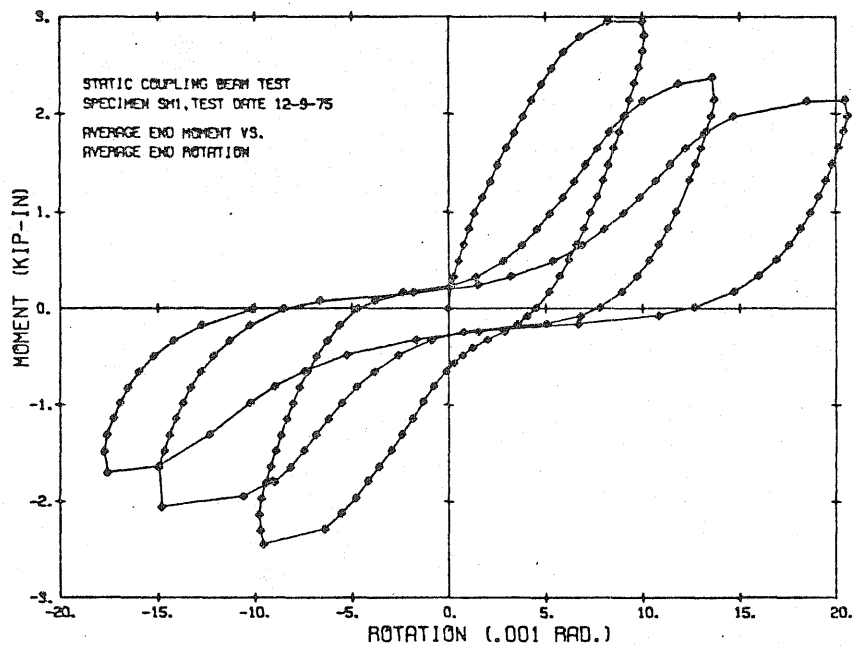

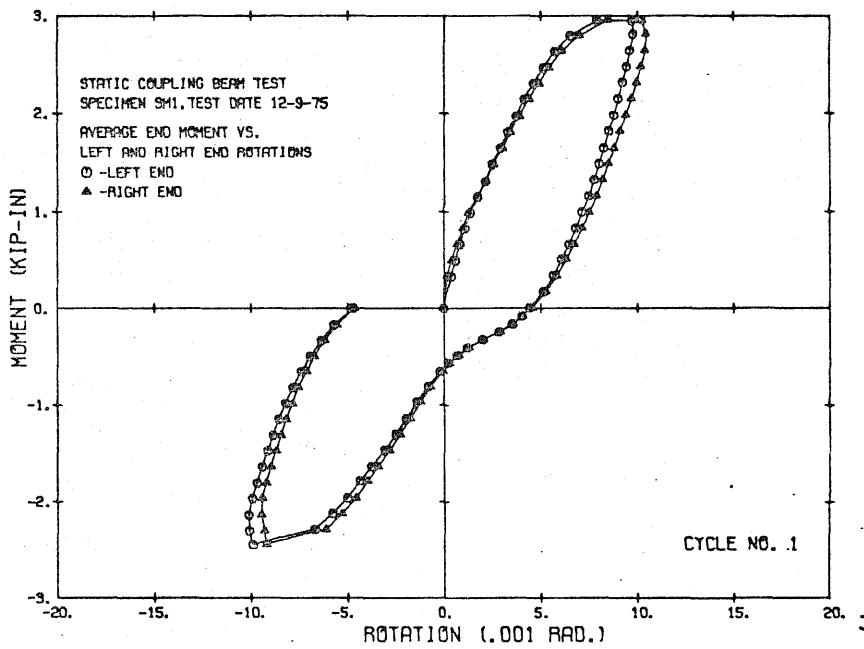

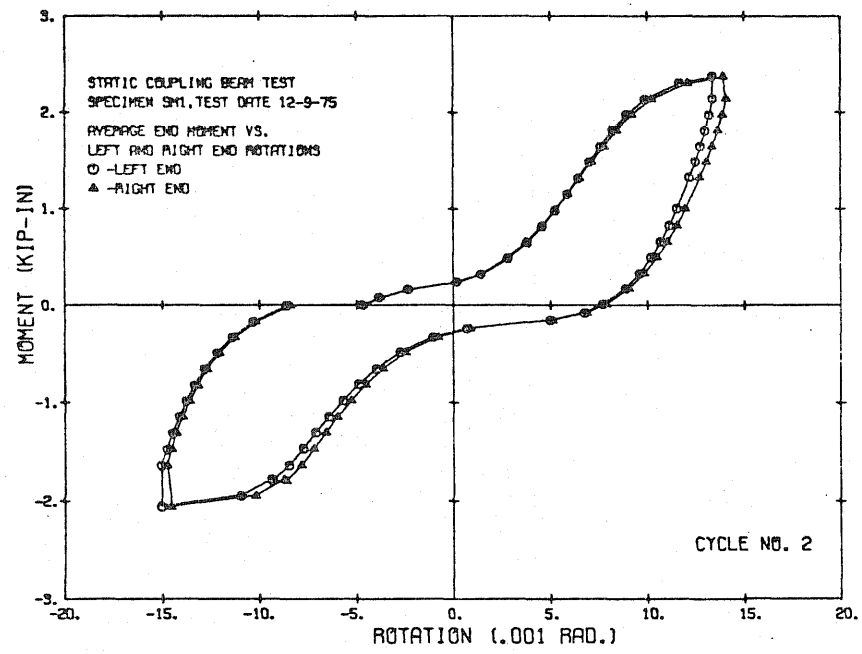

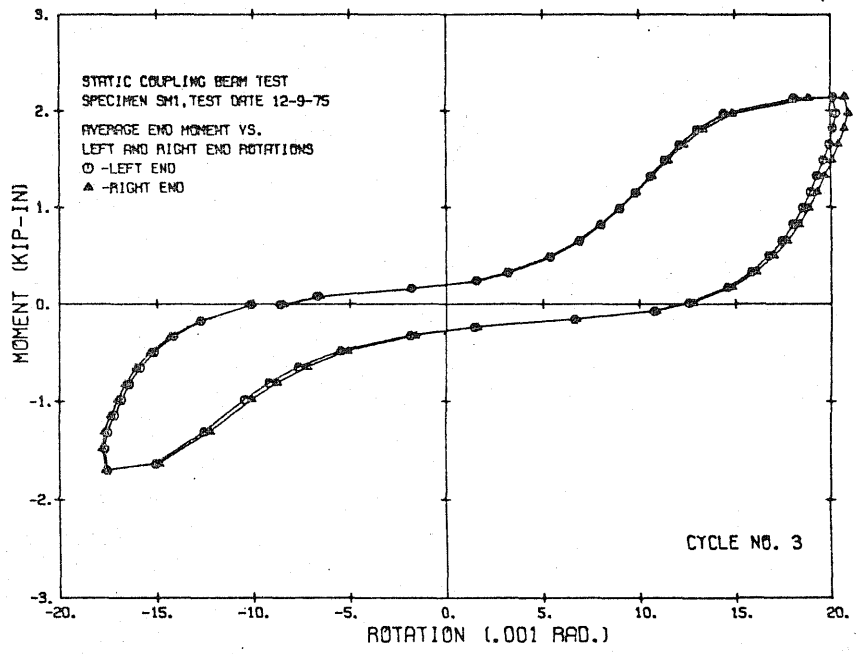

Fig. 3.3 Measured Moment-Rotation Relationship for Specimen SM1

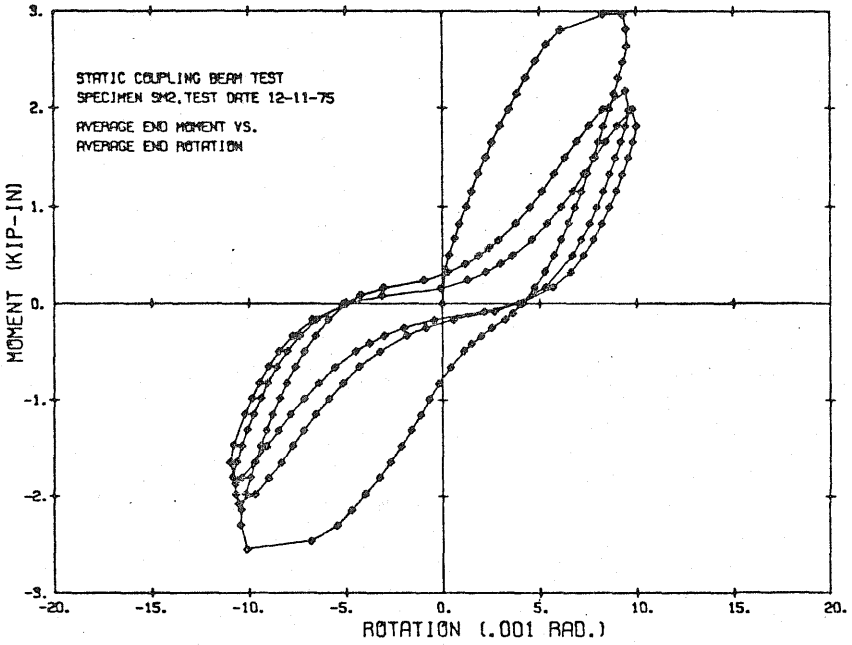

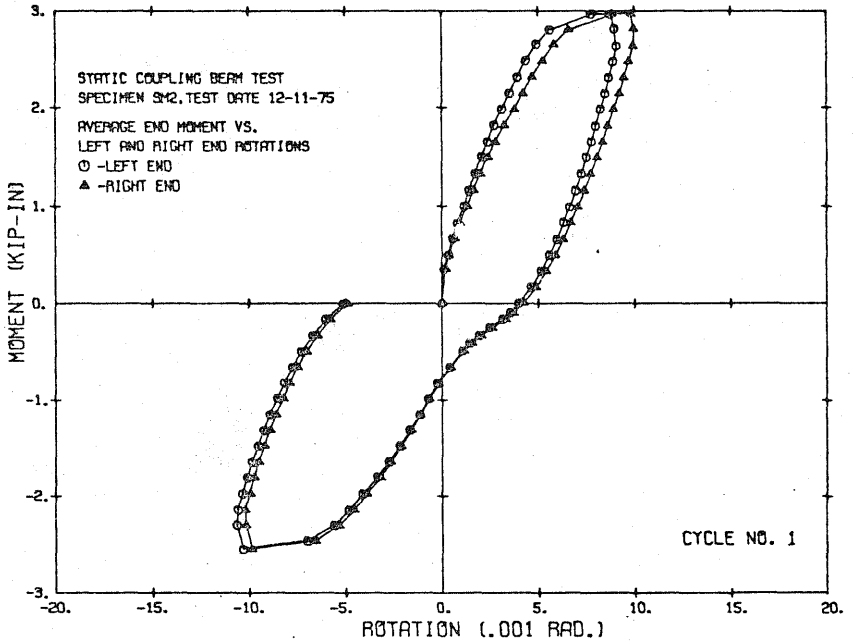

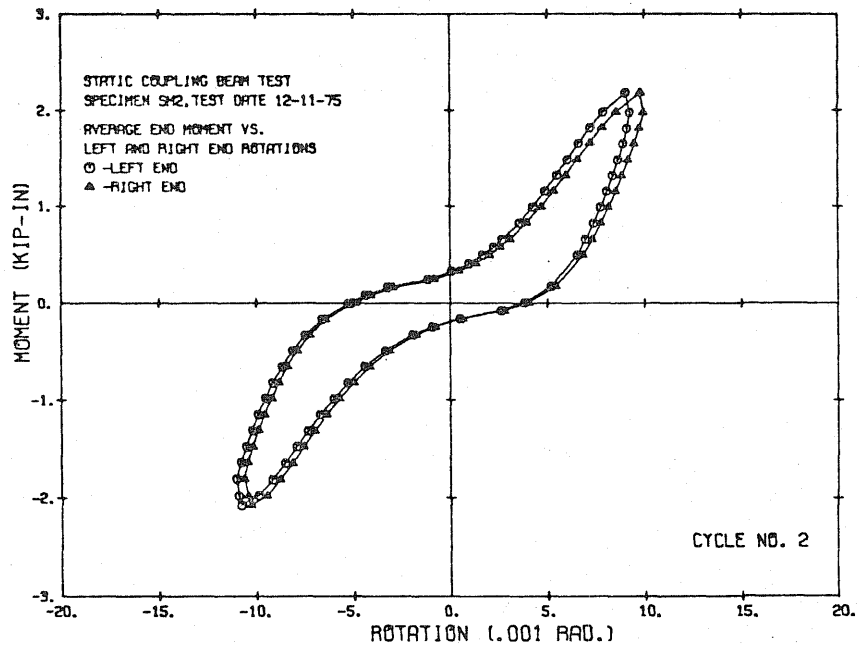

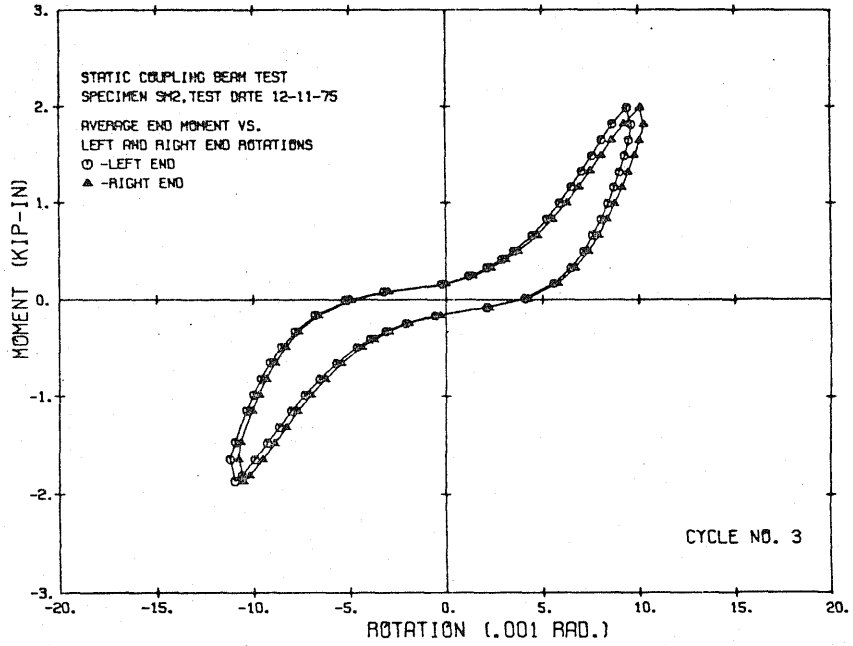

Fig. 3.4 Measured Moment-Rotation Relationship for Specimen SM2

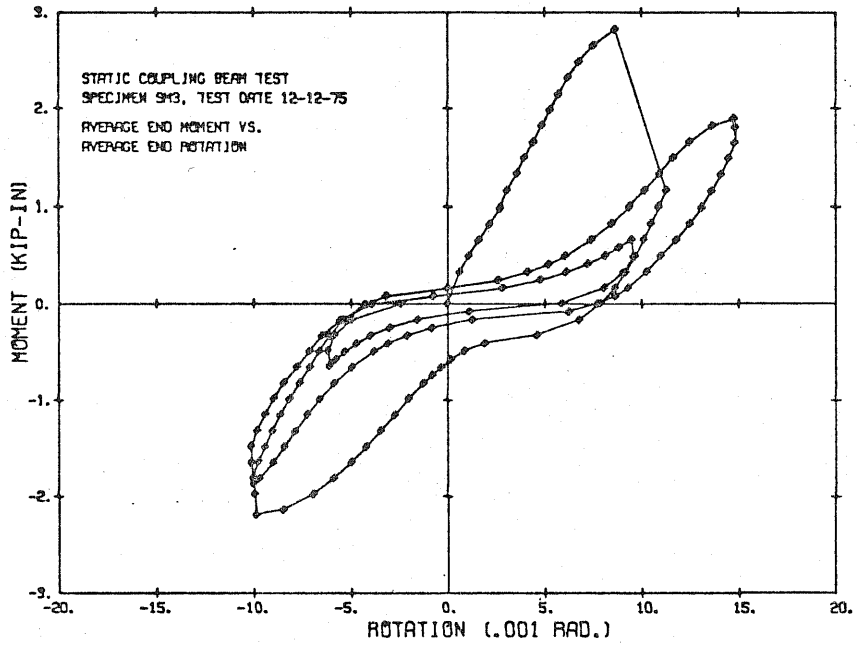

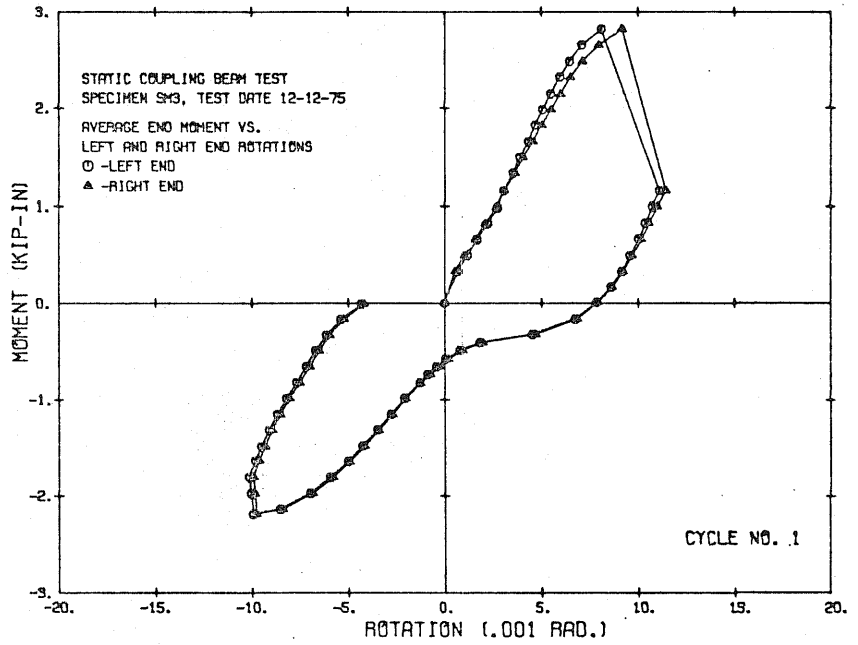

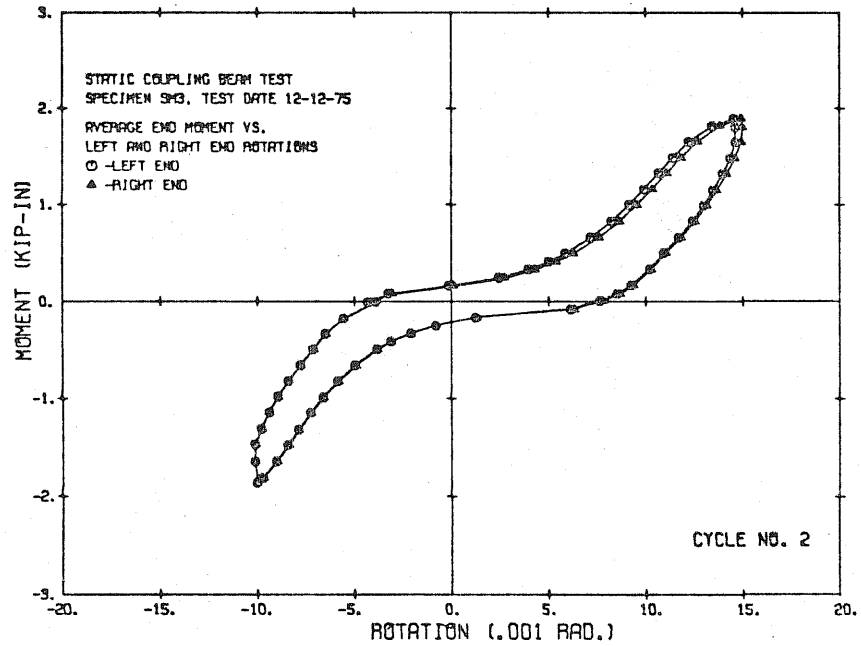

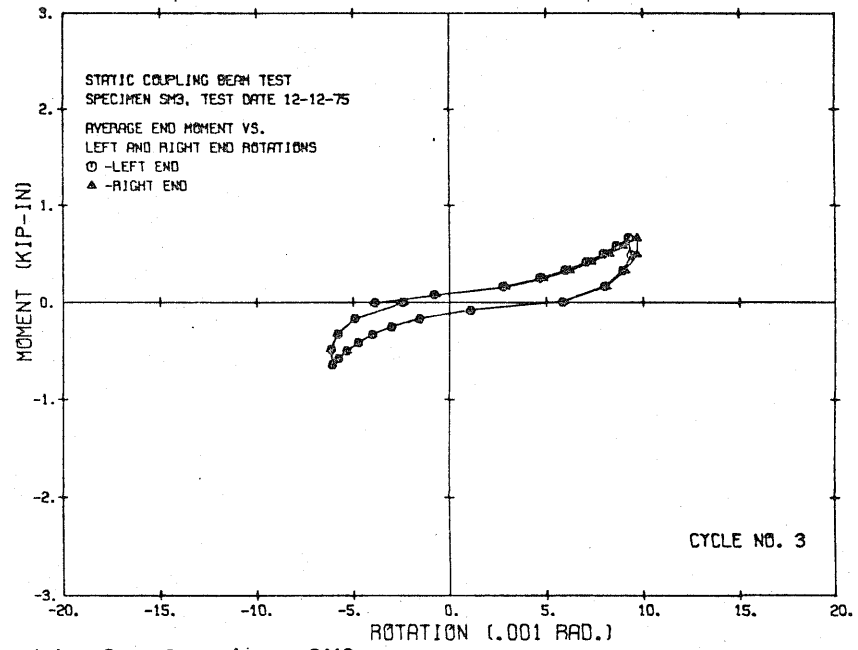

Fig. 3.5 Measured Moment-Rotation Relationship for Specimen SM3

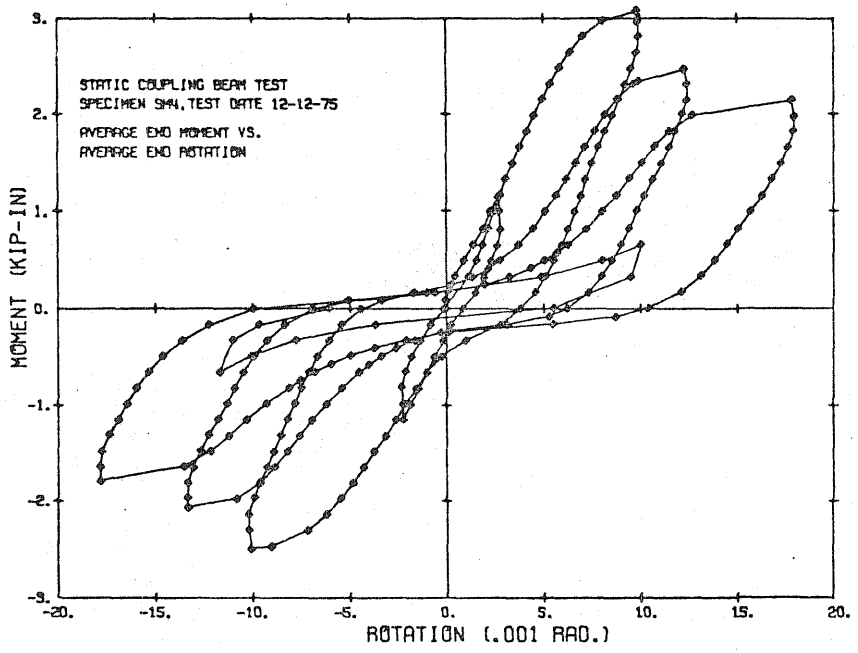

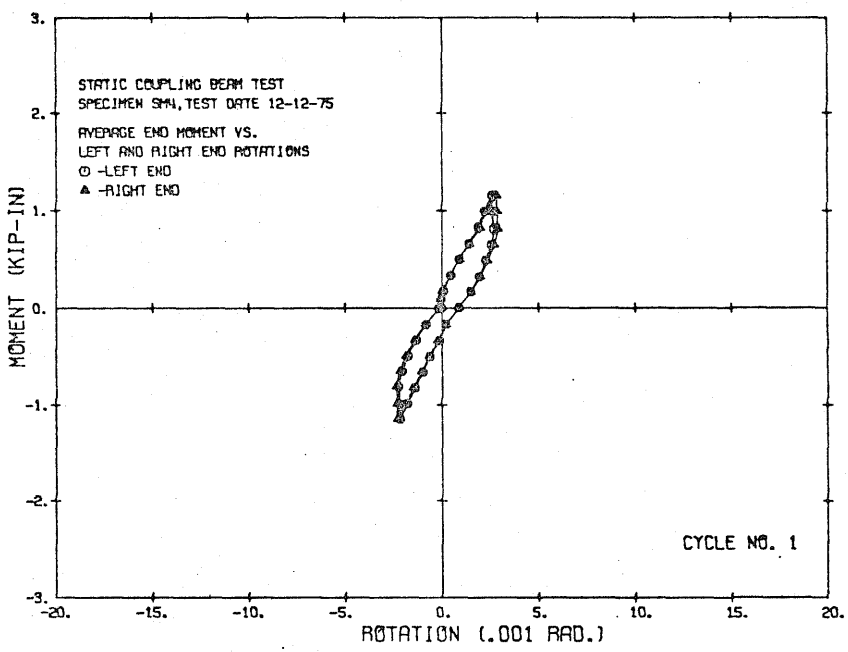

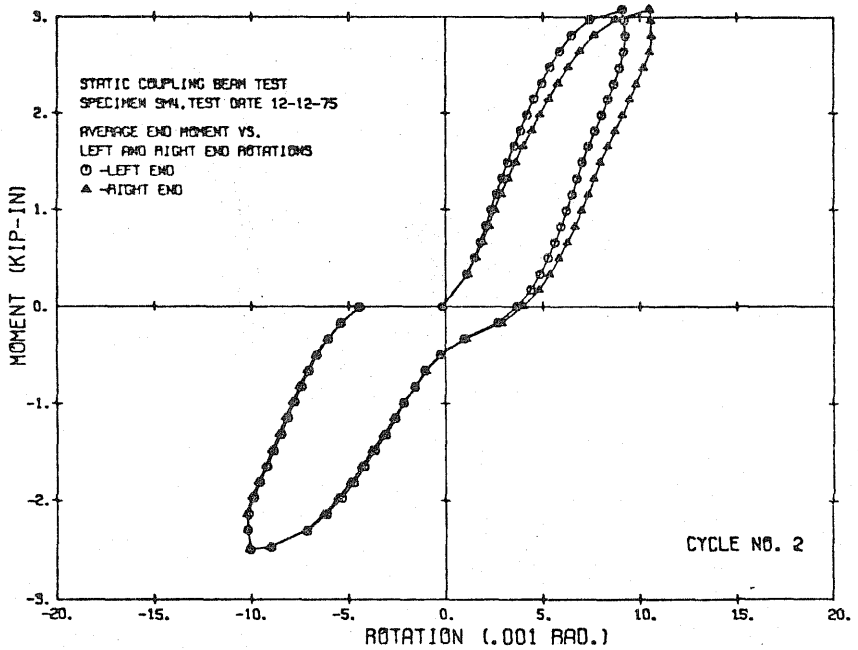

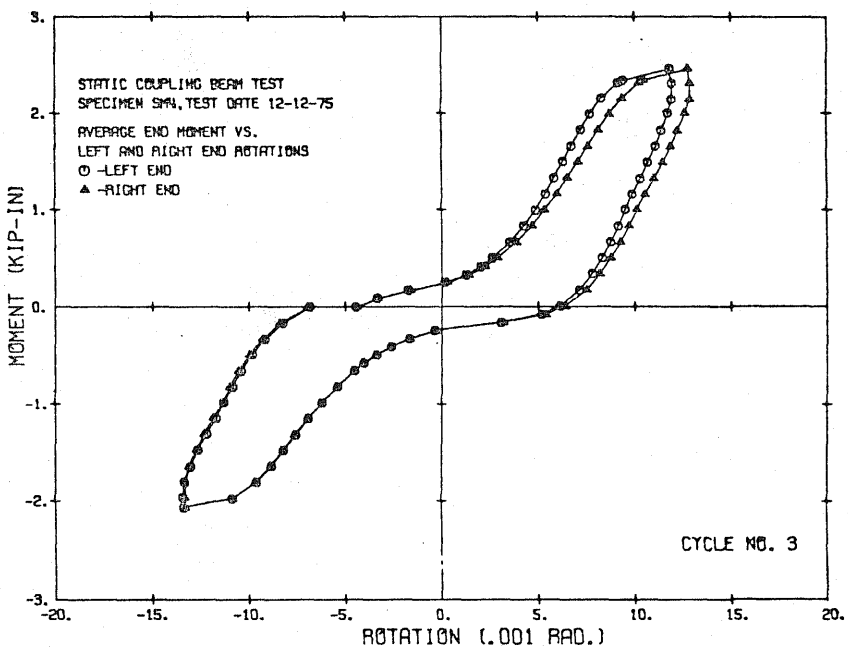

Fig. 3.6 Measured Moment-Rotation Relationship for Specimen SM4

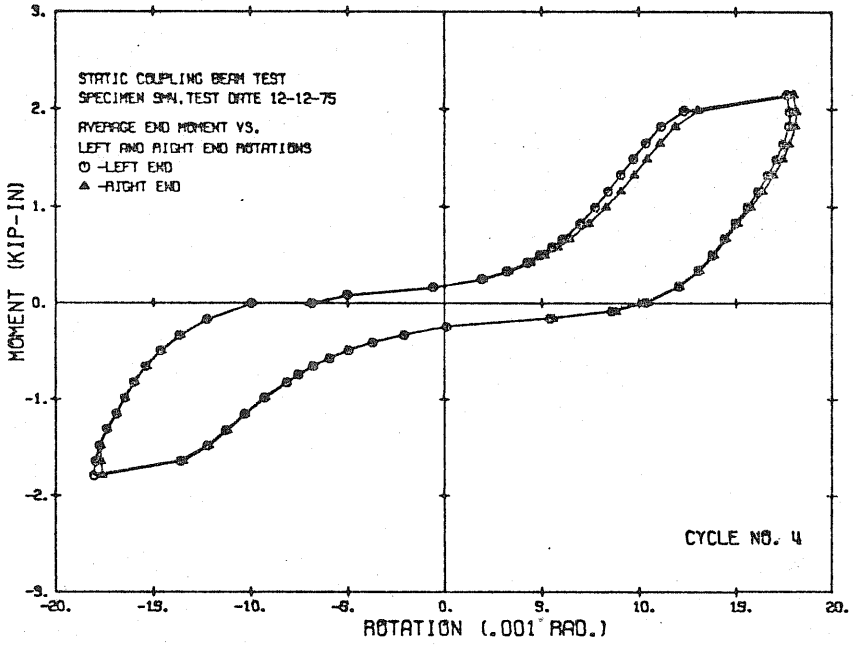

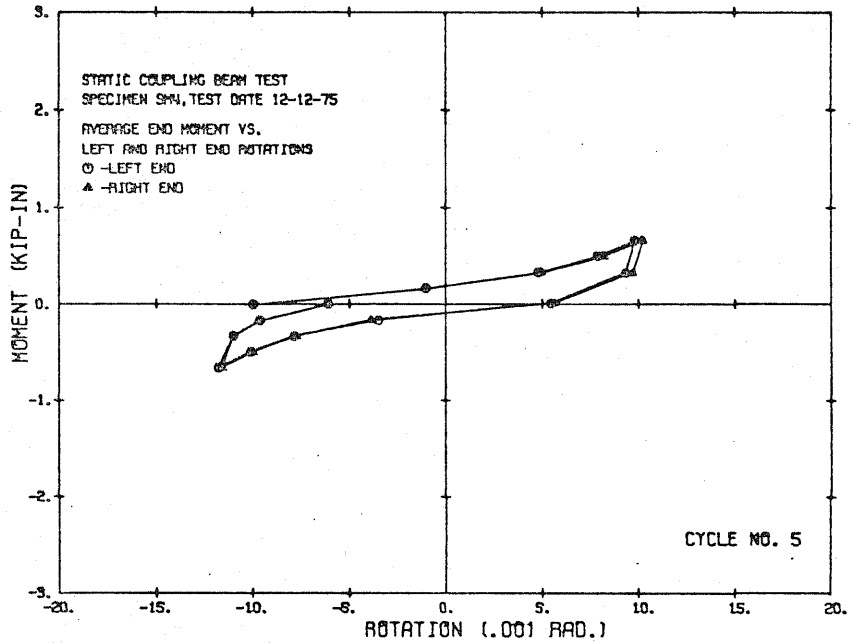

Fig. 3.6 (Continued) Measured Moment-Rotation Relationship for Specimen SM4

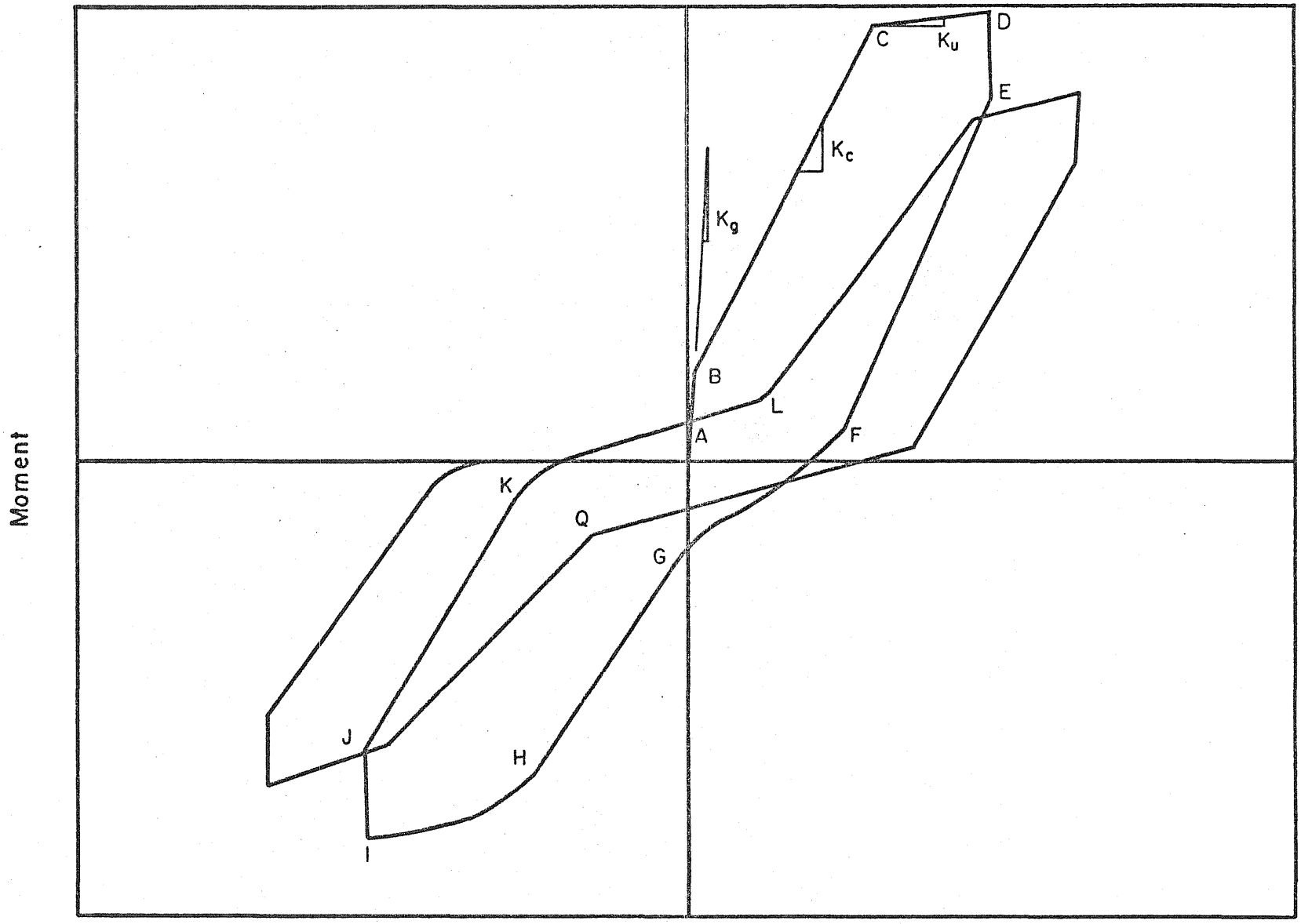

Fig. 3.7 Representative Ranges of Observed Response

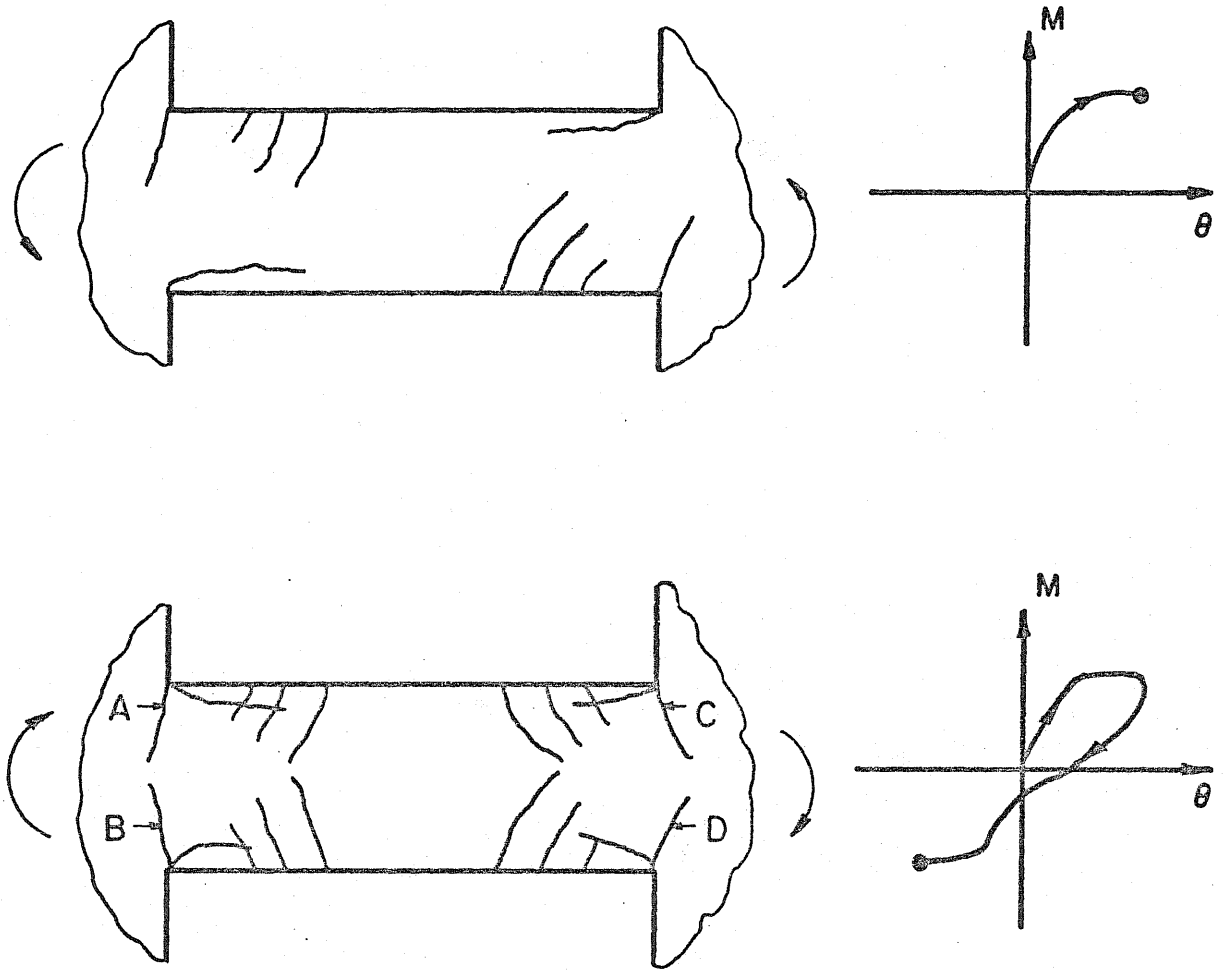

Fig. 3.8 General Pattern of Crack Development

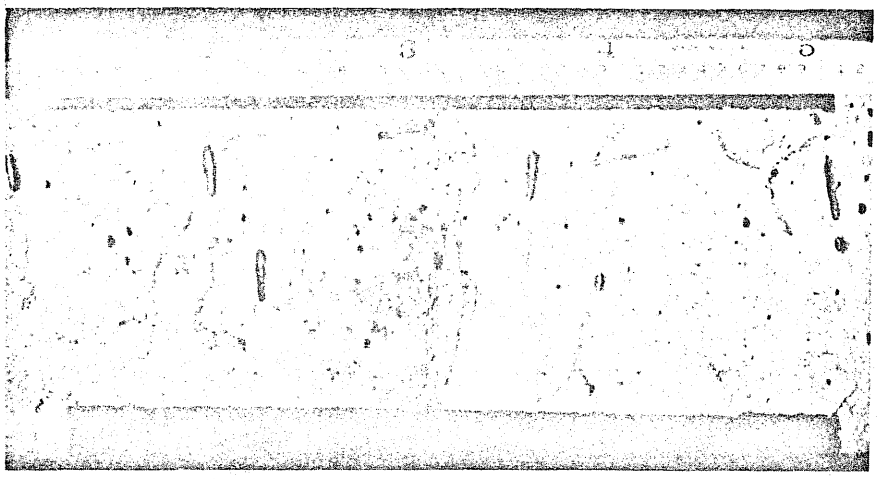

(a) First Half of First Cycle

(b) Second Half of First Cycle

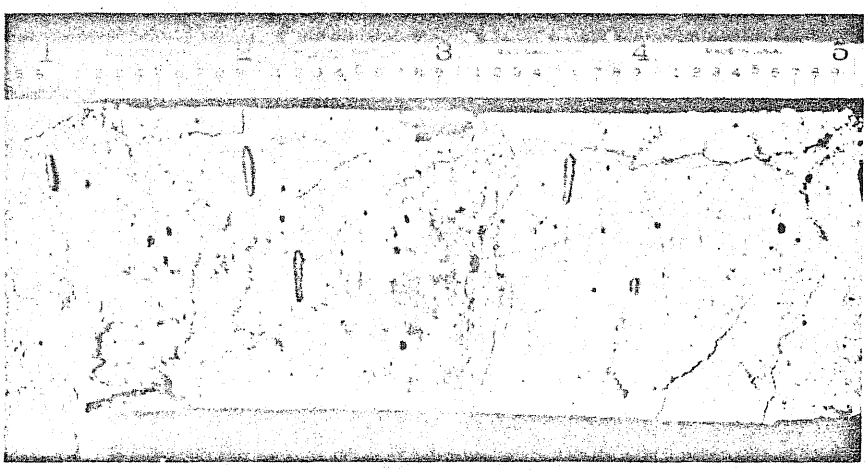

(c) First Half of Second Cycle

Fig. 3.9. Photographs of Representative Damage at Peak Loads

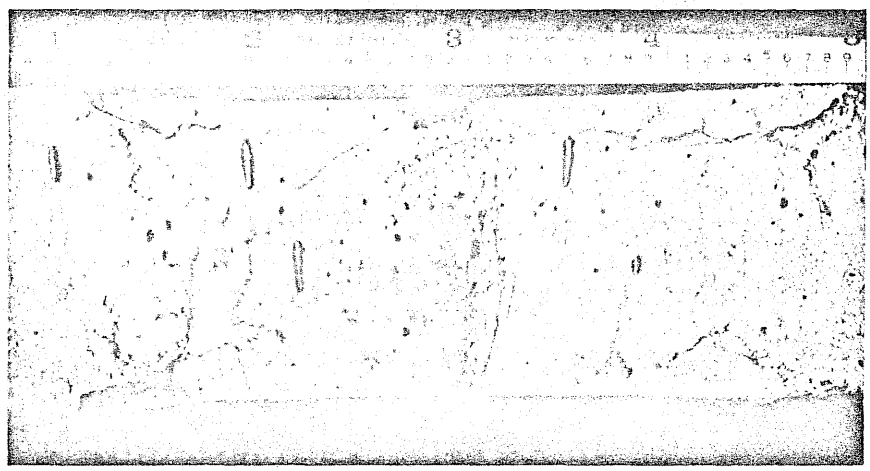

(d) Second Half of Second Cycle

(e) First Half of Third Cycle

(f) Second Half of Third Cycle

Fig. 3.9 (Continued) Photographs of Representative Damage at Peak Loads

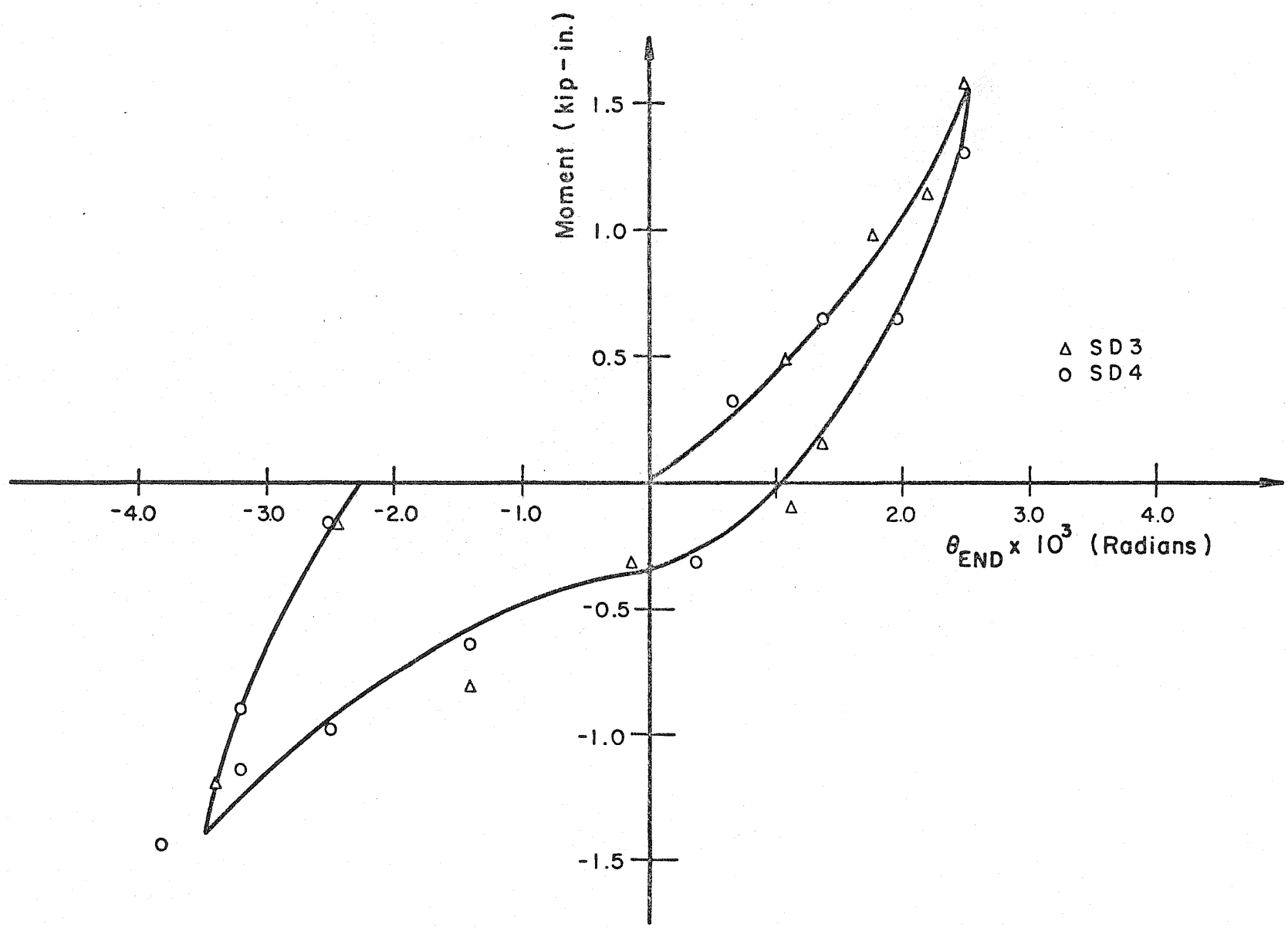

Fig. 3.10 Moment vs. Rotation Calculated from Observed Crack Width for Type SD Specimens

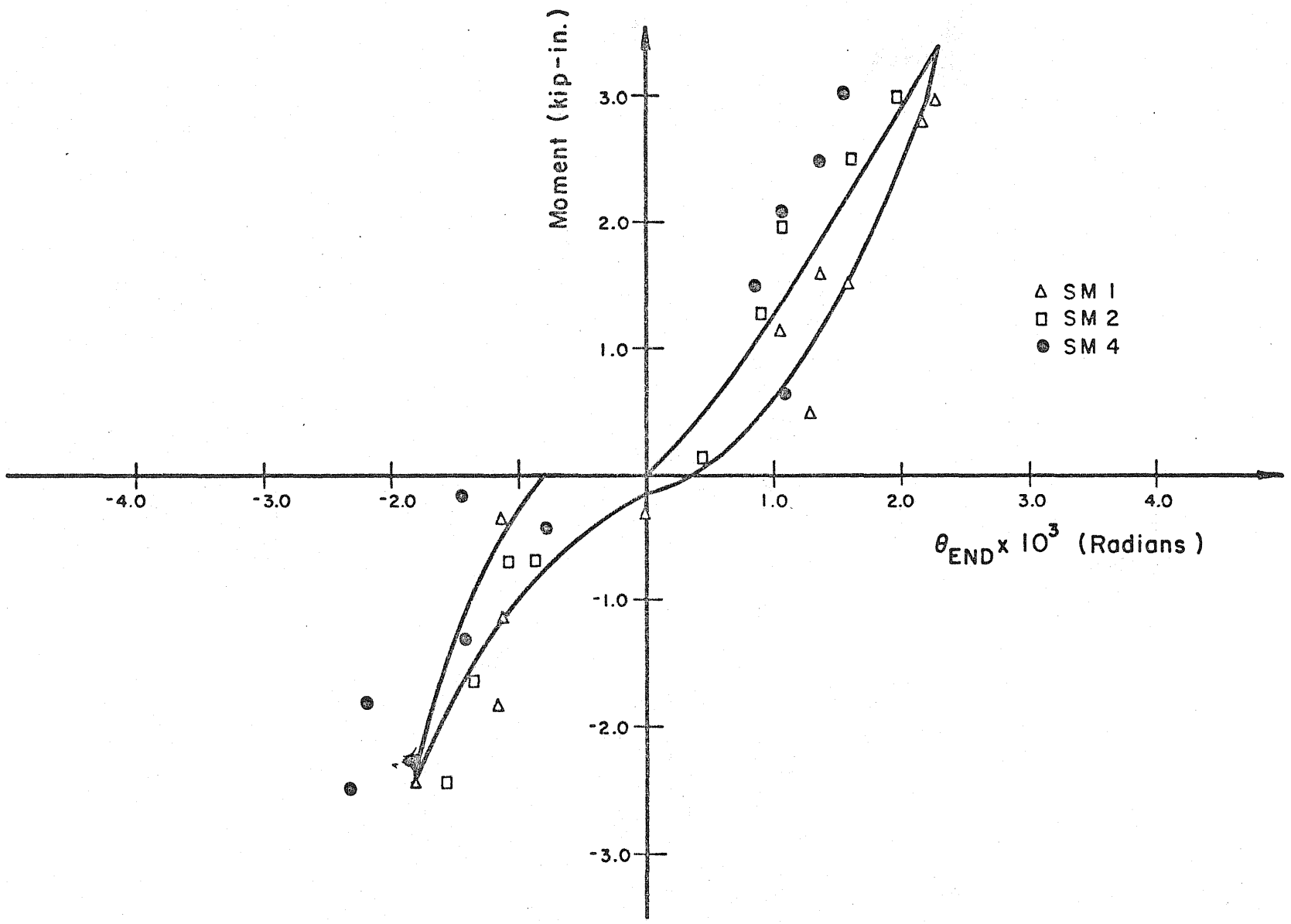

Fig. 3.11 Moment vs. Rotation Calculated from Observed Crack Width for Type SM Specimens

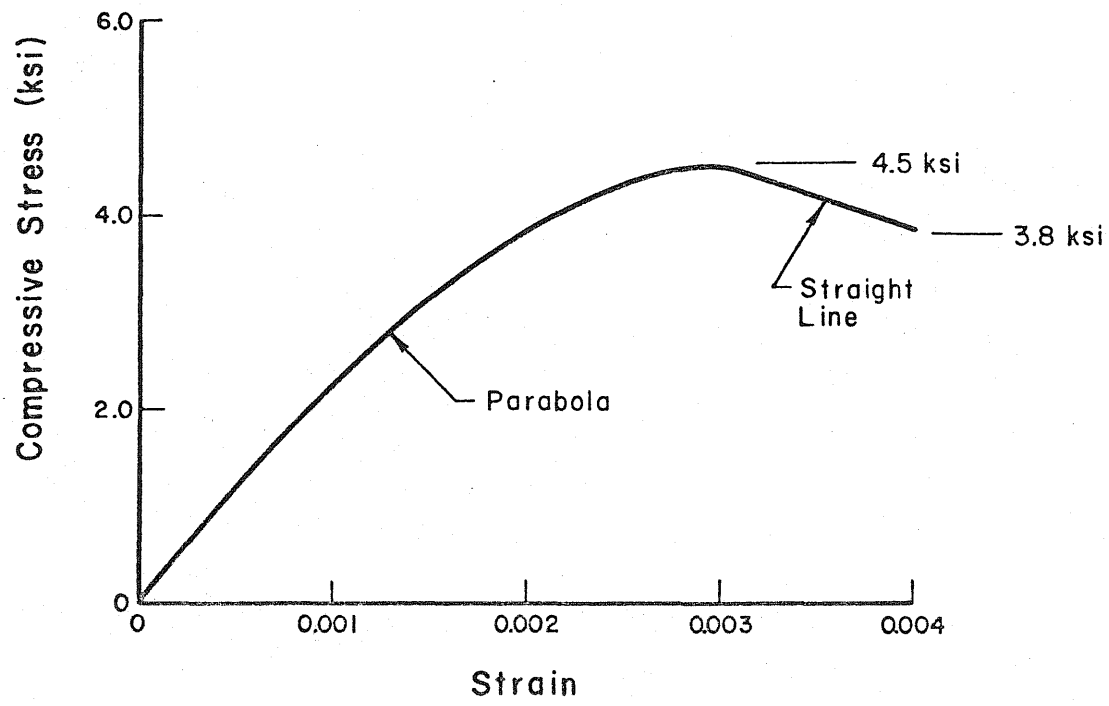

FIG. 4.1 Assumed Stress-Strain Relationship of Concrete

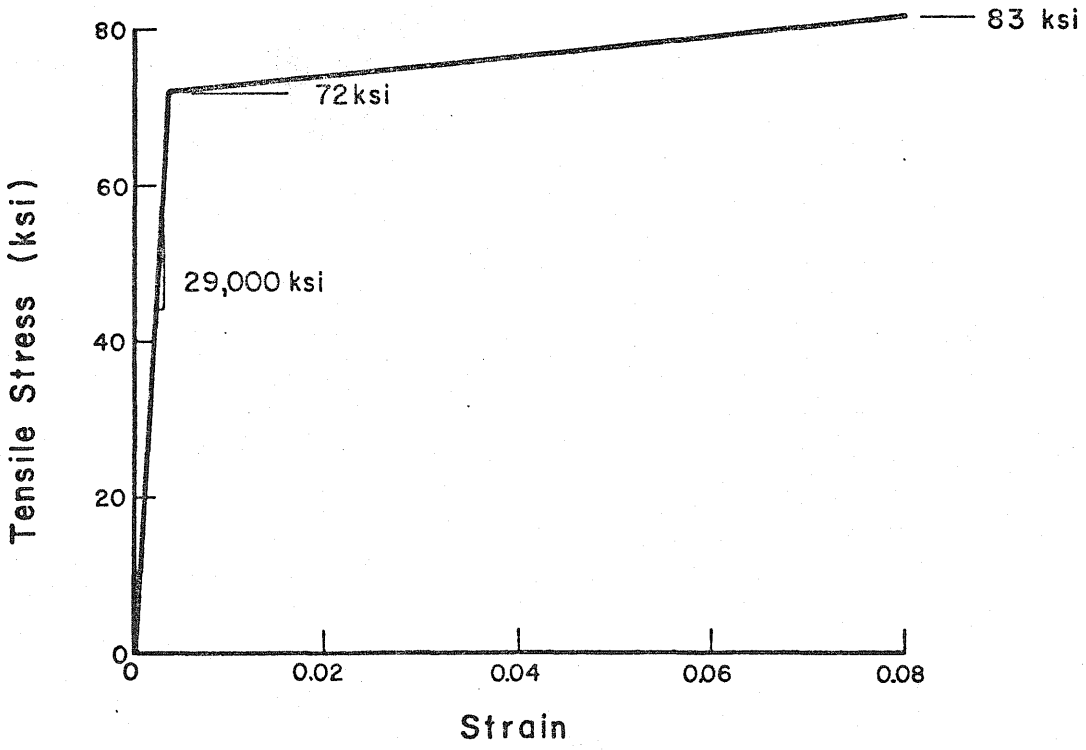

Fig. 4.2 Assumed Stress-Strain Relationship of Reinforcement

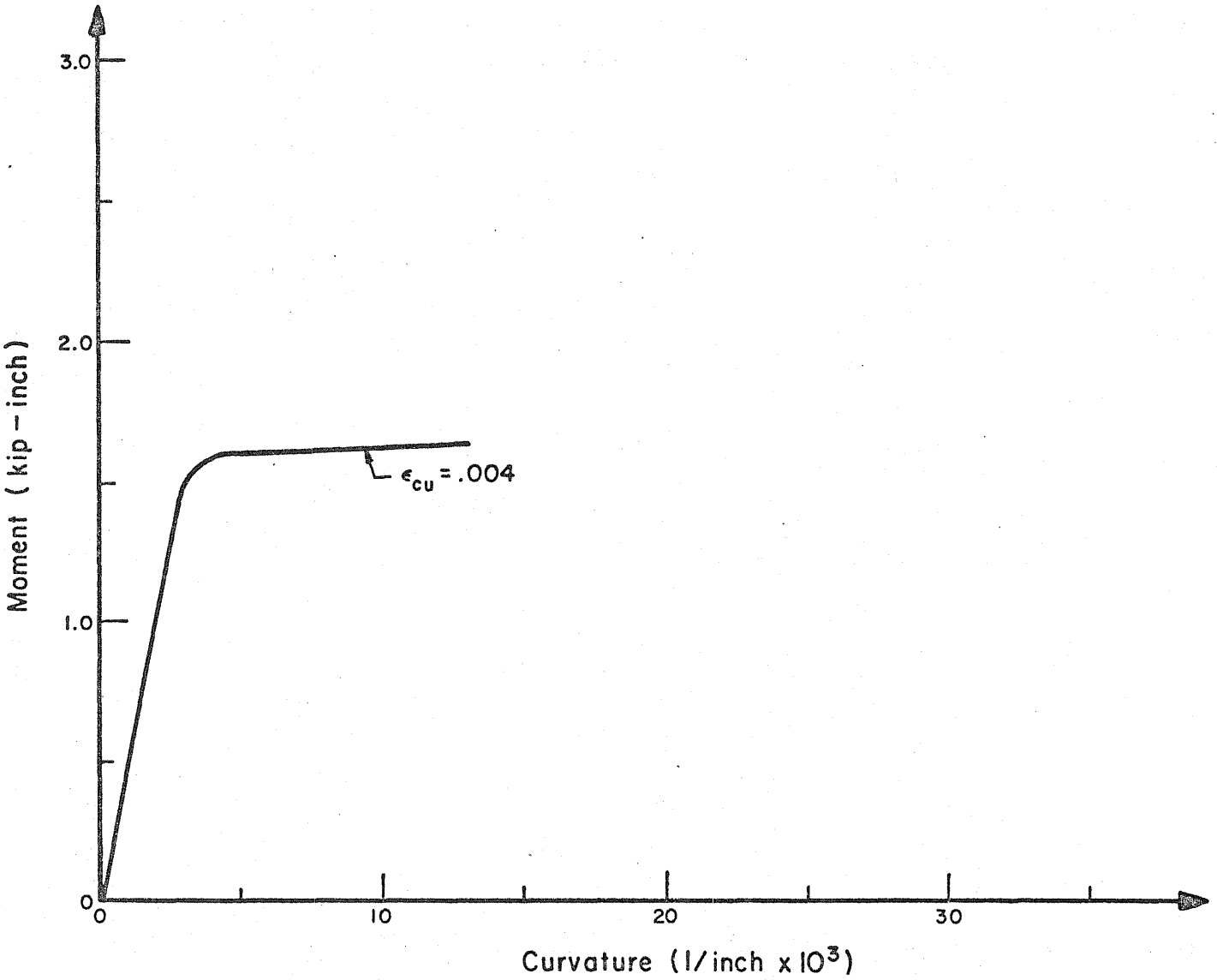

Fig. 4.3 Calculated Moment-Curvature Relationship of Type SD Specimens

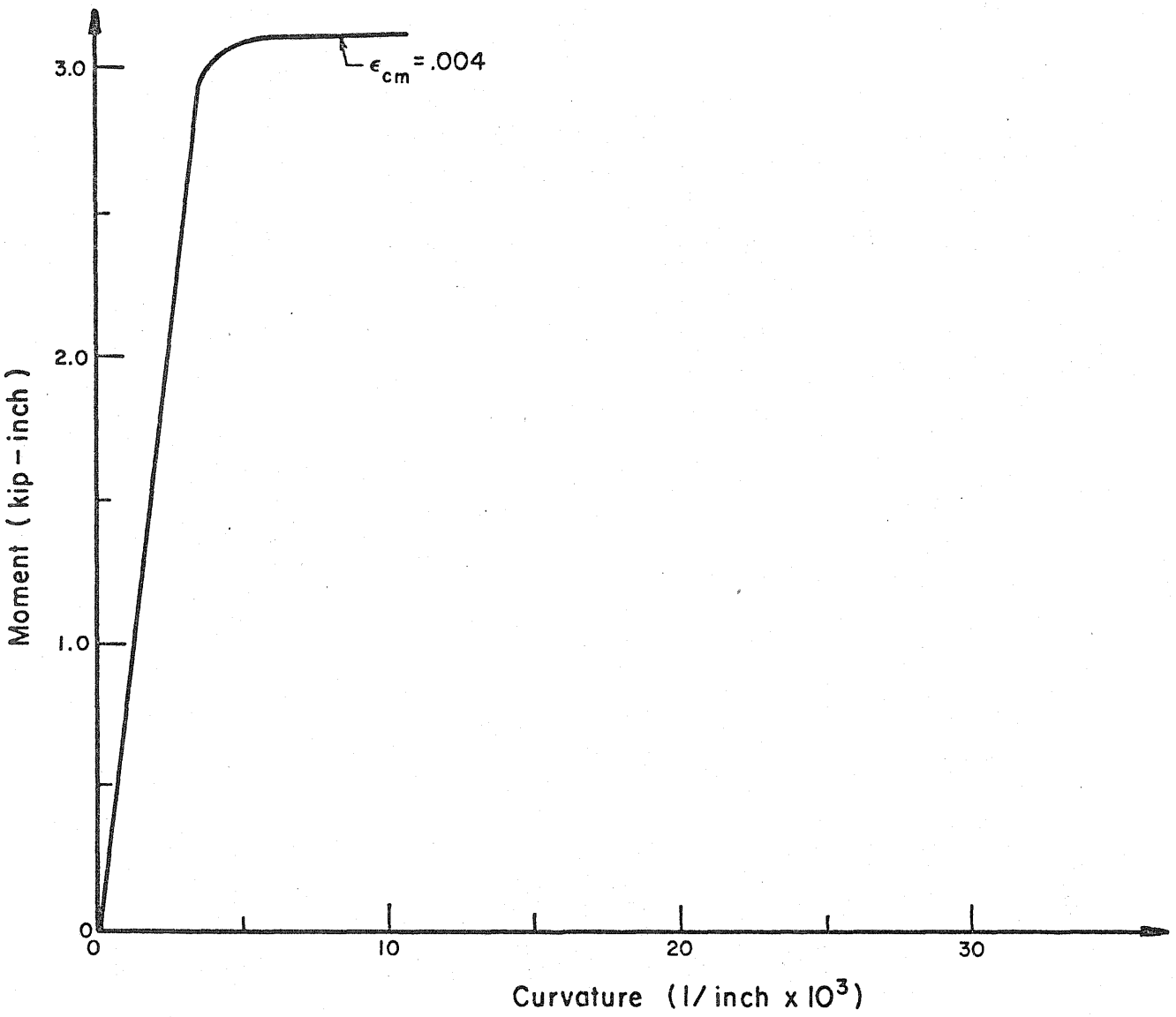

Fig. 4.4 Calculated Moment-Curvature Relationship of Type SM Specimens

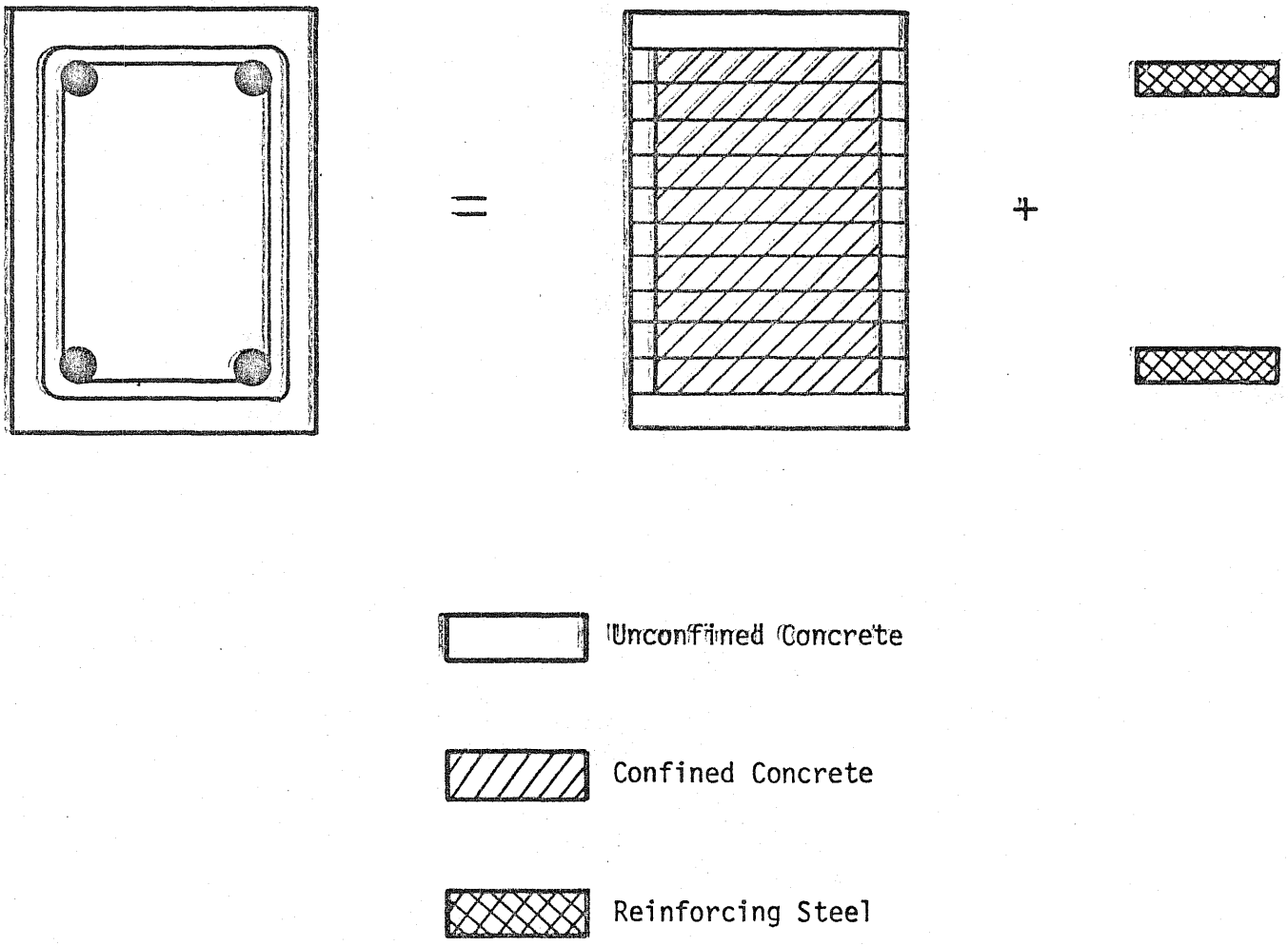

Fig. 4.5 Analytical Model of Section Used to Obtain Cyclic Moment-Curvature Relationship

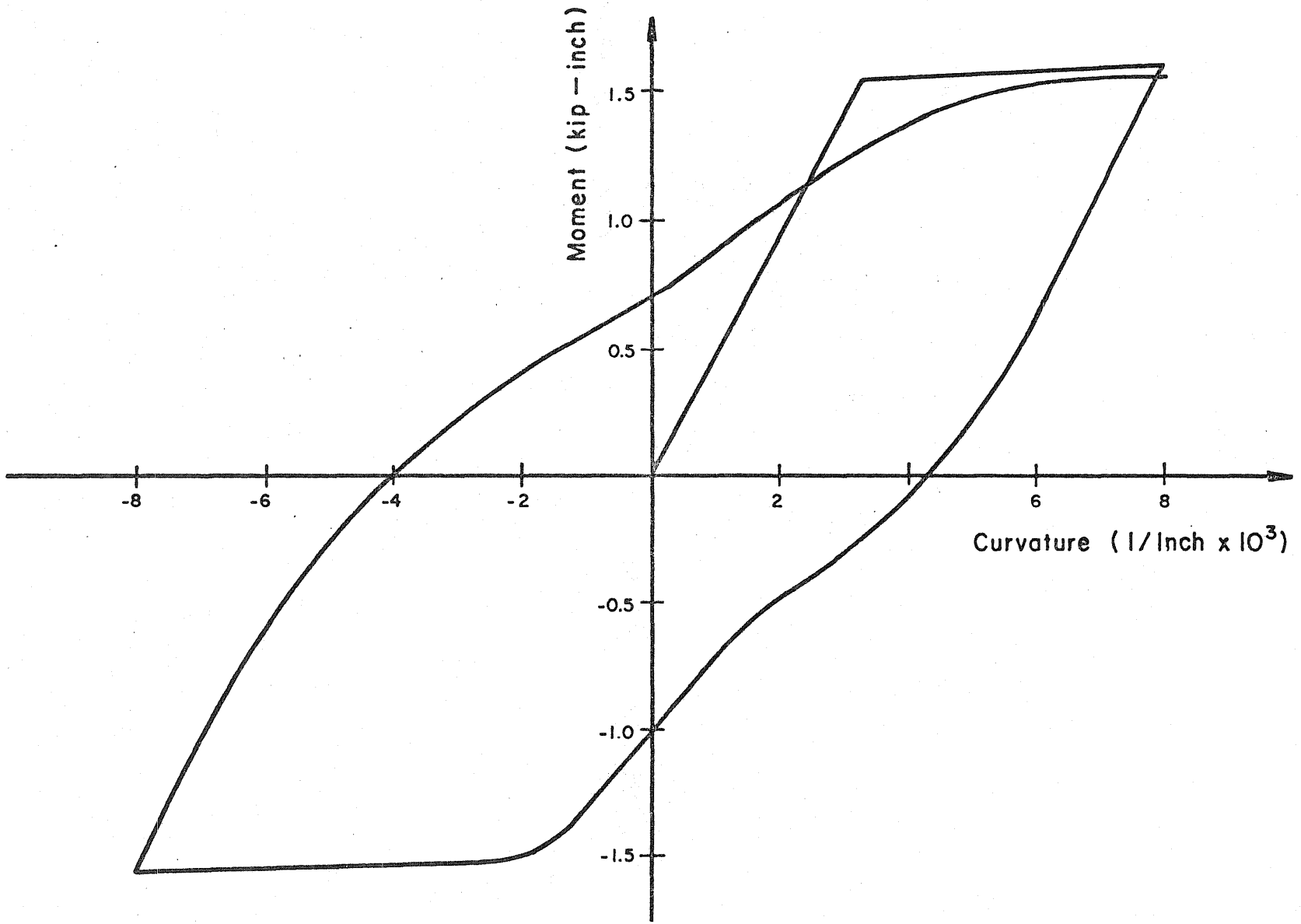

Fig. 4.6 Calculated Moment-Curvature Relationship for Cyclic Loading of Type SD Specimens

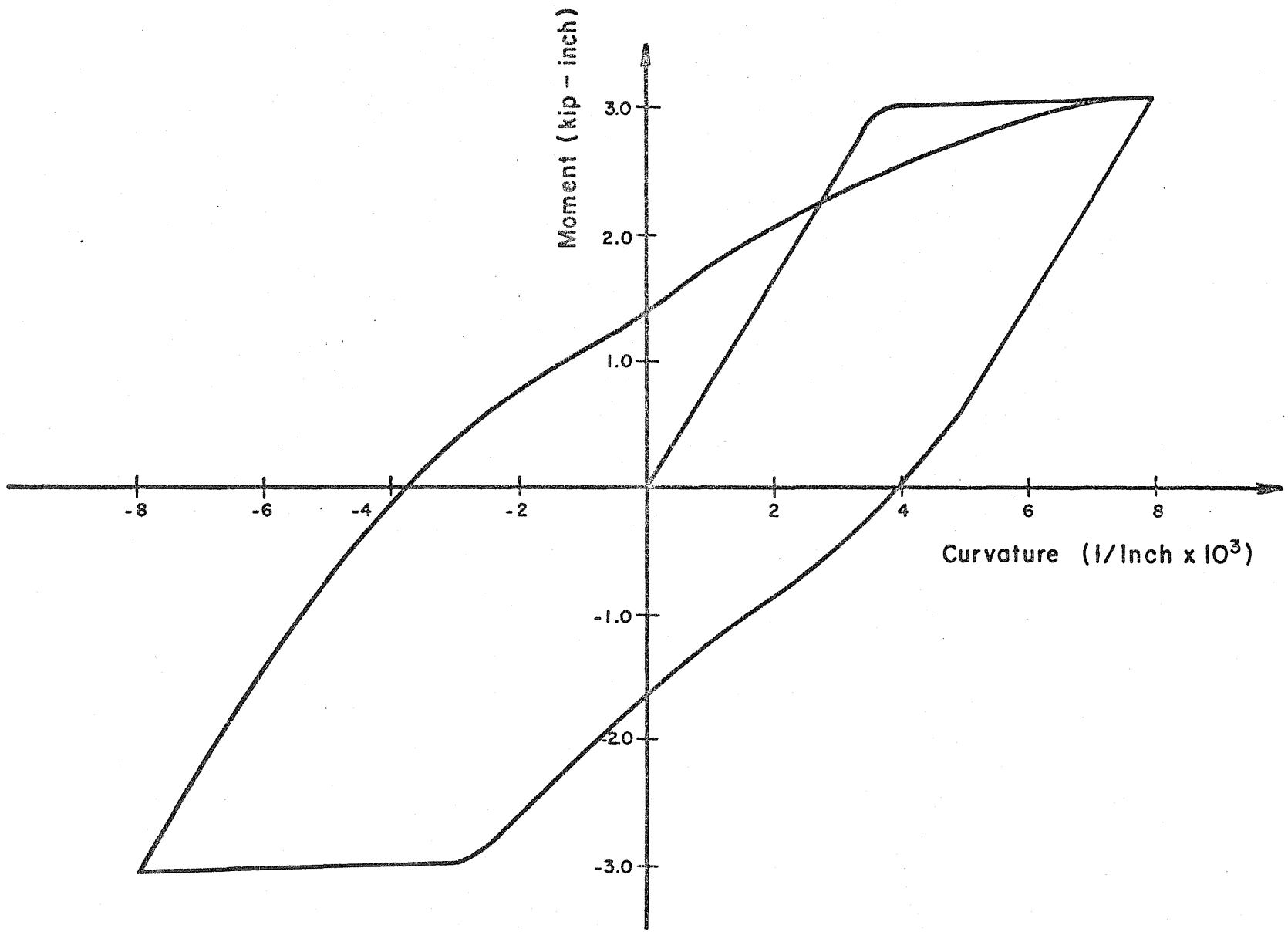

Fig. 4.7 Calculated Moment-Curvature Relationship for Cyclic Loading of Type SM Specimens

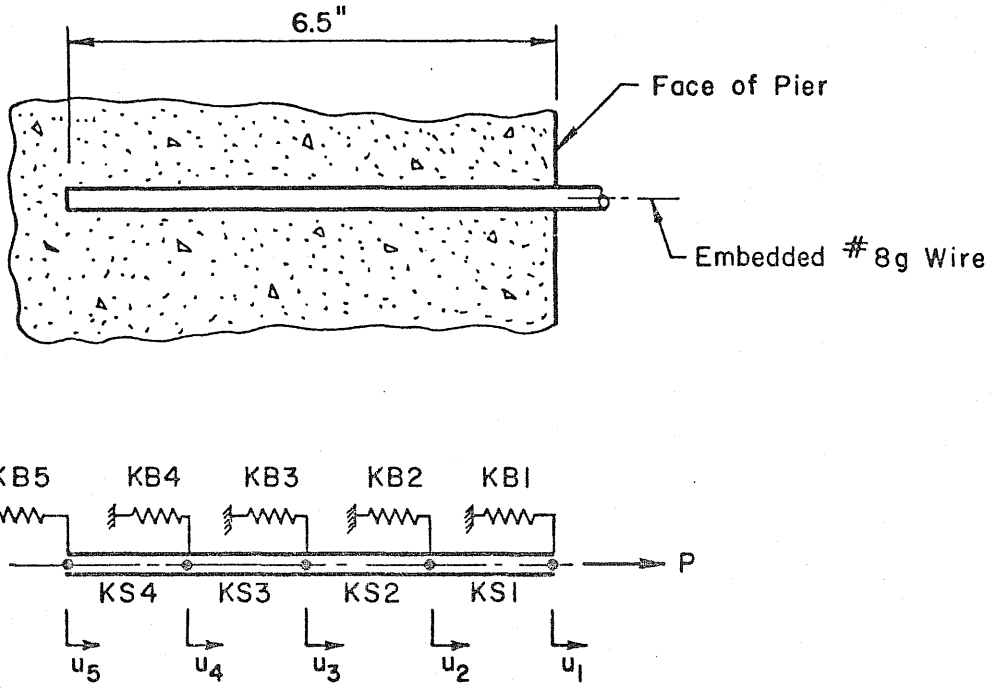

Fig. 4.8 Analytical Bar Embedment Model

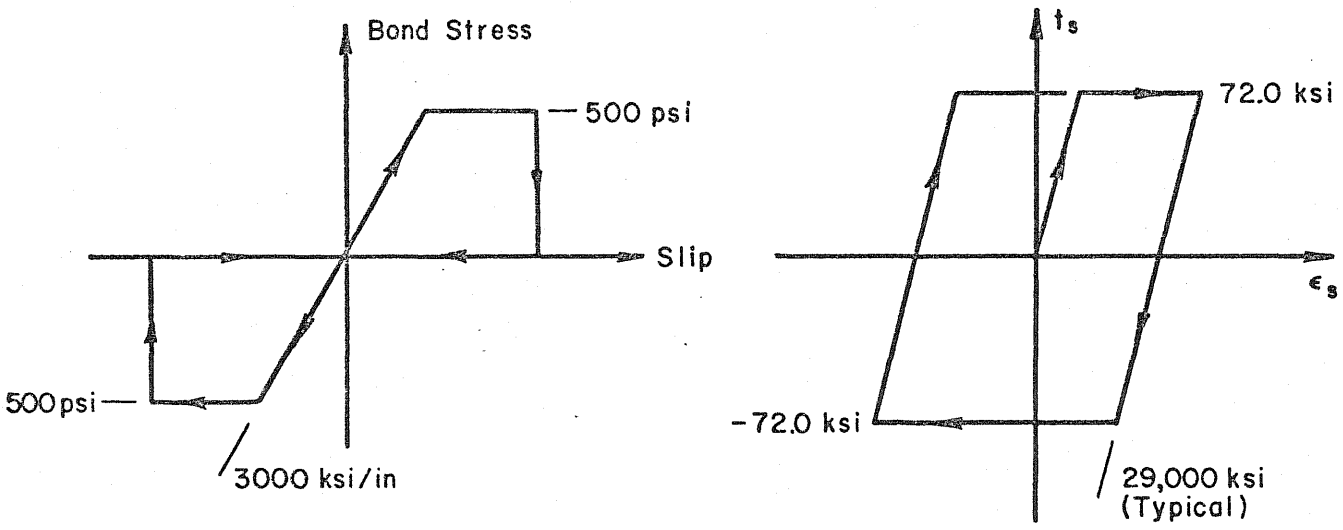

Fig. 4.9 Assumed Bond-Stress Slip and Reinforcing Stress-Strain Relationships

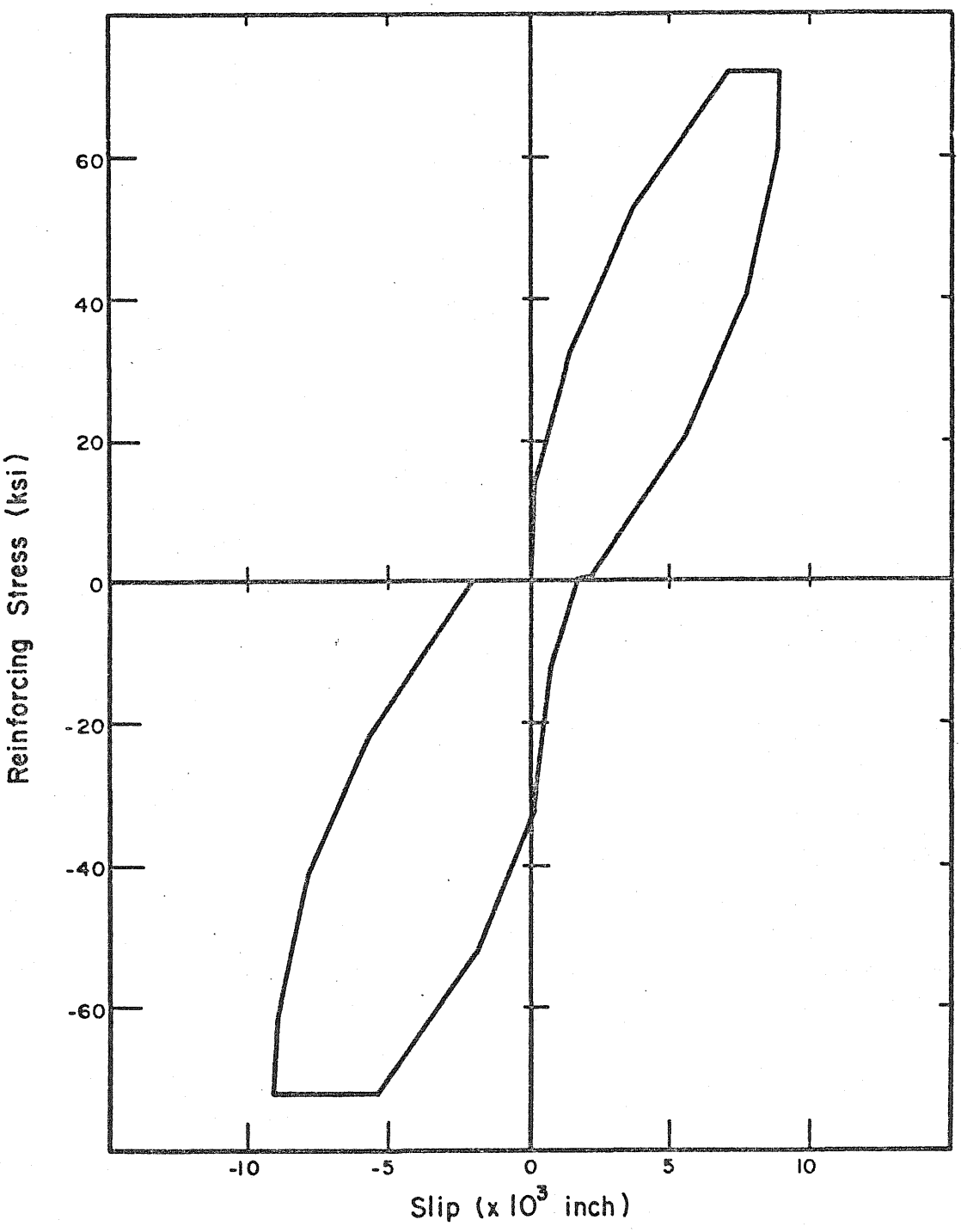

Fig. 4.10 Calculated Reinforcing Stress-Slip Relationship

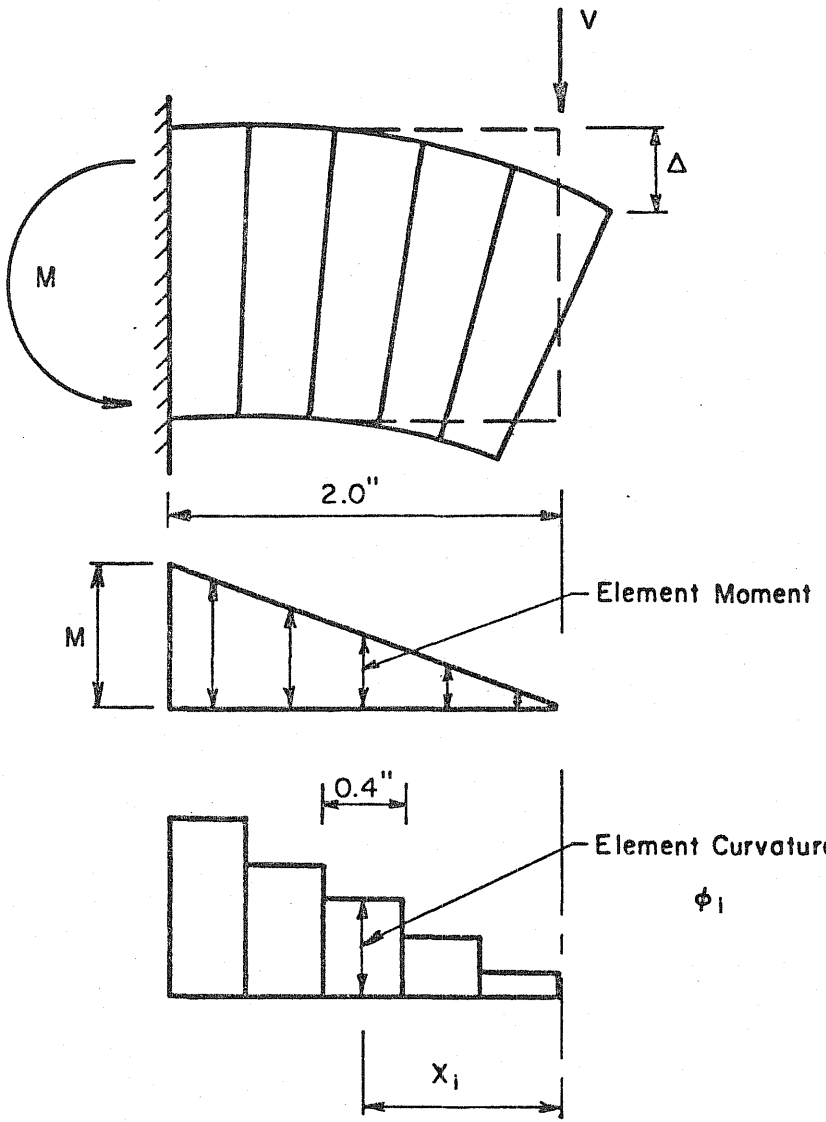

$$\Delta = \sum_{i=1}^{5} 0.4\ \phi_i\ X_i$$

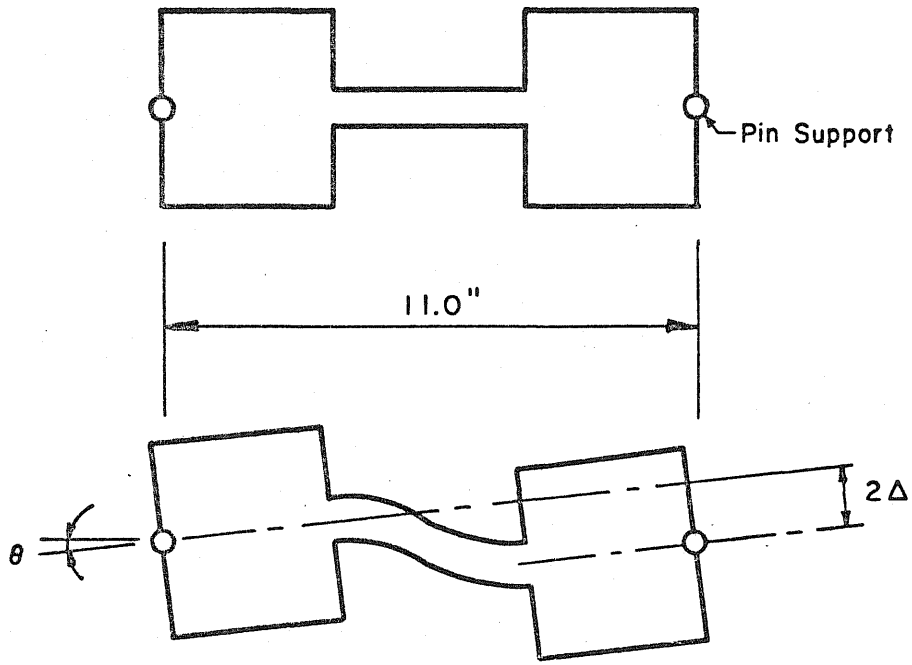

$$\theta = \frac{2\Delta}{11.0"}$$

Fig. 4.11 Calculation of Rotation from Curvatures

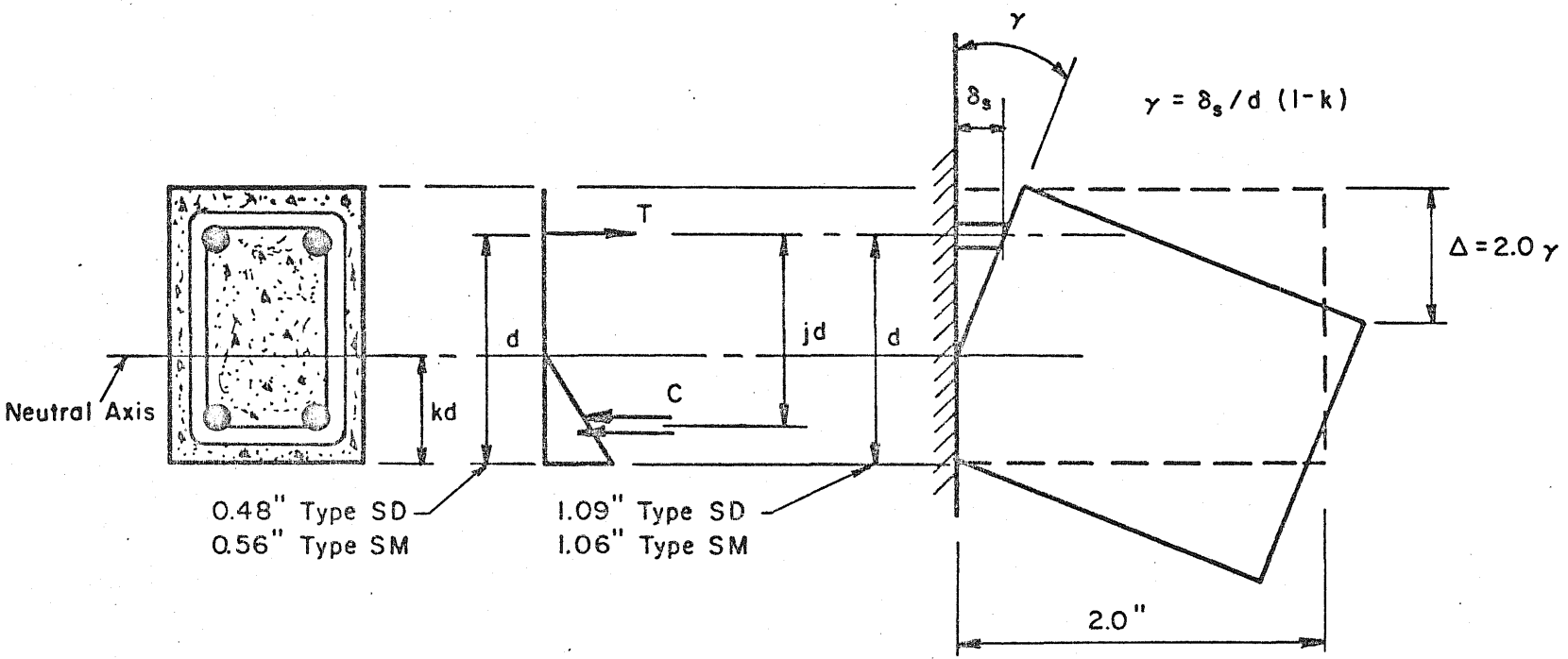

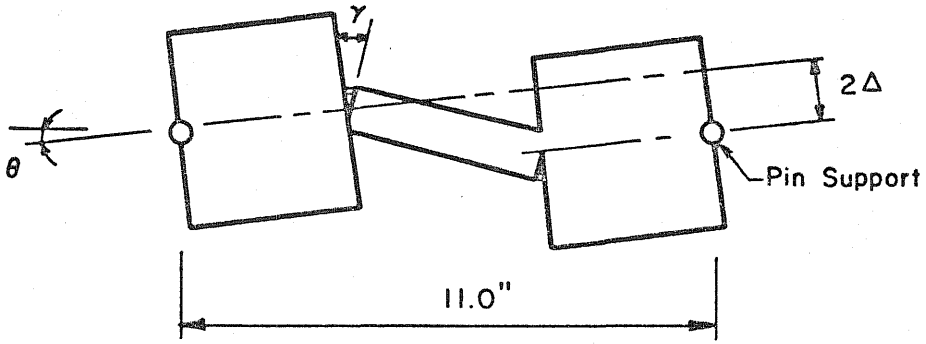

$$\theta = \frac{2\Delta}{11.0"} = \frac{4.0}{11.0"}\,\gamma$$

Fig. 4.12 Calculation of Rotation from Reinforcement Slip

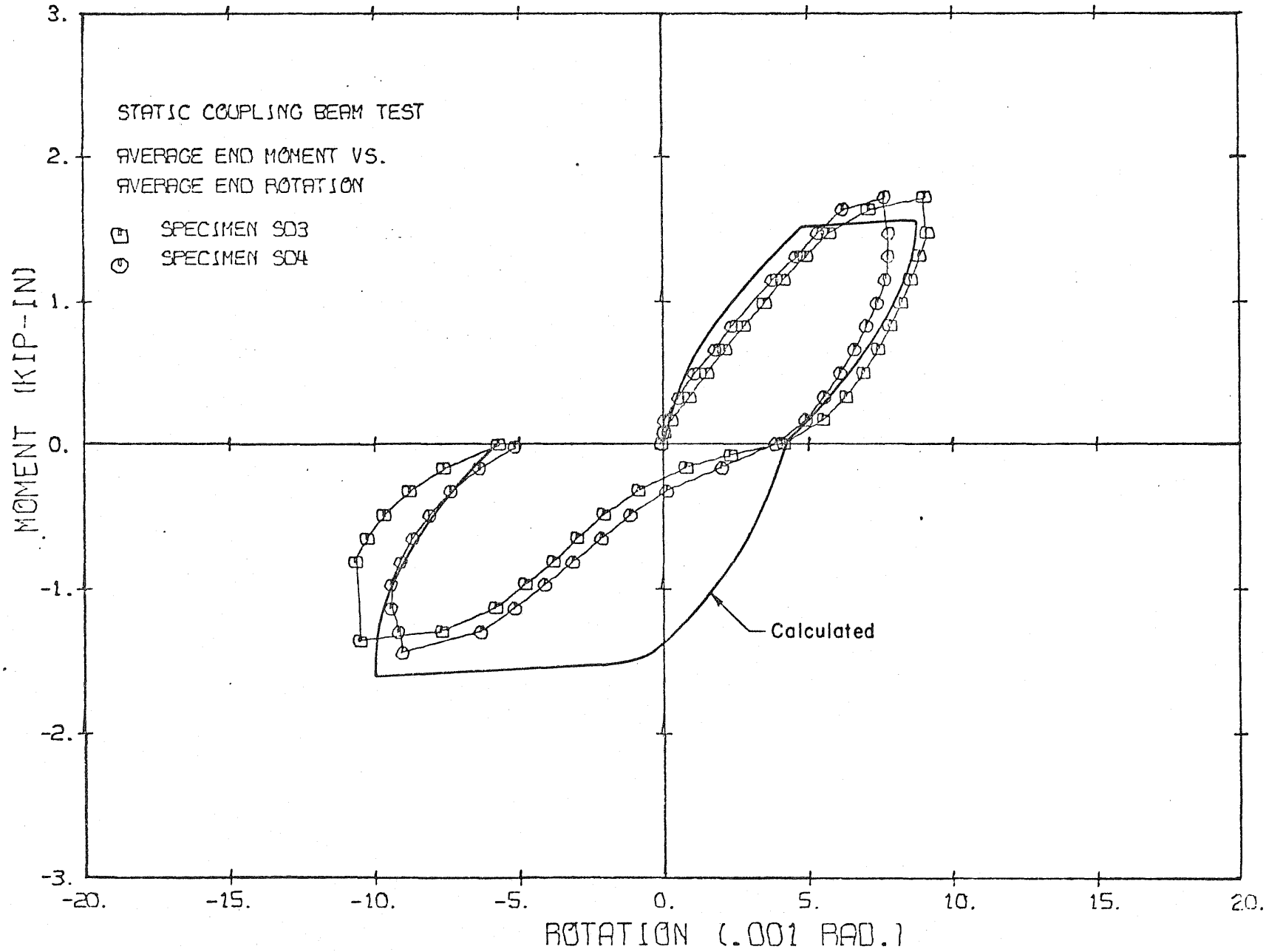

Fig. 5.1 Calculated Moment-Rotation Relationship for Type SD Specimens

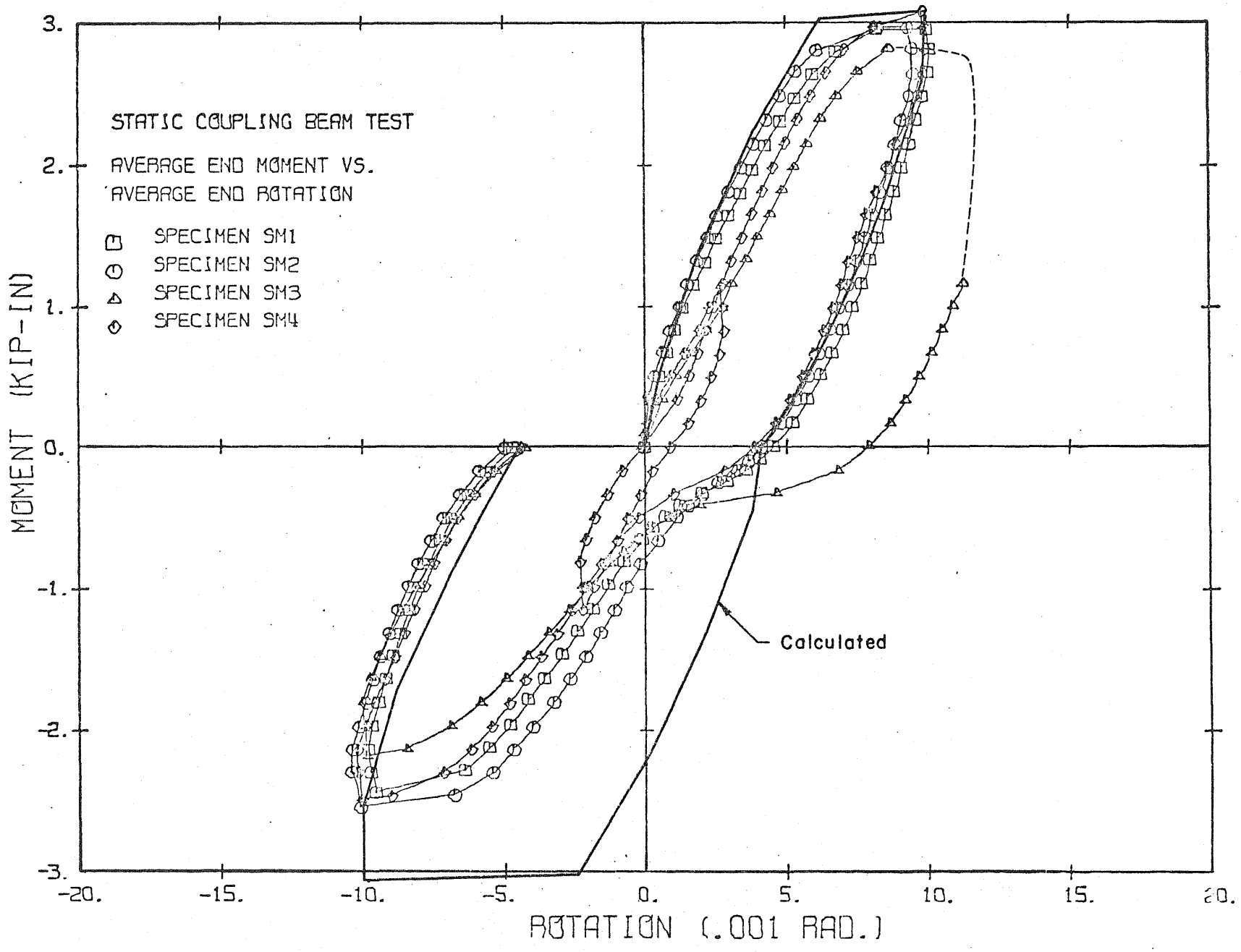

Fig. 5.2 Calculated Moment-Rotation Relationship for Type SM Specimens

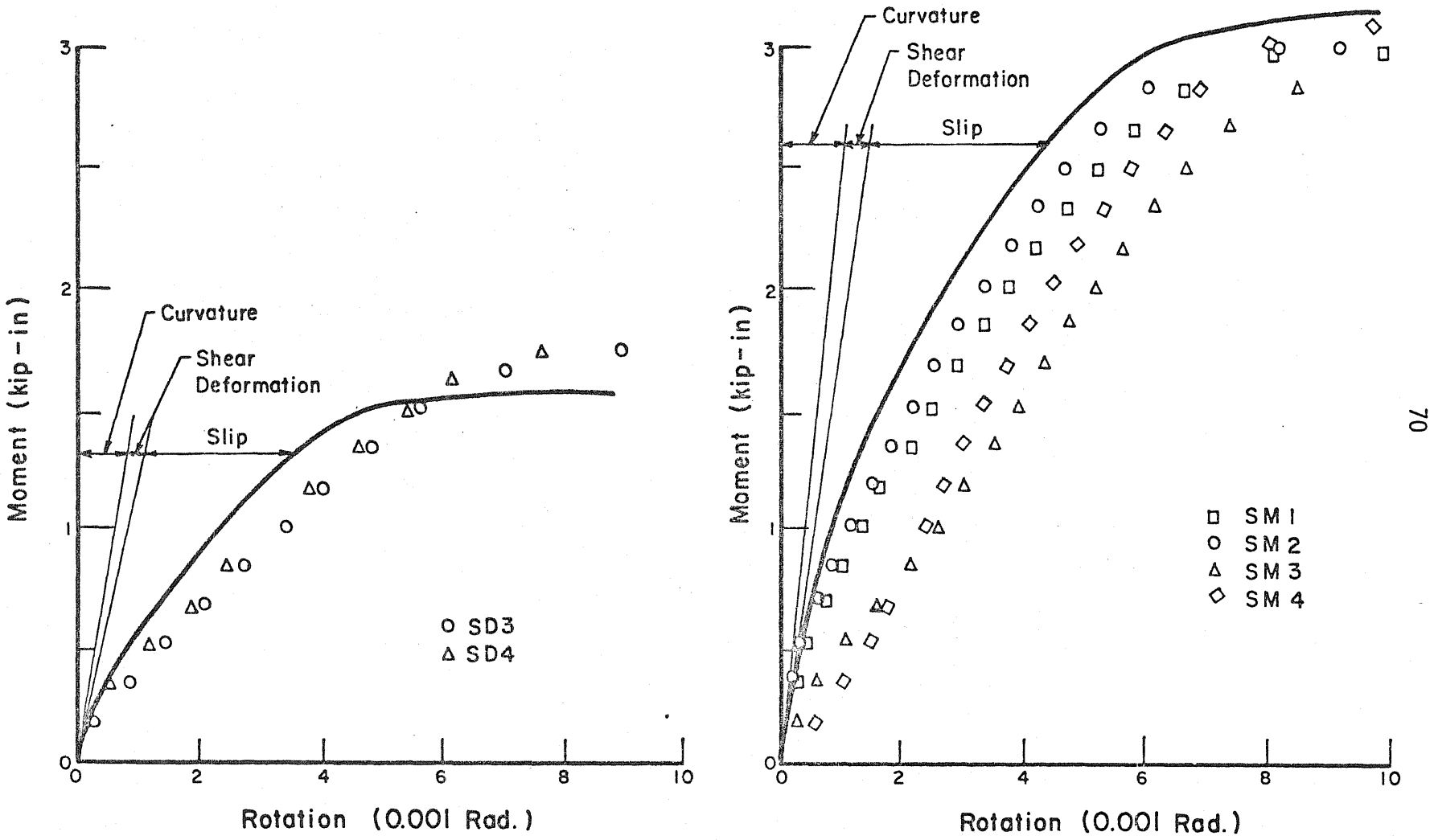

Fig. 5.3 Calculated Response for the First Quarter Cycle

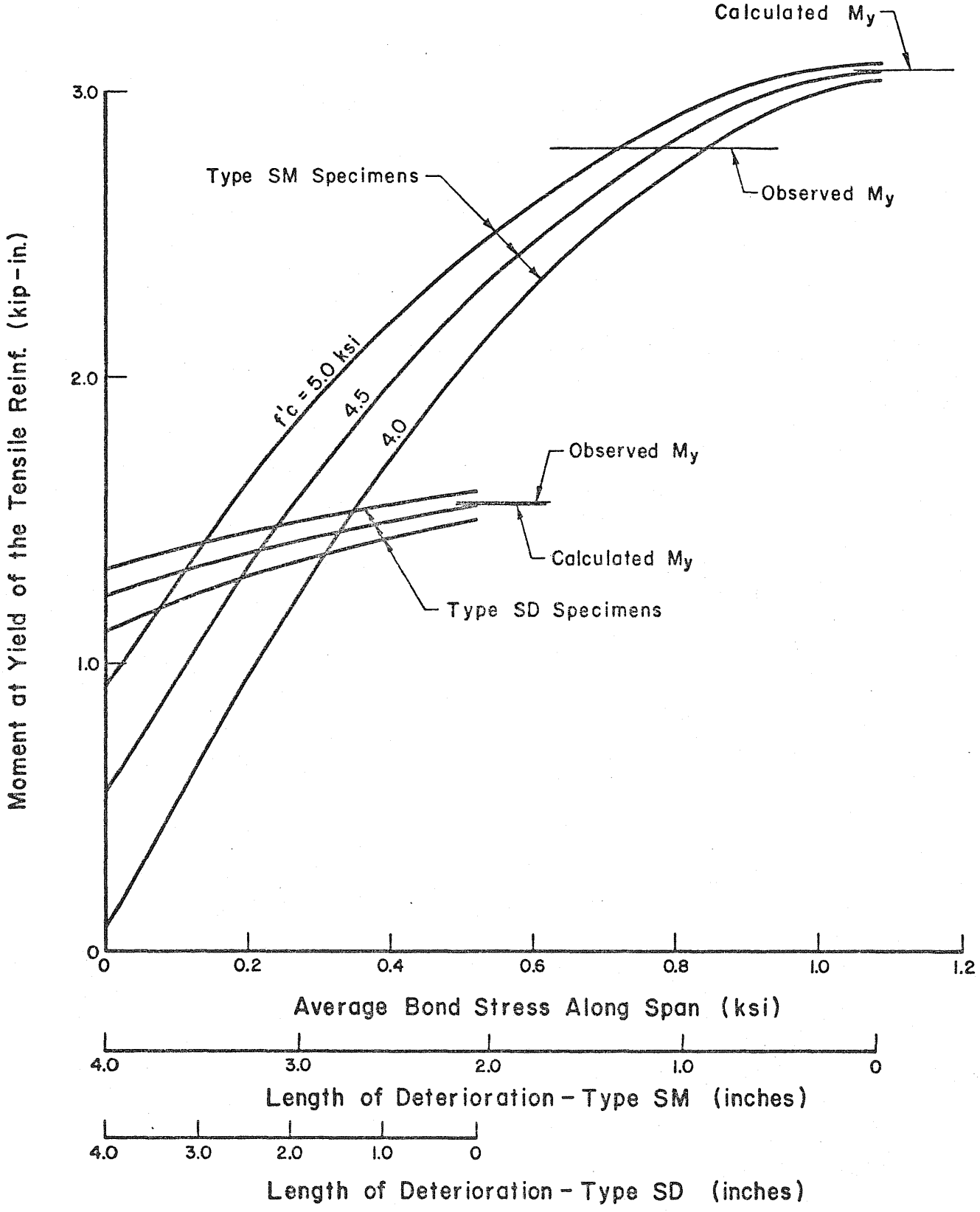

Fig. 5.4 Relationship Between the Internal Moment and Average Bond Stress Along Span

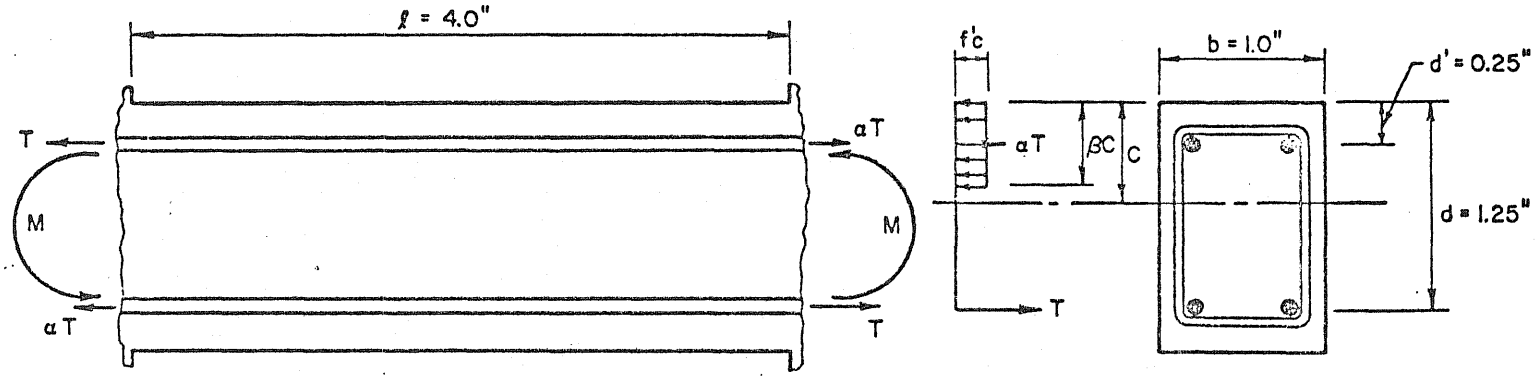

Average Bond Stress Along Span

$$\mu = \frac{T - \alpha T}{\pi d_b l n_b}$$

where d_b = Bar Diameter

n_b = Number of Bars per Face

$$\alpha = 1 - \frac{\mu \pi d_b l n_b}{T} \qquad (1)$$

From Equilibrium of Horizontal Forces at End Section

$$T + \alpha T = \beta c f'_c b \qquad (2)$$

Substituting (1)

$$2T - \mu \pi d_b l n_b = \beta c f'_c b$$

Solving for c

$$c = (2T - \mu \pi d_b l n_b)/\beta f'_c b \qquad (3)$$

From Equilibrium of Moments at End Section

$$M = Td + \alpha T d' - \beta c f'_c b \frac{\beta c}{2} \qquad (4)$$

Substituting (1) and (3) and Considering Yield in Tensile Reinforcement ($T = n_b A_{sb} f_y$)

$$M = n_b A_s f_y (d + d') - \mu \pi d_b l n_b d' - \left(\frac{2 n_b A_s f_y - \mu \pi d_b l n_b}{2 b f'_c}\right)^2$$

Fig. 5.5 Stress Distribution Across Section Considering Loss of Bond Within Span

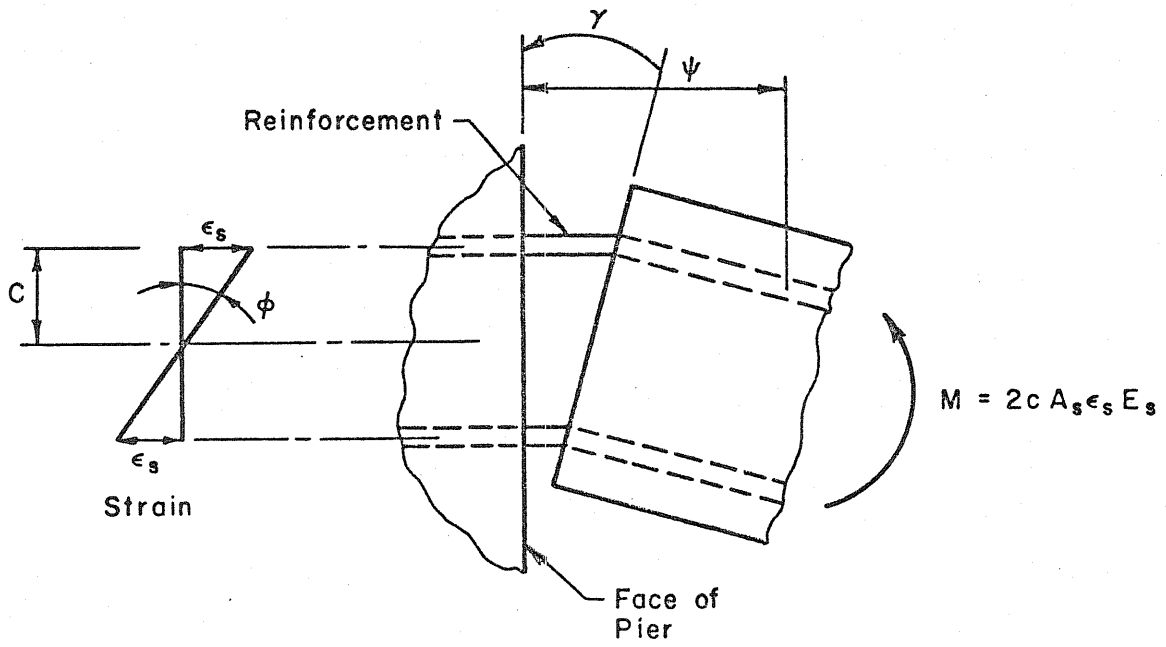

$$\phi = \frac{\epsilon_s}{c}$$

$\gamma = \phi\psi$ where ψ = strained length of reinforcement (2-in. assumed)

θ = measured rotation

$$\theta = \left(\frac{4}{11}\right)\gamma$$

$$\frac{M}{\theta} = \frac{2cA_s\epsilon_s E_s}{\left(\frac{4}{11}\right)\left(\frac{\epsilon_s}{c}\right)\psi} = \frac{22}{4}\,\frac{A_s E_s}{\psi}\,c^2 = \frac{22}{4}\,\frac{(.041)(29000)(0.5)^2}{(2.0)} = 817\frac{\text{kip-in.}}{\text{radian}}$$

Fig. 5.6 Stiffness of Member Consisting of Reinforcement Only

Appendix A

RELATIONSHIP BETWEEN MEASURED DISPLACEMENTS AND ROTATIONS

Beam end rotations were calculated from displacement readings obtained independently for each pier. Because of the small rotations that were measured, the effect of bolt slips at the pin connections were significant. Two horizontal and one vertical LVDT per aluminum rotation indicating bar were used to eliminate the effect of these slips from the beam end rotations. The LVDT locations with respect to each pin connection as described in Fig. A.1 are presented in Table A.1.

The actual angle of the measuring rod was obtained from the two horizontal displacement readings divided by the distance between the LVDT's as depicted in Fig. A.1. Since the largest rotation measured was approximately 0.02 radians, small angles were assumed in the calculations, i.e. $\sin\theta = \tan\theta = \theta$. Thus, the horizontal distance between each rotation measuring bar and pin connection was not relevant on the measured rotations.

Horizontal-bolt slip was calculated by interploting between the two horizontal displacement readings at the level of the pin connection. Vertical bolt slip was calculated using the difference between the vertical displacement reading, and the product of (1) the distance of the vertical LVDT from the pin connection and (2) the measured rotation of the aluminum bar. Both of these operations are shown in Fig. A.2.

Adjustments to the measured bar rotations were made from these slips. Differential horizontal slip between the left and right pin connections due to longitudinal expansion of the coupling beam caused a

residual rotation to be measured for each pier. The calculation of this rotation correction is presented in Fig. A.3. For this calculation, no differential slip of the pin connections of the top load application channel was considered. Also, the rotation correction was applied equally to each pier. The effect of unequal vertical bolt slip on the measured rotations was calculated by taking the difference of the slip of the left and right pin connections and dividing by the horizontal distance between the pins, as depicted in Fig. A.4.

Adjusted rotations for both the left and right ends of each coupling beam for each cycle of loading are given in Fig. 3.1 through 3.6. As can be seen, reasonable agreement between each end rotation was obtained with the largest difference between each end rotation being approximately 0.001 radian. The difference may be due to unequal flexural resistance of each end of the coupling beam associated with slip in the pin connections of the top load application channel. Inaccuracies of approximately one percent may also have existed in the measuring instruments.

Table A.1

LVDT Locations*

(Inches)

Specimen	L1	L2	L3	L4	L5	L6
SD3	25.91	3.82	4.84	26.00	3.74	4.69
SD4	25.84	3.91	4.85	26.00	3.78	4.63
SM1	25.76	3.99	4.70	25.96	3.82	4.64
SM2	25.96	3.79	4.70	25.39	3.89	4.60
SM3	26.09	3.66	4.70	25.96	3.82	4.60
SM4	25.88	3.87	4.70	25.99	3.79	4.60

*Refer to Fig. A.1

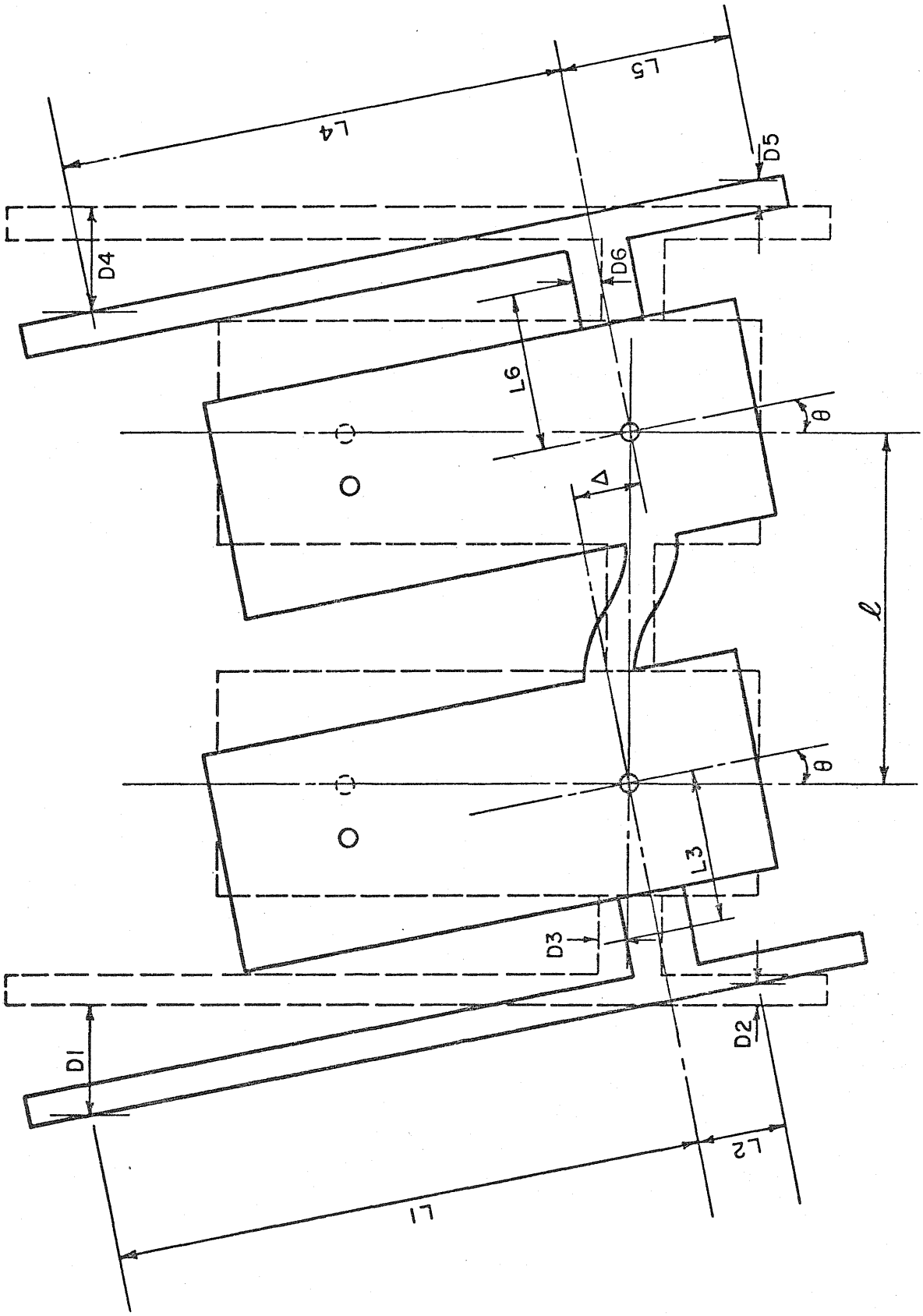

Fig. A.1 LVDT Locations

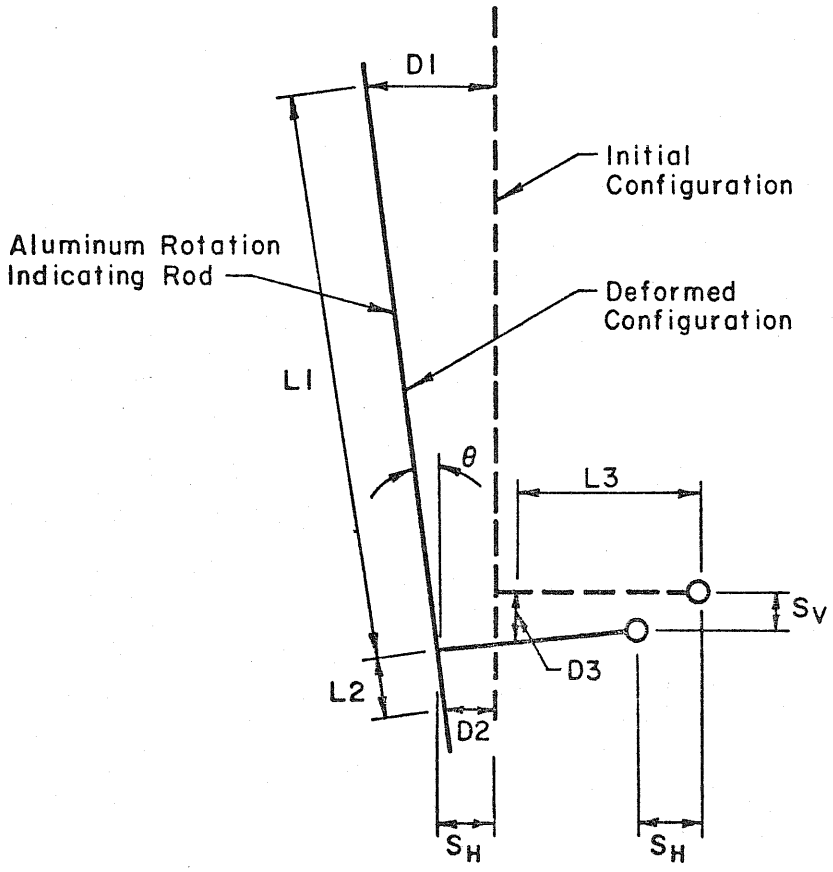

$$\theta = \frac{D1-D2}{L1+L2}$$

S_V = Vertical Bolt Slip
$= D3-(L3)(\theta)$

S_H = Horizontal Bolt Slip
$D1-(L1)(\theta)$

Fig. A.2 Calculation of Bolt Slip

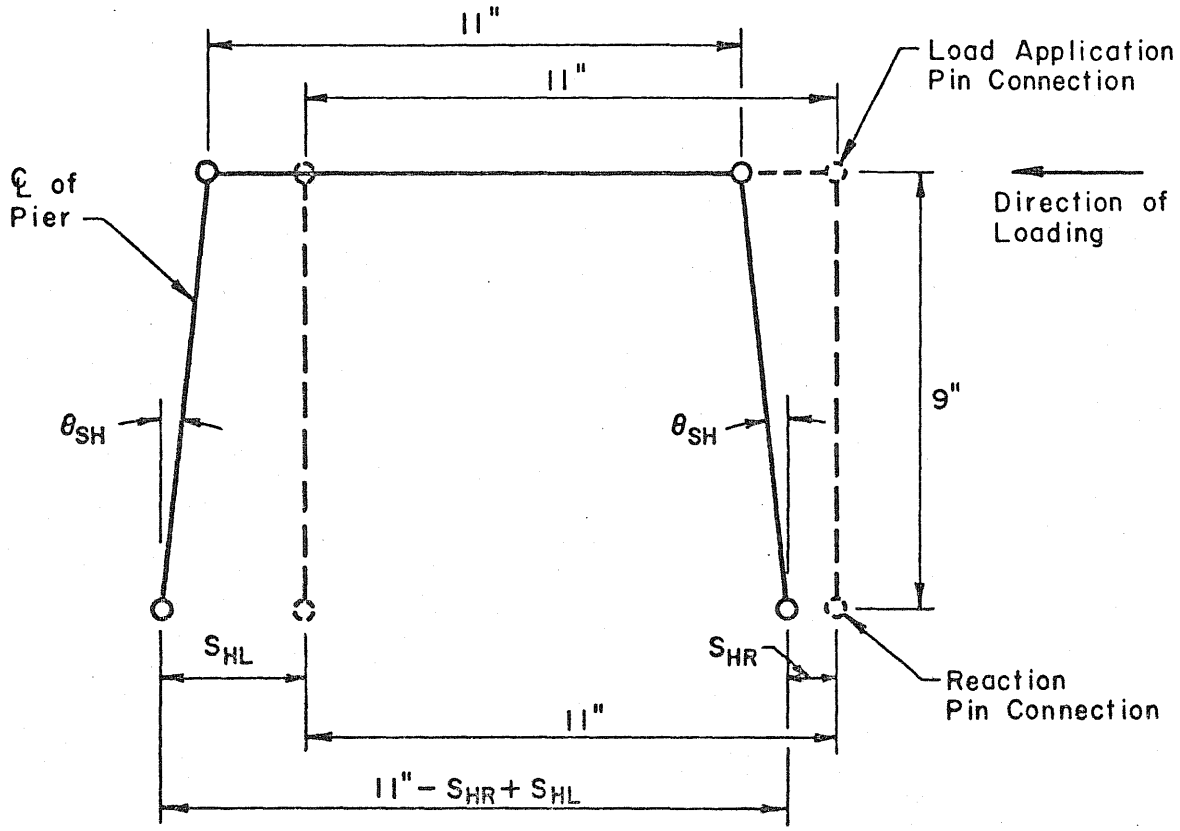

S_{HL} , S_{HR} = Left and Right Horizontal Bolt Slip

θ_{SH} = Rotation Correction Due To Horizontal Bolt Slip

$$= \frac{1}{2} (S_{HL} - S_{HR}) / 9"$$

Fig. A.3 Rotation Adjustment for Horizontal Bolt Slip

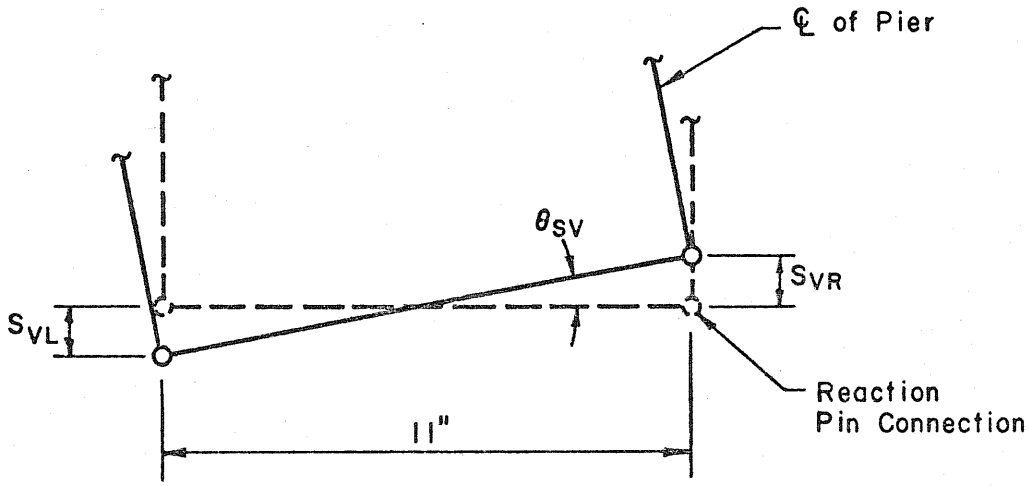

S_{VL} , S_{VR} = Left and Right Vertical Bolt Slip

θ_{SV} = Rotation Correction Due To Vertical Bolt Slip

$= (S_{VL} + S_{VR}) / 11"$

Fig. A.4 Rotation Adjustment for Vertical Bolt Slip